Multiscale Modeling and Computation of 3D Incompressible Turbulent Flows

Thesis by

Xin Hu

In Partial Fulfillment of the Requirements

for the Degree of

Doctor of Philosophy

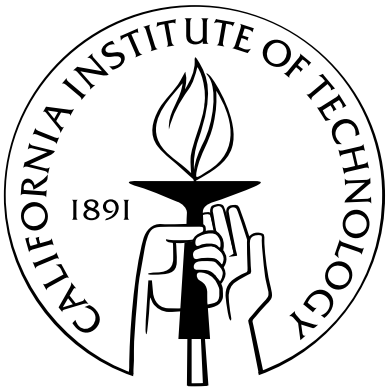

California Institute of Technology

Pasadena, California

2012

(Defended May 4, 2012)

To my wife Lan, daughter Ellie and parents Jiagao Hu and Shiju Zheng

Acknowledgements

First of all, my gratitude goes to my research adviser, Prof. Thomas Y. Hou, who has been supporting and encouraging me throughout my Ph.D. adventure at Caltech. I have greatly benefited from his enthusiasm, rigor, broad but deep insight on math. Thanks to him for bringing me into the area of multiscale analysis modeling of turbulence, which leads to this thesis.

I want to express my deep gratitude to my adviser of M.S. degree at Peking University, Prof. Shaoqiang Tang, for his mentorship, friendship and bringing me into the fantastic but challenging field of applied math. Besides, I would like to heartily thank Dr. Guang Lin at Pacific Northwest National Laboratory for his hospitality when I spent the summer in 2011 doing an internship with him. The discussion and collaboration with him expanded my vision and knowledge. Unfortunately, the work done at PNNL is not included in this thesis, but I have learned a lot about stochastic PDE from him. I also thank Prof. Fazle Hussain for his comments and suggestions on turbulence part of my thesis.

I want to thank Professors Guillaume Blanquart, Thomas Y. Hou, Daniel I. Meiron and Houman Owhadi for kindly serving on my dissertation committee and their valuable suggestions.

It has been a pleasure to interact with people at Caltech. My deep gratitude goes to Michio Inoue for his inspiring and educational discussions on turbulence and numerical schemes, Alex Gittens for his kind help on my English and interesting discussions on American and Asian cultures, Pengchong Yan for his help on DDSM method and his books and experience on raising a baby, and Guo Luo for his discussion on Poisson solver. I thank everyone in the Caltech Chinese community. They make my life at Caltech much easier and I have had a lot of fun with them. I also thank my friends

and badminton mates, Xiaolan Zhang, Wuxing Li, Rong Xiao, Yousong Ding, Han Yi, Xiquan Cui, Chunlan Lu, Chun Huang, Xuexian Li and Yun Zhou, for keeping me fit and having so many parties and happy times together. Sincere thanks go to Sydney Garstang, Carmen Nemer-Sirois, Sheila Shull, Icy Ma and William Yardley. They are always there whenever I need help. Special and unique thanks to Ms. Maribelle Denslow, who has given me so much convenience when I stayed at her place. She is my life teacher and makes me feel at home even tens of thousands miles away from my home country.

Last but not least, I want to express my greatest gratitude to my parents, Jiagao Hu and Shiju Zheng, and my wife, Lan Cui. It would not be possible for me to come to this point without their unconditional support and love. My parents know nothing about my research, but they educated me to be a good person with dignity, which I think goes beyond science. My wife has been standing by me for so many years with her warm heart and ready-to-help hands, through up and down. I also want to thank my little angel, Ellie. You have brought me so many joys and keep giving me surprises.

Abstract

Computing turbulent flows is a challenge due to the large range of scales involved. Developing an effective turbulence model is important not only for engineering applications but also for fundamental understanding of the flow physics. In this thesis, we present a systematic way to derive the LES model based on multiscale analysis. In addition, turbulent flows are treated as stochastic processes and a data-driven stochastic method is applied to compute the turbulent flows.

In the first part, we present a mathematical derivation of a closure relating the Reynolds stress to the mean strain rate for incompressible turbulent flows. This derivation is based on a systematic multiscale analysis that expresses the Reynolds stress in terms of the solutions of local periodic cell problems. We reveal an asymptotic structure of the Reynolds stress by invoking the frame invariant property of the cell problems and an iterative dynamic homogenization of large- and small-scale solutions. The Smagorinsky model for homogeneous turbulence is recovered as an example to illustrate our mathematical derivation. Another example is turbulent channel flow, where we derive a simplified turbulence model based on the asymptotic flow structure near the wall. Additionally, we obtain a nonlinear model by using a second order approximation of the inverse flow map function. This nonlinear model captures the effects of the backscatter of kinetic energy and dispersion and is consistent with other models, such as a mixed model that combines the Smagorinsky and gradient models, and the generic nonlinear model of Lund and Novikov.

Numerical simulation results at two Reynolds numbers using our simplified turbulence model are in good agreement with both experiments and direct numerical simulations in turbulent channel flow. However, due to experimental and modeling errors, we do observe some noticeable differences, e.g. , root mean square velocity

fluctuations at $Re_\tau = 180$.

In the second part, we present a new perspective on calculating fully developed turbulent flows using a data-driven stochastic method. General polynomial chaos (gPC) bases are obtained based on the mean velocity profile of turbulent channel flow in the offline part. The velocity fields are projected onto the subspace spanned by these gPC bases and a coupled system of equations is solved to compute the velocity components in the Karhunen-Loève expansion in the online part. Our numerical results have shown that the data-driven stochastic method for fully developed turbulence offers decent approximations of statistical quantities with a coarse grid and a relatively small number of gPC base elements.

Contents

List of Figures

List of Tables

Chapter 1

Introduction

1.1 Direct numerical simulation of fluid dynamics

Turbulence has been a central research area in fluid dynamics since the 19th century. The Navier-Stokes equations, one of seven millennium prize problems established by the Clay Mathematics Institute[1], accurately describes turbulent flows, according to extensive theoretical and experimental works. However, it is an open question whether the solution of the 3D incompressible Navier-Stokes equations with smooth initial data with finite energy remains smooth for all time. In addition, it is extremely difficult to solve the following Navier-Stokes equations for incompressible flows due to their non-local non-linear nature:

$$\frac{\partial \boldsymbol{u}}{\partial t} + (\boldsymbol{u} \cdot \nabla)\boldsymbol{u} + \nabla p = \nu \Delta \boldsymbol{u}, \tag{1.1.1}$$
$$\nabla \cdot \boldsymbol{u} = 0,$$

with proper initial and boundary conditions.

Nowadays, thanks to the progress of computer technology, it is possible to perform direct numerical simulations (DNS) of the Navier-Stokes equations. But still it requires tremendous computing resources to perform DNS of turbulent flows, especially at a high Reynolds number (Re) and/or with irregular geometry. In the homogeneous turbulent flows, the ratio between the characteristic length of the most energetic scale

[1] http://www.claymath.org/millennium/

L and that of the smallest dynamically active scale η is given by

$$\frac{L}{\eta} = \mathcal{O}\left(Re^{3/4}\right),$$

where Re is the Reynolds number, which measures the ratio of inertial forces and molecular viscosity. Thus, in a cubic volume with edge L, approximately $\mathcal{O}(Re^{9/4})$ degrees of freedom are needed to represent all the scales. In addition, the characteristic time also scales as $\mathcal{O}(Re^{3/4})$. Therefore, a total of $\mathcal{O}(Re^3)$ degrees of freedom in time-space are needed. Another example is the wall-bounded flow at a very high Re with no-slip boundary conditions. Many grid points have to be allocated in the near-wall region in order to resolve the small turbulent structures. Chapman (1979) estimated that the number of grid points needed to resolve the inner boundary layer is proportional to $Re^{1.8}$. To give a flavor of the computational cost of a DNS, the followings are some representative examples (Berselli *et al.*, 2006):

(i) model airplane: $Re \approx 7 \times 10^4$ with characteristic length $1\,m$ and velocity $1\,m/s$,
$N \approx 8 \times 10^{10}$ grid points per time step for a DNS;

(ii) cars: $Re \approx 6 \times 10^5$ with characteristic velocity $30\,m/s$,
$N \approx 10^{13}$ grid points per time step for a DNS;

(iii) airplanes: $Re \approx 2 \times 10^7$ with characteristic velocity $300\,m/s$,
$N \approx 2 \times 10^{16}$ grid points per time step for a DNS;

(iv) atmospheric flows: $Re \approx 10^{20}$,
$N \approx 10^{45}$ grid points per time step for a DNS.

Moreover, even if DNS were computationally feasible for turbulent flows, defining precise initial and boundary conditions remains challenging. At high Reynolds numbers, even small boundary perturbations may excite the already existing small scales, introducing noises into the system. As observed in Aldama (1990), the uncontrollable nature of the boundary conditions produces random responses. Therefore, it makes more sense to ask for the statistics of turbulent flows.

1.2 Classical turbulence modeling

Since DNS is computationally expensive, efforts have been taken to reduce the cost of numerical simulations via turbulence modeling. Typically, large-scale solutions are calculated using a coarse grid, while the small-scale effects are modeled and integrated into the equations of large-scale variables.

1.2.1 A brief overview of turbulence modeling

In order to be able to compute the solution of turbulent flows, we reduce the number of degrees of freedom by introducing a coarse level description of the flows. There are mainly two ways to reduce the number of degrees of freedom in numerical simulation:

(i) Calculating the statistical ensemble-average of the solution. The resulting equations are called the Reynolds Averaged Navier-Stokes equations (RANS) (Launder & Spalding, 1972). The idea is Reynolds decomposition. The exact solution $\boldsymbol{u}$ is split into two parts: the statistical average $\langle \boldsymbol{u} \rangle$ and a fluctuation $\boldsymbol{u}'$ (illustrated in Figure 1.1):

$$\boldsymbol{u}(\boldsymbol{x}, t) = \langle \boldsymbol{u}(\boldsymbol{x}, t) \rangle + \boldsymbol{u}'(\boldsymbol{x}, t).$$

Only for statistically steady turbulence, the average is in practice obtained by a time average

$$\langle \boldsymbol{u}(\boldsymbol{x}, t) \rangle \approx \bar{\boldsymbol{u}}(\boldsymbol{x}) = \lim_{T \to \infty} \frac{1}{T} \int_0^T \boldsymbol{u}(\boldsymbol{x}, t) \mathrm{d}t.$$

The above time-average operations result in a much smaller number of degrees of freedom. The most popular RANS models appear to yield satisfactory predictions in attached flows and some with shallow separations. However, RANS predictions of massive separations have typically been unreliable (Travin *et al.*, 2001; Squires *et al.*, 2005).

(ii) Calculating only the low-frequency modes, while high-frequency fluctuations are modeled (illustrated in Figure 1.2). This is done in Large Eddy Simulation (LES). The solutions are separated into two parts: a large-scale component and

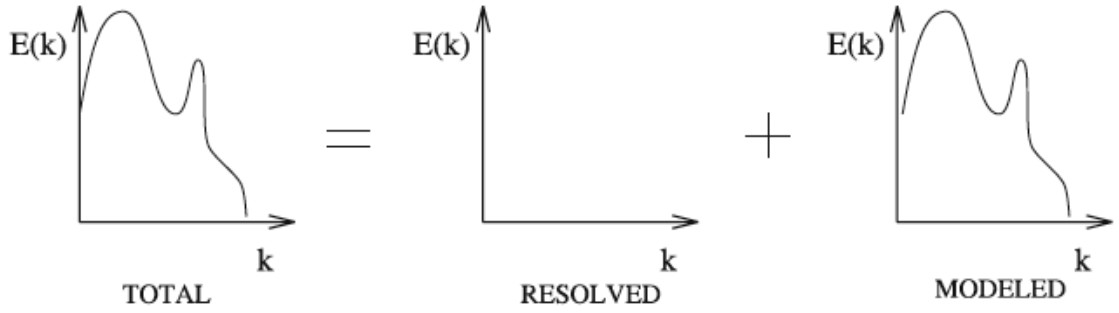

Figure 1.1: Symbolic representation of energy spectrum splitting of RANS, taken from Sagaut (2001)

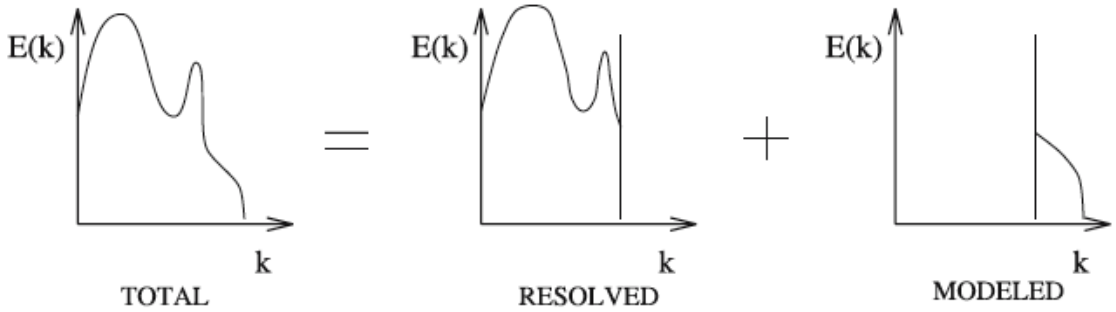

Figure 1.2: Symbolic representation of energy spectrum splitting of LES, taken from Sagaut (2001)

small-scale fluctuations:

$$\boldsymbol{u}(x,t) = \boldsymbol{U}(\boldsymbol{x},t) + \boldsymbol{u}'(\boldsymbol{x},t). \tag{1.2.1}$$

A reference or cutoff length scale is used to define the above scale separation. Great effort has been taken in this thesis to derive mathematically the modeled effect–the Reynolds stress in the resultant LES equations–with minimal assumptions based on the multiscale analysis.

In the first part of this thesis, we focus on LES. After substituting the decomposition (1.2.1) into the Navier-Stokes equations (1.1.1) and taking the mean, the Reynolds equation is obtained:

$$\begin{aligned} &\frac{\partial \boldsymbol{U}}{\partial t} + (\boldsymbol{U}\cdot\nabla)\boldsymbol{U} + \nabla\cdot\langle \boldsymbol{u}'\otimes\boldsymbol{u}'\rangle + \nabla\langle p\rangle = \nu\Delta\boldsymbol{U}, \\ &\nabla\cdot\boldsymbol{U} = 0, \end{aligned} \tag{1.2.2}$$

with proper initial and boundary conditions.

The velocity covariances $\langle \boldsymbol{u}' \otimes \boldsymbol{u}' \rangle$ are called the Reynolds stress. Many turbulence models have been developed to approximate the Reynolds stress, aimed at capturing the most important statistical quantities of turbulent flows: profiles of mean velocity, r.m.s. velocity fluctuations, etc. Among them, the turbulent-viscosity models were the first attempts. Based on the turbulent-viscosity hypothesis in these models, the Reynolds stress is given by

$$\langle \boldsymbol{u}' \otimes \boldsymbol{u}' \rangle = \frac{2}{3} k \mathcal{I} - \nu_T \left(\nabla \boldsymbol{U} + \nabla \boldsymbol{U}^T \right), \tag{1.2.3}$$

where ν_T is the turbulent viscosity. In applications to turbulent boundary-layer flows, the mixing length model was proposed (Prandtl, 1925)

$$\nu_T = l_m^2 \left| \frac{\partial \boldsymbol{U}}{\partial y} \right|. \tag{1.2.4}$$

But the turbulent structures are over-simplified and the essential physical mechanisms are not included. More complicated models, such as k-ϵ, k-ω models (Mohammadi & Pironneau, 1994; Sagaut, 2001; Berselli *et al.*, 2006), have been proposed and incorporated in most commercial CFD softwares.

Another popular model is the Smagorinsky model (Smagorinsky, 1963) and its variants (van Driest, 1956, for an example of channel flow), which have succeeded in many applications, e.g. , homogeneous turbulence and turbulent channel flow. In the Smagorinsky model, the turbulent viscosity is given as

$$\nu_T = (C_s \Delta)^2 \left\| \mathcal{D} \right\|_F, \tag{1.2.5}$$

where C_s is the Smagorinsky constant, Δ is the filter width and $\mathcal{D}$ is the mean strain rate:

$$\mathcal{D} = \frac{1}{2} \left(\nabla \boldsymbol{U} + \nabla \boldsymbol{U}^T \right). \tag{1.2.6}$$

Recently, a class of subgrid stress models for large eddy simulation (LES) have been obtained by Misra & Pullin (1997) based on the vortex-based Reynolds stress closure. An equation relating the subgrid stress to the vortex-structure orientation

and the subgrid kinetic energy and the Kolmogorov energy spectrum assumption for the subgrid vortices gives a coupling closure. This model has been tested in decaying turbulence. LES has been able to calculate practical engineering flows even in relatively complex geometries (Ferziger, 1977; Lesieur & Métais, 1996; Rogallo & Moin, 1984; Sagaut, 2001). However, it is still prohibitively expensive to simulate wall-bounded flows at high Re, since a huge number of grid points are needed to resolve the small structures near the wall (Chapman, 1979; Spalart *et al.*, 1997). Efforts have been made to address the issue of LES near the wall by fitting a log law or coupling the thin boundary layer equations and a damped mixing-length eddy viscosity (Cabot & Moin, 1999; Wang & Moin, 2002). Later, a special near-wall subgrid-scale model based on wall parallel filtering and wall-normal averaging of the streamwise momentum equation was developed (Chung & Pullin, 2009). This LES model was performed for turbulent channel flow at Re_τ in the range 2×10^3 to 2×10^7.

On the other hand, hybrid models, which combine LES with RANS equation, have been proposed to improve the modeling performance of wall-bounded turbulence (Baggett, 1998; Hamba, 2003). Most popular RANS models appear to yield good predictions of high Re turbulent flows. Hence, the RANS model is applied near the wall, while LES is carried out away from the wall. Spalart *et al.* (1997) proposed the detached eddy simulations (DES) by modifying the Spalart-Allmaras one-equation model. The RANS simulation in the near-wall region is switched to the LES in the outer region, where the model length scale is changed from the wall distance to a pseudo-Kolmogorov length scale. DES have been performed to predict separated flows around a rounded-corner square at 10 degree angle of attack (Squires *et al.*, 2005). Nevertheless, all these models have closure problems, which means that these models are based on empirical formulations and/or fitting to experimental data. No systematic mathematical derivation of such a turbulence model has been achieved yet.

1.2.2 Summary of the results of turbulence modeling via multiscale analysis

In Chapter 2, we present a mathematical derivation based on a multiscale analysis of Navier-Stokes equations developed by Hou *et al.* (2005, 2008), aiming to provide an explicitly systematic derivation of the Reynolds stress term in the LES models. This multiscale analysis is developed for 3D homogeneous incompressible Euler and Navier-Stokes equations using a semi-Lagrangian point of view. A multiscale model can be obtained by separating variables into large-scale and small-scale components and considering the interactions between these two components. This gives rise to a system of coupled equations for large and small scales. An important feature of the multiscale formulation is that no closure assumption is required and no unknown parameters need to be determined. Therefore, it provides a self-consistent multiscale system that captures the dynamic interaction between the mean velocities and the small-scale velocities. This multiscale technique has been successfully applied to 3D incompressible Navier-Stokes equations with multiscale initial data (Hou *et al.*, 2008). It couples the large-scale solution to a subgrid cell problem. The computational cost for this coupled system of equations is still quite high, although an adaptive scheme has been developed to speed up the computation.

In the multiscale model, the Reynolds stress term is expressed as the average of the tensor product of the small-scale velocities, which are the solutions of a local periodic cell problem. By using the frame invariance property of the cell problem and an iterative homogenization of large- and small-scale solutions dynamically, we reveal a crucial structure of the Reynolds stress. This special structure enables us to obtain an explicit form of the Reynolds stress. To the best of our knowledge, this is the first time that a linear constitutive relation between the Reynolds stress and the strain rate has been established by combining a systematic mathematical derivation with physical arguments.

For homogeneous turbulence, we are able to recover the Smagorinsky model under minimal assumptions, while a simplified Smagorinsky model can be derived given the special structure of turbulent channel flow.

We also use a second order approximation of the inverse flow map to obtain a nonlinear model. This nonlinear model can capture the phenomena of dispersion and backscatter of kinetic energy. In addition, it covers the mixed model, which combines the Smagorinsky model and the gradient model. Careful comparison reveals the consistency of our nonlinear model with the generic nonlinear model of Lund & Novikov (1992).

In Chapter 3, an extensive numerical study is performed to validate the simplified model for turbulent channel flow by using some well-established benchmark tests. Good qualitative agreements are shown for various statistical quantities of channel flow. These include mean velocity profiles, r.m.s. velocity and vorticity fluctuations, turbulent kinetic energy budget, etc. However, we do observe some noticeable differences among the results obtained from the simplified model, DNS, and experiments, especially in the profiles of r.m.s. vorticity fluctuations near the wall. There are two error sources that could contribute to these discrepancies. The first one is due to measurement (hot wire) errors near the wall (Kim *et al.*, 1987). The second one is the modeling error, which will be discussed in detail in Chapter 3.

1.3 Turbulence modeling via the data-driven stochastic method

Due to its high irregularity, turbulent flow could be characterized by stochastic processes. There has been growing interest and significant progress over the past decades in the area of stochastic partial differential equations (sPDEs). Consequently, many methods have been devised to solve sPDEs accurately and efficiently. Recently, the generalized polynomial chaos (gPC) method has been developed and is receiving more and more attention (Xiu & Karniadakis, 2002). The types of polynomials used in the gPC method are chosen empirically according to the distributions of the input random parameters. A list of commonly used polynomials associated with different distributions of the random input is given in the book by Xiu (2010). However, if the stochastic systems are highly nonlinear and correlated, there is no guarantee that the correspondence between the distribution of the random input and the type of orthogonal polynomials remains valid.

Usually, the probabilistic dimensionality of a stochastic system is extremely high. The Karhunen-Loève (K-L) expansion (see Loève, 1977, for example) is one of the most widely used techniques for dimension reduction in representing random processes. Let $Y(\omega)$ be a stochastic process with random variable ω. The K-L expansion of Y is

$$Y(\omega, \boldsymbol{x}) = \bar{Y}(\boldsymbol{x}) + \sum_{i=1}^{\infty} \sqrt{\lambda_i}\psi_i(\boldsymbol{x})A_i(\omega), \tag{1.3.1}$$

where $\bar{Y}(\boldsymbol{x})$ is the mean and $\psi_i(\boldsymbol{x})$ and λ_i are the eigen-pairs of the covariance $\mathrm{Cov}[Y(\omega, \boldsymbol{x}), Y(\omega, \mathbf{y})]$. Inspired by the multiscale finite element method (Hou & Wu, 1997) and the proper orthogonal decomposition (POD) method (Sirovich, 1987; Venturi *et al.*, 2008), a new algorithm named the data-driven stochastic method (DDSM) has been proposed (Cheng *et al.*, 2011) and successfully combined with (adaptive) ANOVA to address the issue of high dimensionality in random space (Hu *et al.*, 2012). Efforts have been taken to construct gPC bases under which the stochastic solutions have a sparse decomposition based on Karhunen-Loève (K-L) expansion.

The DDSM algorithm consists of two parts: the offline and the online parts. In the offline part, an approximately complete subset of mutually orthogonal gPC bases $\{A_i(\omega)\}$ is obtained based on K-L expansion. In the online part, the stochastic solutions are projected onto the subspace spanned by gPC bases, and the coefficient functions in the K-L expansion are obtained by solving a coupled deterministic system.

1.3.1 Numerical results of turbulence modeling based on DDSM

In Chapter 4, we extend the DDSM to the simulation of fully developed turbulence. Specifically, we study the channel flows with random initial data. If we decompose the velocity field using K-L expansion, the number of dominant terms remains prohibitively large. The main idea of turbulence modeling via DDSM is based on the observation that once flows enter the fully developed regime, the dimensions of certain statistical structures become small. A prominent example is the famous Kolmogorov -5/3 law for the energy spectrum of the intermediate scales of high-Reynolds-number flows that are ideally homogeneous and isotropic. Since the statistical quantities of

turbulent flows are the central focus of attention, it is sensible to calculate the gPC bases from the statistical intensities.

The gPC bases based on the mean velocity profile are obtained. It is shown that the corresponding eigen-values decay fast enough so that only around 10 bases are needed in the K-L expansion. Then, the velocities are projected onto the subspace spanned by these gPC bases and the system of equations is solved to obtain approximate samples of $\boldsymbol{u}(t, \boldsymbol{x}, \omega)$. We also check two potential factors that may affect the accuracy of this algorithm. The first factor is the number and type of the gPC bases; the second one is the resolution of velocity coefficients $\boldsymbol{u}_i(t, \boldsymbol{x})$ in the K-L expansion. It turns out that the number and type of gPC base have only marginal effect on this DDSM algorithm. On the other hand, a slightly higher resolution, which is the grid size of LES, does improve the accuracy of r.m.s. velocity fluctuation, especially the normal component, pronouncedly. That is, in the near-wall region, the flow structures need to be resolved to certain level. Overall, the DDSM offers decent approximation with low resolution and a relatively small number of gPC bases.

Chapter 2

Turbulence modeling via multiscale analysis

Computing 3D incompressible flows at high Reynolds number is very challenging due to the huge number of degrees of freedom. Developing an effective turbulence model that captures the large-scale behavior of turbulent flows is essential in many engineering applications. The objective of this chapter is to find a systematic way to obtain turbulent models using a multiscale analysis developed by Hou *et al.* (2005, 2008). This multiscale analysis was developed for 3D homogeneous incompressible Euler and Navier-Stokes equations using a semi-Lagrangian point of view. A multiscale system was obtained by separating the variables into large-scale and small-scale components. This multiscale technique has been successfully applied to 3D incompressible Navier-Stokes equations with multiscale initial data. The multiscale analysis couples the large-scale solution to a subgrid cell problem. The computational cost for this coupled system of equations is still quite high, although an adaptive scheme has been developed to speed up the computation. The ultimate objective of multiscale analysis of turbulent flows is to develop an approximate closure model without the need to solve the cell problems. This will lead to the development of a multiscale model with a computational cost comparable to that of LES turbulence models.

In the multiscale model, the Reynolds stress term can be expressed as the mean of the tensor product of the small-scale velocities with respective to the small scale component. These small-scale velocities are the solutions of local periodic cell problems. By taking advantage of the frame invariance property of the cell problems and an iterative homogenization of large- and small-scale solutions dynamically, we

reveal a crucial structure of the Reynolds stress. This special structure enables us to obtain an explicit form for the Reynolds stress in turbulent flows with the aid of some mild physical assumptions. To the best of our knowledge, this is the first time that a linear constitutive relation between the Reynolds stress and the strain rate has been established by combining systematic mathematical derivation and physical arguments. Moreover, we take second order approximation of the inverse flow map function to obtain a nonlinear model, which could model the effects of anti-cascade of kinetic energy and dispersion.

2.1 Multiscale analysis for the 3D Navier-Stokes equations

First, we review the multiscale analysis for the Navier-Stokes equations. Based on the multiscale analysis by Hou-Yang-Ran (Hou *et al.*, 2005, 2008, hereafter referred to as HYR), we can formally formulate a multiscale system for the incompressible 3D Navier-Stokes equation as a homogenization problem with ϵ being a reference wave length as follows:

$$\partial_t \boldsymbol{u}^\epsilon + (\boldsymbol{u}^\epsilon \cdot \nabla)\boldsymbol{u}^\epsilon + \nabla p^\epsilon = \nu \Delta \boldsymbol{u}^\epsilon, \tag{2.1.1a}$$

$$\nabla \cdot \boldsymbol{u}^\epsilon = 0, \tag{2.1.1b}$$

$$\boldsymbol{u}^\epsilon|_{t=0} = \boldsymbol{U}(\boldsymbol{x}) + \boldsymbol{W}(\boldsymbol{x}, \boldsymbol{z}), \tag{2.1.1c}$$

where $\boldsymbol{u}^\epsilon(\boldsymbol{x}, t)$ and $p^\epsilon(\boldsymbol{x}, t)$ are the velocity field and the pressure, respectively, and $\boldsymbol{z} = \boldsymbol{x}/\epsilon$. The initial velocity field $\boldsymbol{u}^\epsilon(\boldsymbol{x}, 0)$ can be reparameterized in a formal two-scale structure, and is separated into a mean component $\boldsymbol{U}(\boldsymbol{x})$ and a high-frequency component $\boldsymbol{W}(\boldsymbol{x}, \boldsymbol{z})$. In general, $\boldsymbol{W}(\boldsymbol{x}, \boldsymbol{z})$ is periodic in $\boldsymbol{z}$ with mean zero, i.e.,

$$\langle \boldsymbol{W} \rangle \equiv \int \boldsymbol{W}(\boldsymbol{x}, \boldsymbol{z})\, d\boldsymbol{z} = \boldsymbol{0}.$$

In Appendix B, the reparameterization technique of the initial velocity $\boldsymbol{u}^\epsilon(\boldsymbol{x}, 0)$ into a two-scale structure for turbulent channel flow is illustrated in detail. Here, the mean component $\boldsymbol{U}(\boldsymbol{x})$ and the high-frequency component $\boldsymbol{W}(\boldsymbol{x}, \boldsymbol{z})$ depend on the reference scale ϵ. If we take the limit $\epsilon \to 0$, $\boldsymbol{W}(\boldsymbol{x}, \boldsymbol{z})$ will tend to zero and the mean

velocity $\boldsymbol{U}(\boldsymbol{x})$ will recover the full velocity field, which contains all of the scales.

In the analysis of the multiscale solution structure for Euler and Navier-Stokes equations, the key idea is to use a nested multiscale expansion to characterize the propagation of the small scales or the high frequency component $\boldsymbol{W}(\boldsymbol{x}, \boldsymbol{z})$. The first attempt to use homogenization theory to study the 3D Euler equations with highly oscillating data was carried out by McLaughlin *et al.* (1985). To construct a multiscale expansion for the Euler equations, they made the assumption that the oscillation is convected by the mean flow. However, Hou *et al.* performed a detailed study using the vorticity-stream function formulation (see Hou *et al.*, 2005, 2008), and found that the small-scale information is in fact propagated by the full velocity $\boldsymbol{u}^\epsilon$, which is consistent with Taylor's hypothesis (Zaman & Hussain, 1981). To be specific, define a multiscale phase function $\boldsymbol{\theta}^\epsilon(t, \boldsymbol{x})$ as follows:

$$\frac{\partial \boldsymbol{\theta}^\epsilon}{\partial t} + (\boldsymbol{u}^\epsilon \cdot \nabla)\boldsymbol{\theta}^\epsilon = \mathbf{0}, \tag{2.1.2a}$$

$$\boldsymbol{\theta}^\epsilon|_{t=0} = \boldsymbol{x}, \tag{2.1.2b}$$

which is also called the inverse flow map. Using this multiscale phase function, HYR characterized the evolution of the small-scale velocity field.

Based on a careful multiscale analysis in the Lagrangian coordinate, HYR obtained the following nested multiscale expansion for $\boldsymbol{\theta}^\epsilon$:

$$\boldsymbol{\theta}^\epsilon = \bar{\boldsymbol{\theta}}(t, \boldsymbol{x}, \tau) + \epsilon\tilde{\boldsymbol{\theta}}(t, \bar{\boldsymbol{\theta}}, \tau, \bar{\boldsymbol{\theta}}/\epsilon), \tag{2.1.3}$$

where $\tau = t/\epsilon$. By making a change of variables to simplify the computation of the cell problem, the following multiscale expansions for $(\boldsymbol{u}^\epsilon, p^\epsilon)$ are proposed:

$$\boldsymbol{u}^\epsilon = \bar{\boldsymbol{u}}(t, \boldsymbol{x}, \tau) + \tilde{\boldsymbol{u}}(t, \bar{\boldsymbol{\theta}}, \tau, \boldsymbol{z}), \tag{2.1.4a}$$

$$p^\epsilon = \bar{p}(t, \boldsymbol{x}, \tau) + \tilde{p}(t, \bar{\boldsymbol{\theta}}, \tau, \boldsymbol{z}), \tag{2.1.4b}$$

where $\tau = t/\epsilon$, $\boldsymbol{z} = \bar{\boldsymbol{\theta}}/\epsilon$, $(\bar{\boldsymbol{u}}, \bar{p})$ and $\bar{\boldsymbol{\theta}}$ are total mean components including high order terms, and $\tilde{\boldsymbol{u}}$ and $\tilde{p}$ are periodic in $\boldsymbol{z}$ with zero mean.

Remark 2.1.1. *After representing in a formal two-scale reparameterization in* (2.1.4)*,*

t, τ, $\boldsymbol{x}$ and $\boldsymbol{z}$ are regarded as independent variables.

Then, substituting the expansions (2.1.4) into the Navier-Stokes system (2.1.1) and averaging with respect to $\boldsymbol{z}$, the averaged equations for the mean velocity field $\bar{\boldsymbol{u}}(t, \boldsymbol{x}, \tau)$ with initial and proper boundary conditions are obtained:

$$\bar{\partial}_t \bar{\boldsymbol{u}} + (\bar{\boldsymbol{u}} \cdot \nabla_{\boldsymbol{x}})\bar{\boldsymbol{u}} + \nabla_{\boldsymbol{x}} \bar{p} + \nabla_{\boldsymbol{x}} \cdot \langle \tilde{\boldsymbol{u}} \otimes \tilde{\boldsymbol{u}} \rangle = \nu \nabla_{\boldsymbol{x}}^2 \bar{\boldsymbol{u}} \tag{2.1.5a}$$

$$\nabla_{\boldsymbol{x}} \cdot \bar{\boldsymbol{u}} = 0, \tag{2.1.5b}$$

$$\bar{\boldsymbol{u}}|_{t=0} = \boldsymbol{U}(\boldsymbol{x}), \tag{2.1.5c}$$

where $\bar{\partial}_t = \partial_t + \epsilon^{-1}\partial_\tau$. The additional term $\langle \tilde{\boldsymbol{u}} \otimes \tilde{\boldsymbol{u}} \rangle$ in the averaged equation (2.1.5a) is the well-known Reynolds stress. How the Reynolds stress term is modeled is of importance in both theoretical understanding and engineering applications of turbulent flows.

Next, substituting the expansion (2.1.3) into (2.1.2) and averaging over $\boldsymbol{z}$ gives us the averaged equations for $\bar{\boldsymbol{\theta}}(t, \boldsymbol{x}, \tau)$ with proper initial and boundary conditions:

$$\bar{\partial}_t \bar{\boldsymbol{\theta}} + (\bar{\boldsymbol{u}} \cdot \nabla_{\boldsymbol{x}})\bar{\boldsymbol{\theta}} + \epsilon \nabla_{\boldsymbol{x}} \cdot \langle \tilde{\boldsymbol{\theta}} \otimes \tilde{\boldsymbol{u}} \rangle = \boldsymbol{0}, \tag{2.1.6a}$$

$$\bar{\boldsymbol{\theta}}|_{t=0} = \boldsymbol{x}. \tag{2.1.6b}$$

We would like to emphasize that in Eq. (2.1.5a), $\bar{\boldsymbol{u}}(t, \boldsymbol{x}, \tau)$ and $\tilde{\boldsymbol{u}}(t, \theta, \tau, \boldsymbol{z})$ are functions of τ. After averaging over $\boldsymbol{z}$, the Reynolds stress term is still τ dependent. In order to make the Reynolds stress independent on τ, we make the following assumption:

Assumption 2.1.2. *We assume that the turbulent flows are weakly ergodic. Since we perform space average for the Reynolds stress, it is expected that the average should have a short correlation length in time. If we denote Δt as the characteristic correlation time, then we expect the time-average of the Reynolds stress over Δt has a weak dependence on τ.*

To simplify the model further, we consider only the leading order terms of the

large-scale variables $(\bar{\boldsymbol{u}}, \bar{p}, \bar{\boldsymbol{\theta}})$. We are looking for the following expansion:

$$\bar{\boldsymbol{u}}(t, \boldsymbol{x}, \tau) = \boldsymbol{u}(t, \boldsymbol{x}) + \epsilon \boldsymbol{u}_1(t, \boldsymbol{x}, \tau), \tag{2.1.7a}$$

$$\bar{p}(t, \boldsymbol{x}, \tau) = p(t, \boldsymbol{x}) + \epsilon p_1(t, \boldsymbol{x}, \tau), \tag{2.1.7b}$$

$$\bar{\boldsymbol{\theta}}(t, \boldsymbol{x}, \tau) = \boldsymbol{\theta}(t, \boldsymbol{x}) + \epsilon \boldsymbol{\theta}_1(t, \boldsymbol{x}, \tau), \tag{2.1.7c}$$

and small-scale variables $(\tilde{\boldsymbol{u}}, \tilde{p}, \tilde{\boldsymbol{\theta}})$,

$$\tilde{\boldsymbol{u}} = \boldsymbol{w}(t, \bar{\boldsymbol{\theta}}, \tau, \boldsymbol{z}) + O(\epsilon), \tag{2.1.8a}$$

$$\tilde{p} = q(t, \bar{\boldsymbol{\theta}}, \tau, \boldsymbol{z}) + O(\epsilon), \tag{2.1.8b}$$

$$\tilde{\boldsymbol{\theta}} = \boldsymbol{\Theta}(t, \bar{\boldsymbol{\theta}}, \tau, \boldsymbol{z}) + O(\epsilon). \tag{2.1.8c}$$

Plugging the above expansions (2.1.7) and (2.1.8) into Eqs. (2.1.5) and (2.1.6) and keeping the leading order of ϵ, we have the equations

$$\partial_t \boldsymbol{u} + (\boldsymbol{u} \cdot \nabla_{\boldsymbol{x}})\boldsymbol{u} + \nabla_{\boldsymbol{x}} p + \nabla_{\boldsymbol{x}} \cdot \langle \boldsymbol{w} \otimes \boldsymbol{w} \rangle = \nu \nabla_{\boldsymbol{x}}^2 \boldsymbol{u} \tag{2.1.9a}$$

$$\nabla_{\boldsymbol{x}} \cdot \boldsymbol{u} = 0, \tag{2.1.9b}$$

$$\boldsymbol{u}|_{t=0} = \boldsymbol{U}(\boldsymbol{x}), \tag{2.1.9c}$$

for large-scale velocity $\boldsymbol{u}$ and

$$\partial_t \boldsymbol{\theta} + (\boldsymbol{u} \cdot \nabla_{\boldsymbol{x}})\boldsymbol{\theta} = \boldsymbol{0}, \tag{2.1.10a}$$

$$\boldsymbol{\theta}|_{t=0} = \boldsymbol{x}. \tag{2.1.10b}$$

for large-scale inverse flow map θ.

Let Δt to be the typical time length and $\Delta\tau = \Delta t/\epsilon$, and define $[f]^*_{\Delta\tau}$ to be the local time-average given by

$$[f]^*_{\Delta\tau} = \frac{1}{\Delta\tau} \int_{\tau}^{\tau+\Delta\tau} f \mathrm{d}\tau.$$

In Eq. (2.1.9a), the Reynolds stress $\langle \boldsymbol{w} \otimes \boldsymbol{w} \rangle$ is still dependent on fast time τ. By Assumption 2.1.2, the local time-average of the Reynolds stress is independent on τ. Therefore, after a local time-average of Eq. (2.1.9), we have the following simplified

averaged equations for large-scale velocity $\boldsymbol{u}$, up to the first order of ϵ,

$$\partial_t \boldsymbol{u} + (\boldsymbol{u} \cdot \nabla_{\boldsymbol{x}})\boldsymbol{u} + \nabla_{\boldsymbol{x}} p + \nabla_{\boldsymbol{x}} \cdot \langle [\boldsymbol{w} \otimes \boldsymbol{w}]^*_{\Delta\tau} \rangle = \nu \nabla^2_{\boldsymbol{x}} \boldsymbol{u} \tag{2.1.11a}$$

$$\nabla_{\boldsymbol{x}} \cdot \boldsymbol{u} = 0, \tag{2.1.11b}$$

$$\boldsymbol{u}|_{t=0} = \boldsymbol{U}(\boldsymbol{x}). \tag{2.1.11c}$$

Then we subtract the averaged equations from the Navier-Stokes equation (2.1.1) and the equations for the inverse flow map $\boldsymbol{\theta}^\epsilon$ (2.1.2). After some algebraic operations, we obtain the equations for the small-scale variables, to the leading order approximation:

$$\partial_\tau \boldsymbol{w} + D_{\boldsymbol{z}} \boldsymbol{w} \mathcal{A} \boldsymbol{w} + \mathcal{A}^{\mathsf{T}} \nabla_{\boldsymbol{z}} q - \frac{\nu}{\epsilon} \nabla \cdot (\mathcal{A}\mathcal{A}^{\mathsf{T}} \nabla_{\boldsymbol{z}} \boldsymbol{w}) = \boldsymbol{0}, \tag{2.1.12a}$$

$$(\mathcal{A}^{\mathsf{T}} \nabla_{\boldsymbol{z}}) \cdot \boldsymbol{w} = \boldsymbol{0}, \tag{2.1.12b}$$

$$\boldsymbol{w}|_{t=0} = \boldsymbol{W}(\boldsymbol{x}, \boldsymbol{z}), \tag{2.1.12c}$$

where $\mathcal{A}$ is the gradient of the phase function $\boldsymbol{\theta}$, i.e. , $\mathcal{A} = D_{\boldsymbol{x}} \boldsymbol{\theta}$, which measures the deformation rate of the flow.

Remark 2.1.3. *The details of the above multiscale analysis technique are elaborated in Appendix A.*

Remark 2.1.4. *An important feature of the above multiscale formulation* (2.1.11) - (2.1.12)*, including the equations for both large-scale and high-frequency variables, is that we do not need any closure assumption; thus no unknown parameters need to be determined, in contrast to other models, e.g. , the Smagorinsky model. The multiscale formulation provides a self-consistent system that captures the interaction between large-scale and small-scale fields. The computational cost of this coupled system of equations is still quite high, although an adaptive scheme has been developed to speed up the computation, (see Hou* et al.*, 2008, for a numerical example of homogeneous turbulent flows).*

Remark 2.1.5. *For the convenience of theoretical analysis and numerical implementation, the cell problems* (2.1.12) *can be further simplified by making a change of variables from $\boldsymbol{w}$ to $\tilde{\boldsymbol{w}}$ by letting $\tilde{\boldsymbol{w}} = \mathcal{A}\boldsymbol{w}$. The $\tilde{\boldsymbol{w}}$ satisfies the following modified*

cell problems:

$$\partial_\tau \tilde{\boldsymbol{w}} + (\tilde{\boldsymbol{w}} \cdot \nabla_{\boldsymbol{z}})\tilde{\boldsymbol{w}} + \mathcal{B}\nabla_{\boldsymbol{z}} q - \frac{\nu}{\epsilon}\nabla \cdot (\mathcal{B}\nabla_{\boldsymbol{z}}\tilde{\boldsymbol{w}}) = \mathbf{0}, \tag{2.1.13a}$$

$$\nabla_{\boldsymbol{z}} \cdot \tilde{\boldsymbol{w}} = \mathbf{0}, \tag{2.1.13b}$$

$$\tilde{\boldsymbol{w}}|_{t=0} = \mathcal{A}\boldsymbol{W}(\boldsymbol{x}, \boldsymbol{z}). \tag{2.1.13c}$$

where $\mathcal{B} = \mathcal{A}\mathcal{A}^{\mathsf{T}}$.

2.2 Mathematical derivation of turbulence models

Considering that the model (2.1.11)–(2.1.12) needs considerable computational CPU time and memory storage, we would like to develop a simplified multiscale model for turbulent flows. On one hand, the new model has a comparable computational complexity with the other turbulence models. On the other hand, the simplified multiscale model requires minimal closure assumptions.

First of all, we state the Rivlin-Ericksen Theorem, which plays an essential role in the mathematical development of the turbulence models.

Theorem 2.2.1 (Rivlin-Ericksen)**.** *To be frame invariant, the only possible form for a symmetric matrix R, function of another symmetric matrix $B \in \mathbb{R}^{d\times d}$, is*

$$R(B) = \beta_0(i_B)I + \beta_1(i_B)B + \cdots + \beta_{d-1}(i_B)B^{d-1},$$

where d is the dimensionality and $\beta_0, \beta_1, \cdots, \beta_{d-1}$ are real-valued functions of the principal invariants i_B of the matrix B.

A complete proof of the Rivlin-Ericksen can be found in the book by Ciarlet (1988).

Lemma 2.2.2. *Let $\tilde{\boldsymbol{w}}$ be the solution to the modified cell problems* (2.1.13)*, then the tensor $\mathcal{R}_m = \langle[\tilde{\boldsymbol{w}} \otimes \tilde{\boldsymbol{w}}]^*_{\Delta\tau}\rangle$ can be expressed as follows:*

$$\langle[\tilde{\boldsymbol{w}} \otimes \tilde{\boldsymbol{w}}]^*_{\Delta\tau}\rangle(\mathcal{B}) = a_0\mathcal{I} + a_1\mathcal{B} + a_2\mathcal{B}^2, \tag{2.2.1}$$

where $\mathcal{I}$ is the identity matrix and the coefficients a_0, a_1, a_2 are real-valued functions of the principal invariants of $\mathcal{B}$.

Proof. The proof relies on frame invariance, which is the property that the model should yield results independent of reference. It has been shown that Navier-Stokes equations and the averaged equations (2.1.11) are frame-invariant (Mohammadi & Pironneau, 1994). We need to show that the modified cell problems (2.1.13) are also frame-invariant. Keep in mind that we are working in three-dimensional space for both the averaged equations and the cell problems (2.1.13).

Then, we check that the modified cell problems (2.1.13) are frame-invariant.

(i) Transitional invariance: suppose $\boldsymbol{z} = \boldsymbol{y} + \boldsymbol{Z}$, where $\boldsymbol{Z}$ is a constant vector of R^3. Then

$$\frac{\mathrm{d}\boldsymbol{z}}{\mathrm{d}\tau} = \tilde{\boldsymbol{w}}(\boldsymbol{z}, \tau, \boldsymbol{x}, t) = \frac{\mathrm{d}\boldsymbol{y}}{\mathrm{d}\tau}, \quad \frac{\partial \tilde{\boldsymbol{w}}}{\partial z_i} = \frac{\partial \tilde{\boldsymbol{w}}}{\partial y_i}.$$

In $(\boldsymbol{z}, \tau)$, the small-scale velocity is $\tilde{\boldsymbol{w}}(\boldsymbol{z}, \tau, \boldsymbol{x}, t)$ and it satisfies the modified cell problems (2.1.13).

In $(\boldsymbol{y}, \tau)$, the small-scale velocity is $\tilde{\boldsymbol{v}}(\boldsymbol{y}, \tau, \boldsymbol{x}, t)$. Hence it verifies

$$\begin{aligned}
\mathbf{0} &= \left[\partial_\tau \tilde{\boldsymbol{w}} + (\tilde{\boldsymbol{w}} \cdot \nabla_{\boldsymbol{z}})\tilde{\boldsymbol{w}} + \mathcal{B}\nabla_{\boldsymbol{z}} q - \frac{\nu}{\epsilon}\nabla \cdot (\mathcal{B}\nabla_{\boldsymbol{z}} \tilde{\boldsymbol{w}})\right]_{\boldsymbol{z}=\boldsymbol{y}+\boldsymbol{Z}} \\
&= \partial_\tau \tilde{\boldsymbol{v}} + (\tilde{\boldsymbol{v}} \cdot \nabla_{\boldsymbol{y}})\tilde{\boldsymbol{v}} + \mathcal{B}\nabla_{\boldsymbol{y}} q - \frac{\nu}{\epsilon}\nabla_{\boldsymbol{y}} \cdot (\mathcal{B}\nabla_{\boldsymbol{y}} \tilde{\boldsymbol{v}}), \\
\nabla_{\boldsymbol{z}} \cdot \tilde{\boldsymbol{w}}|_{\boldsymbol{z}=\boldsymbol{y}+\boldsymbol{Z}} &= \nabla_{\boldsymbol{y}} \cdot \tilde{\boldsymbol{v}} = \mathbf{0}.
\end{aligned}$$

Therefore, the cell problems (2.1.13) are invariant with respect to translation.

(ii) Galilean invariance: suppose $\boldsymbol{z} = \boldsymbol{y} + \hat{\tilde{\boldsymbol{v}}}\tau$, where $\hat{\tilde{\boldsymbol{v}}}$ is a constant vector. Then

$$\frac{\mathrm{d}\boldsymbol{z}}{\mathrm{d}\tau} = \tilde{\boldsymbol{w}}(\boldsymbol{z}, \tau, \boldsymbol{x}, t) = \tilde{\boldsymbol{w}}(\boldsymbol{y} + \hat{\tilde{\boldsymbol{v}}}\tau, \tau, \boldsymbol{x}, t) = \frac{\mathrm{d}\boldsymbol{y}}{\mathrm{d}\tau} + \hat{\tilde{\boldsymbol{v}}} = \tilde{\boldsymbol{v}} + \hat{\tilde{\boldsymbol{v}}},$$

so let $\tilde{\boldsymbol{v}}(\boldsymbol{y}, \tau, \boldsymbol{x}, t) = \tilde{\boldsymbol{w}}(\boldsymbol{y} + \hat{\tilde{\boldsymbol{v}}}\tau, \tau, \boldsymbol{x}, t) - \hat{\tilde{\boldsymbol{v}}}$.

Note that $\partial_\tau \tilde{\boldsymbol{v}} = \partial_\tau(\tilde{\boldsymbol{w}} - \hat{\tilde{\boldsymbol{v}}}) + (\hat{\tilde{\boldsymbol{v}}} \cdot \nabla_{\boldsymbol{z}})\tilde{\boldsymbol{w}} = \partial_\tau \tilde{\boldsymbol{w}} + (\hat{\tilde{\boldsymbol{v}}} \cdot \nabla_{\boldsymbol{z}})\tilde{\boldsymbol{w}}$. The cell problems

for $\tilde{\boldsymbol{v}}$ become

$$\begin{aligned}
&\partial_\tau \tilde{\boldsymbol{v}} + (\tilde{\boldsymbol{v}} \cdot \nabla_{\boldsymbol{y}})\tilde{\boldsymbol{v}} + \mathcal{B}\nabla_{\boldsymbol{y}} q - \frac{\nu}{\epsilon}\nabla_{\boldsymbol{y}} \cdot (\mathcal{B}\nabla_{\boldsymbol{y}}\tilde{\boldsymbol{v}}) \\
=&\partial_\tau \tilde{\boldsymbol{w}} + (\hat{\tilde{\boldsymbol{v}}} \cdot \nabla_{\boldsymbol{z}})\tilde{\boldsymbol{w}} + ((\tilde{\boldsymbol{w}} - \hat{\tilde{\boldsymbol{v}}}) \cdot \nabla_{\boldsymbol{z}})(\tilde{\boldsymbol{w}} - \hat{\tilde{\boldsymbol{v}}}) + \mathcal{B}\nabla_{\boldsymbol{z}} q - \frac{\nu}{\epsilon}\nabla_{\boldsymbol{z}} \cdot (\mathcal{B}\nabla_{\boldsymbol{z}}(\tilde{\boldsymbol{w}} - \hat{\tilde{\boldsymbol{v}}})) \\
=&\partial_\tau \tilde{\boldsymbol{w}} + (\hat{\tilde{\boldsymbol{w}}} \cdot \nabla_{\boldsymbol{z}})\tilde{\boldsymbol{w}} + \mathcal{B}\nabla_{\boldsymbol{z}} q - \frac{\nu}{\epsilon}\nabla_{\boldsymbol{z}} \cdot (\mathcal{B}\nabla_{\boldsymbol{z}}\tilde{\boldsymbol{w}}) = \mathbf{0}, \\
&\nabla_{\boldsymbol{y}} \cdot \tilde{\boldsymbol{v}} = \nabla_{\boldsymbol{z}} \cdot (\tilde{\boldsymbol{w}} - \hat{\tilde{\boldsymbol{v}}}) = \nabla_{\boldsymbol{z}} \cdot \tilde{\boldsymbol{w}} = \mathbf{0}.
\end{aligned}$$

Therefore, the cell problems (2.1.13) are Galilean invariant.

(iii) Rotation invariance: Let M be a rotational matrix, that is

$$MM^T = M^T M = \mathcal{I}.$$

Let $\boldsymbol{z} = M\boldsymbol{y}$ and $\hat{\tilde{\boldsymbol{v}}}$ denote the small-scale velocity in the $\boldsymbol{y}$ variable,

$$\tilde{\boldsymbol{w}} = \frac{\mathrm{d}\boldsymbol{z}}{\mathrm{d}\tau} = M\frac{\mathrm{d}\boldsymbol{y}}{\mathrm{d}\tau} = M\hat{\tilde{\boldsymbol{v}}};$$

and for any f we have

$$\frac{\partial f}{\partial z_i} = \frac{\partial f}{\partial y_j}\frac{\partial y_j}{\partial z_i} = \frac{\partial f}{\partial y_j}M^T_{ji}, \text{ that is } \nabla_{\boldsymbol{z}} f = M\nabla_{\boldsymbol{y}} f.$$

Consequently,

$$\nabla_{\boldsymbol{z}}\tilde{\boldsymbol{w}} = (M\nabla_{\boldsymbol{y}})M\hat{\tilde{\boldsymbol{v}}} = M\nabla_{\boldsymbol{y}}\hat{\tilde{\boldsymbol{v}}}M^T.$$

Hence

$$\begin{aligned}
\mathbf{0} =&\partial_\tau \tilde{\boldsymbol{w}} + (\hat{\tilde{\boldsymbol{w}}} \cdot \nabla_{\boldsymbol{z}})\tilde{\boldsymbol{w}} + \mathcal{B}\nabla_{\boldsymbol{z}} q - \frac{\nu}{\epsilon}\nabla_{\boldsymbol{z}} \cdot (\mathcal{B}\nabla_{\boldsymbol{z}}\tilde{\boldsymbol{w}}) \\
=&M\partial_\tau \hat{\tilde{\boldsymbol{v}}} + (M\hat{\tilde{\boldsymbol{v}}}) \cdot [(M\nabla_{\boldsymbol{y}})M\hat{\tilde{\boldsymbol{v}}}] + M\nabla_{\boldsymbol{y}}(\mathcal{B}q) - \frac{\nu}{\epsilon}(M\nabla_{\boldsymbol{y}}) \cdot (M\nabla_{\boldsymbol{y}}[M\mathcal{B}\hat{\tilde{\boldsymbol{v}}}]) \\
=&M(\partial_\tau \hat{\tilde{\boldsymbol{v}}} + (\hat{\tilde{\boldsymbol{v}}} \cdot \nabla_{\boldsymbol{y}})\hat{\tilde{\boldsymbol{v}}} + \mathcal{B}\nabla_{\boldsymbol{y}} q - \frac{\nu}{\epsilon}\nabla_{\boldsymbol{y}} \cdot (\mathcal{B}\nabla_{\boldsymbol{y}}\hat{\tilde{\boldsymbol{v}}}), \\
\nabla_{\boldsymbol{z}} \cdot \tilde{\boldsymbol{w}} = (M\nabla_{\boldsymbol{y}}) \cdot M\hat{\tilde{\boldsymbol{v}}} = &M_{ij}\frac{\partial}{\partial y_j}M_{ik}\hat{\tilde{v}}_k = \nabla_{\boldsymbol{y}} \cdot \hat{\tilde{\boldsymbol{v}}} = 0.
\end{aligned}$$

Therefore, the cell problems (2.1.13) are rotation invariant.

In summary, the cell problems (2.1.13) for $\tilde{\boldsymbol{w}}$ are frame invariant.

Furthermore, the cell problems are equations of $\tilde{\boldsymbol{w}}$ with respect to τ and $\boldsymbol{z}$. $\mathcal{B}(t, \boldsymbol{x})$ can be regarded as parameters in Eqs. (2.1.13). Therefore, the solution $\tilde{\boldsymbol{w}}$ depends on this parameter $\mathcal{B}$:

$$\tilde{\boldsymbol{w}} = \tilde{\boldsymbol{w}}(\tau, \boldsymbol{z}, t, \boldsymbol{x}; \mathcal{B}).$$

After local time and space averaging w.r.t. τ and $\boldsymbol{z}$, the symmetric tensor $\langle[\tilde{\boldsymbol{w}} \otimes \tilde{\boldsymbol{w}}]^*_{\Delta\tau}\rangle$ still depends on $\mathcal{B}$:

$$\langle[\tilde{\boldsymbol{w}} \otimes \tilde{\boldsymbol{w}}]^*_{\Delta\tau}\rangle = \langle[\tilde{\boldsymbol{w}} \otimes \tilde{\boldsymbol{w}}]^*_{\Delta\tau}\rangle(t, x; \mathcal{B}).$$

Note that $\mathcal{B} = \mathcal{A}\mathcal{A}^{\mathsf{T}}$ is also a symmetric tensor. By the Rivlin-Ericksen theorem in three dimension ($d = 3$), we have the following relation in three-dimensional space:

$$\langle[\tilde{\boldsymbol{w}} \otimes \tilde{\boldsymbol{w}}]^*_{\Delta\tau}\rangle = a_0\mathcal{I} + a_1\mathcal{B} + a_2\mathcal{B}^2,$$

and the coefficients a_0, a_1, a_2 are real-valued functions of the principal invariants of $\mathcal{B}$. □

Remark 2.2.3. *At this point, we only know that all these coefficients $a_i (i = 0, 1, 2)$ are real-valued functions of the three principal invariants of $\mathcal{B}$. Nevertheless, $\mathcal{B}$ cannot be solved explicitly in order to obtain these invariants. Hence, we will approximate $\mathcal{B}$ in the following using the multiscale system that we have obtained in the previous subsection.*

In order to extract the structure of the Reynolds stress, we perform a local-in-time multiscale analysis to account for the interaction between the large and small scales through dynamic re-initialization of the phase function. The large-scale components of the solutions, $\boldsymbol{u}$ and $\boldsymbol{\theta}$, can generate small scales dynamically through convection and nonlinear interaction. In order to ensure that $\boldsymbol{u}$ contains only the large-scale components of the solutions, we decompose the multiscale solutions into local mean and high-frequency components by applying the reparameterization technique of HRY after solving the multiscale system for some characteristic time step Δt. This dynamic iterative reparameterization of the multiscale solutions enables us to capture the dynamic interaction among all small scales of the solutions. We call this procedure a

dynamic iterative homogenization. This leads to the following theorem.

Theorem 2.2.4. *To the leading order of some characteristic time length Δt, the linear relation between the Reynolds stress tensor and the strain-rate tensor is given by*

$$\mathcal{R} = \alpha\mathcal{I} - \beta\Delta t\mathcal{D} + \mathcal{O}(\Delta t^2), \tag{2.2.2}$$

where $\alpha = a_0 + a_1 + a_2$, $\beta = -2(a_0 - a_2)$, $\mathcal{I}$ is the identity matrix, and $\mathcal{D}$ is the rate of strain tensor defined as

$$\mathcal{D} = \frac{1}{2}\left(\nabla \boldsymbol{u} + \nabla \boldsymbol{u}^{\mathsf{T}}\right).$$

Proof. Note that in Eq. (2.2.1), we found the relation between $\langle[\tilde{\boldsymbol{w}} \otimes \tilde{\boldsymbol{w}}]^*_{\Delta\tau}\rangle$ and $\mathcal{B}$, where $\mathcal{B} = D_{\boldsymbol{x}}\boldsymbol{\theta}(D_{\boldsymbol{x}}\boldsymbol{\theta})^T$. In the first step, in order to obtain the linear relation between $\mathcal{R}$ and $\mathcal{D}$, we need to approximate $\mathcal{B}$ by $\mathcal{D}$. To achieve this goal, we solve the average equations (2.1.10) for the inverse phase flow $\boldsymbol{\theta}$ in a local time interval $[t, t + \Delta t]$ with $\boldsymbol{\theta}(t, \boldsymbol{x}) = \boldsymbol{x}$ as the initial condition. Using the forward Euler method, the leading order approximation of $\boldsymbol{\theta}$ is as follows:

$$\boldsymbol{\theta}(t + \Delta t, \boldsymbol{x}) = \boldsymbol{x} - \Delta t\boldsymbol{u}(t, \boldsymbol{x}) + \mathcal{O}(\Delta t^2).$$

Now it follows that the rate of deformation can be computed as

$$\mathcal{A} = D_{\boldsymbol{x}}\boldsymbol{\theta} = \mathcal{I} - \Delta t\nabla \boldsymbol{u} + \mathcal{O}(\Delta t^2),$$

and its inverse

$$\mathcal{A}^{-1} = \mathcal{I} + \Delta t\nabla \boldsymbol{u} + \mathcal{O}(\Delta t^2).$$

Therefore, $\mathcal{B}$ can be approximated up to second order in Δt as follows:

$$\mathcal{B} = \mathcal{A}\mathcal{A}^{\mathsf{T}} = \mathcal{I} - 2\Delta t\mathcal{D} + \mathcal{O}(\Delta t^2), \tag{2.2.3}$$

Plugging Eq. (2.2.3) into relation (2.2.1), we have an approximation to $\langle[\tilde{\boldsymbol{w}}\otimes\tilde{\boldsymbol{w}}]^*_{\Delta\tau}\rangle$:

$$\begin{aligned}\langle[\tilde{\boldsymbol{w}}\otimes\tilde{\boldsymbol{w}}]^*_{\Delta\tau}\rangle &= a_0\mathcal{I}+a_1\mathcal{B}+a_2\mathcal{B}^2\\ &= a_0\mathcal{I}+a_1\left(\mathcal{I}-2\Delta t\mathcal{D}+O(\Delta t^2)\right)+a_2\left(\mathcal{I}-2\Delta t\mathcal{D}+O(\Delta t^2)\right)^2\\ &= \alpha\mathcal{I}-\tilde{\beta}\Delta t\mathcal{D}+O(\Delta t^2),\end{aligned}$$

where the coefficients $\alpha=a_0+a_1+a_2$ and $\tilde{\beta}=2(a_1+2a_2)$. Keep in mind that both coefficients α and $\tilde{\beta}$ are functions of the invariants of $\mathcal{B}$.

Finally, the Reynolds stress tensor is given by

$$\begin{aligned}\mathcal{R} &= \langle[\boldsymbol{w}\otimes\boldsymbol{w}]^*_{\Delta\tau}\rangle\\ &= \langle[\mathcal{A}^{-1}\tilde{\boldsymbol{w}}\otimes\mathcal{A}^{-1}\tilde{\boldsymbol{w}}]^*_{\Delta\tau}\rangle\\ &= \langle[(\mathcal{I}+\Delta t\nabla\boldsymbol{u}+\mathcal{O}(\Delta t^2))\tilde{\boldsymbol{w}}\otimes(\mathcal{I}+\Delta t\nabla\boldsymbol{u}+\mathcal{O}(\Delta t^2))\tilde{\boldsymbol{w}}]^*_{\Delta\tau}\rangle\\ &= \langle[\tilde{\boldsymbol{w}}\otimes\tilde{\boldsymbol{w}}]^*_{\Delta\tau}\rangle+\Delta t\nabla\boldsymbol{u}\langle[\tilde{\boldsymbol{w}}\otimes\tilde{\boldsymbol{w}}]^*_{\Delta\tau}\rangle+\Delta t\langle[\tilde{\boldsymbol{w}}\otimes\tilde{\boldsymbol{w}}]^*_{\Delta\tau}\rangle\nabla u^{\mathsf{T}}+O(\Delta t^2)\\ &= \alpha\mathcal{I}-\beta\Delta t\mathcal{D}+\mathcal{O}(\Delta t^2),\end{aligned}\tag{2.2.4}$$

where $\mathrm{tr}(\mathcal{R})=\alpha/3=(a_0+a_1+a_2)/3$ is the SGS kinetic energy, and $\beta=-2(a_0-a_2)$. Both coefficients α and β are also functions of the invariants of $\mathcal{B}$. □

Remark 2.2.5. *Since $\nabla\cdot(\alpha\mathcal{I})=\nabla\alpha$, the first term $\alpha\mathcal{I}$ in Eq.* (2.2.2) *can be integrated into the pressure term in Eq.* (2.1.11a) *with a modified pressure $p'=p+\alpha$.*

Lemma 2.2.6. *The coefficient β in Eq.* (2.2.4) *is the order of $1/\Delta t$, i.e.*

$$\beta\sim\frac{1}{\Delta t}.\tag{2.2.5}$$

Proof. In the proof of Rivlin-Ericson theorem, the Reynolds stress tensor $\mathcal{R}$ and the mean strain-rate tensor $\mathcal{D}$ share the eigen-vectors $\psi_i, i=1,2,3$ (Mohammadi & Pironneau, 1994; Ciarlet, 1988). One of the corresponding eigen-values must be non-zero. Otherwise $\mathcal{R}$ and $\mathcal{D}$ are zero tensors. Assume $\mathcal{D}$'s eigen-value λ_1 is non-zero and the corresponding orthonormal eigen-vector is ψ_1. Further, we assume that μ_1 is the eigen-value of $\mathcal{R}$ related to ψ_1.

Multiplying both sides of Eq. (2.2.4) by ψ_1, we have the following approximate

relation:

$$\mathcal{R}\psi_1 = \alpha\mathcal{I}\psi_1 - \beta\Delta t\mathcal{D}\psi_1,$$
$$\mu_1\psi_1 = (\alpha - \beta\Delta t\lambda_1)\psi_1.$$

After taking the dot product with eigen-vector ψ_1 on both sides of the above equation and noticing $< \psi_1, \psi_1 >= 1$ and $\lambda_1 \neq 0$, we have

$$\mu_1 = (\alpha - \beta\Delta t\lambda_1), \quad \text{or}$$
$$\beta = \frac{\alpha - \mu_1}{\lambda_1\Delta t}.$$

Therefore, we have the following order of the coefficient β

$$\beta \sim \frac{1}{\Delta t}.$$

□

Remark 2.2.7. *It is important to note that if we take the limite $\Delta t \to 0$, the Reynolds stress tensor should not reduce to a multiple of identity matrix, which means that $\mathcal{R}$ must have any effect on the LES model* (2.1.11a). *By Lemma 2.2.6 the coefficient β is the order of $1/\Delta t$, or*

$$\beta\Delta t \sim \ 1.$$

Therefore, the term $-\beta\Delta t\mathcal{D}$ does not vanish when taking the limit $\Delta t \to 0$.

In eddy-viscosity models, the Reynolds stress tensor is assumed to be a linear functional of the strain rate tensor via the turbulent eddy viscosity

$$\tilde{\mathcal{R}}_{ij} = \mathcal{R}_{ij} - \frac{1}{3}R_{kk}\delta_{ij} = -\nu_T\mathcal{D}_{ij}, \tag{2.2.6}$$

which is a first-order approximation, as is that in (2.2.4). We remark that this linear relation between the stress and strain rate tensors is not meant to be valid as a point-wise relation, but should be understood in a statistical sense as an ensemble average. To demonstrate this, the channel flow is taken as an example. The computational settings in Kim *et al.* (1987) are adopted. The streamwise (x) and spanwise (z) com-

putational periods are chosen to be 4π and 2π, and the half-width of the channel is 1, i.e. , the computational domain is $[0, 4\pi] \times [-1, 1] \times [0, 2\pi]$. Figure 2.1 is the time average of the sign of $\tilde{\mathcal{R}}_{11}/\mathcal{D}_{11}$ at each grid point on the central plane $y = 0$, while Figure 2.2 displays the snapshot of the sign at $t = 2$. Hence, it is clear that there does not exist a positive ν_T for which equation (2.2.6) holds in a pointwise fashion.

Furthermore, the turbulent eddy viscosity ν_T is assumed to be positive, which treats the 'dissipation' of kinetic energy at sub-grid scales similar to viscous (molecular) dissipation. As a matter of fact, the Reynolds stress term reflects neither diffusion nor dissipation locally in space, but reflects equivalent, ensemble-averaged effects of turbulent fluctuations. Figure 2.3 indicates that each element of $\tilde{R}/\mathcal{D}$ alternates sign in time. This suggests that the role of the Reynolds stress changes continuously in time with a positive time-average in turbulent shear flows.

Remark 2.2.8. *In equation* (2.2.4)*, we establish a linear constitutive relation between the Reynolds stress* $\tilde{\mathcal{R}}$ *and the strain rate* $\mathcal{D}$*, up to second-order accuracy in the time step* Δt*. The first term* $\alpha\mathcal{I}$ *is not crucial since it can be incorporated into the equations of large-scale fields as a modified pressure. Thereafter, we write* $\tilde{\mathcal{R}}$ *as* $\mathcal{R}$ *for simplicity of notation. The remaining question is how to determine the coefficient* β*. In order to specify* β*, we need to know the detailed structure of the symmetric tensor* $\mathcal{B}$*. Constitutive relations necessarily involve the material make-up or constitution of the medium and must involve material properties like viscosity.*

Note that there exists a relation between $\mathcal{B}$ and $\mathcal{D}$ given in (2.2.3), so we can find the relation of the eigenvalues between $\mathcal{B}$ and $\mathcal{D}$ as follows. In three dimensions, assume λ_i and $\tilde{\lambda}_i\,(i = 1, 2, 3)$ are the eigenvalues of $\mathcal{D}$ and $\mathcal{B}$, respectively, while $\psi_i\,(i = 1, 2, 3)$ are the corresponding eigenfunctions. Then, up to the second order of Δt, we have

$$\mathcal{B}\psi_i = (\mathcal{I} - 2\Delta t\mathcal{D})\psi_i = \tilde{\lambda}_i\psi_i, \quad i = 1, 2, 3,$$

which gives

$$\mathcal{D}\psi_i = \frac{1 - \tilde{\lambda}_i}{2\Delta t}\psi_i = \lambda_i\psi_i, \quad i = 1, 2, 3,$$

or

$$\tilde{\lambda}_i = 1 - 2\Delta t\lambda_i, \quad i = 1, 2, 3. \tag{2.2.7}$$

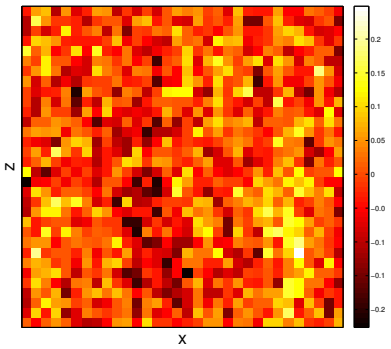

(a) $\tilde{\mathcal{R}}_{11}/\mathcal{D}_{11}$

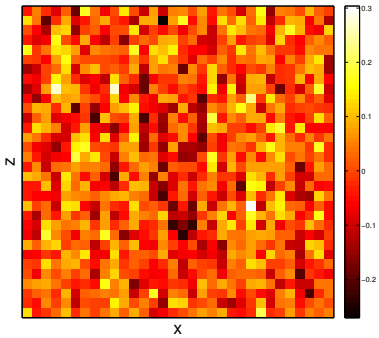

(b) $\tilde{\mathcal{R}}_{12}/\mathcal{D}_{12}$

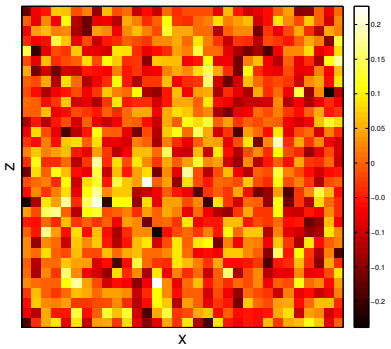

(c) $\tilde{\mathcal{R}}_{22}/\mathcal{D}_{22}$

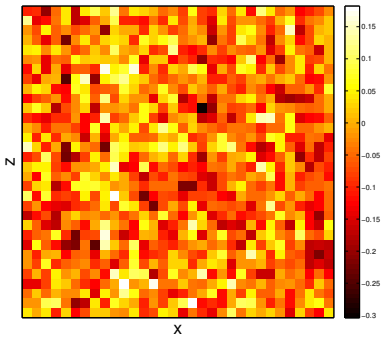

(d) $\tilde{\mathcal{R}}_{23}/\mathcal{D}_{23}$

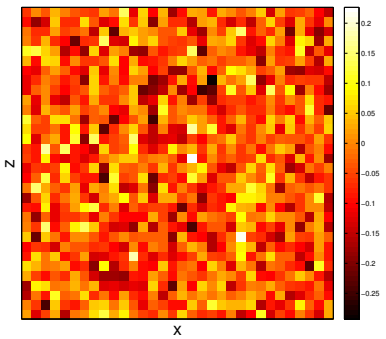

(e) $\tilde{\mathcal{R}}_{33}/\mathcal{D}_{33}$

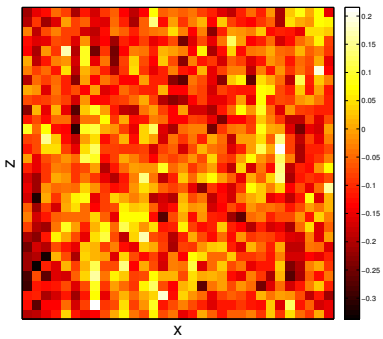

(f) $\tilde{\mathcal{R}}_{31}/\mathcal{D}_{31}$

Figure 2.1: Spatial distributions of the time-averaged sign of $\tilde{\mathcal{R}}_{11}\mathcal{D}_{11}$ on the central layer of the channel $y = 0$ for each entry of $\tilde{\mathcal{R}}/\mathcal{D}$

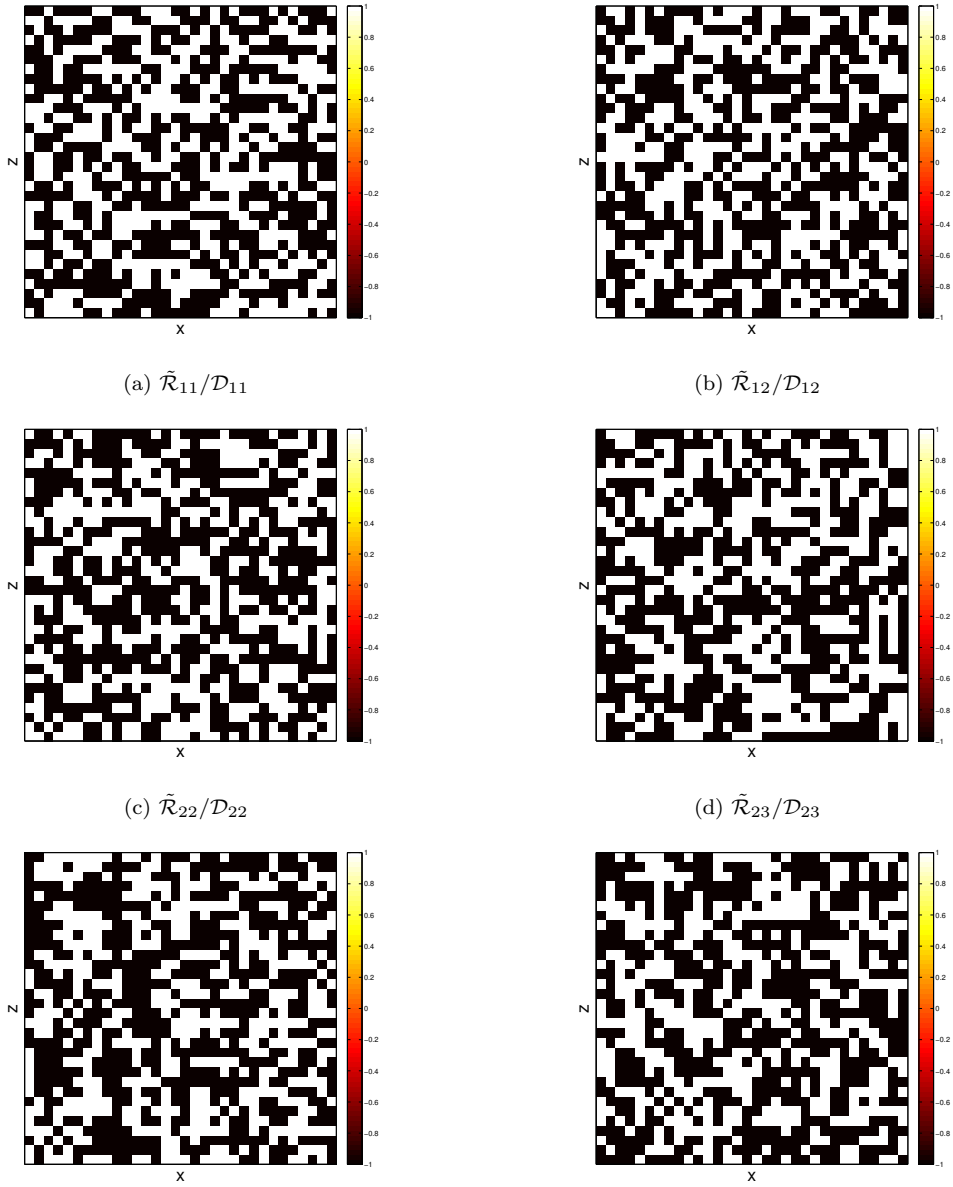

(a) $\tilde{\mathcal{R}}_{11}/\mathcal{D}_{11}$

(b) $\tilde{\mathcal{R}}_{12}/\mathcal{D}_{12}$

(c) $\tilde{\mathcal{R}}_{22}/\mathcal{D}_{22}$

(d) $\tilde{\mathcal{R}}_{23}/\mathcal{D}_{23}$

(e) $\tilde{\mathcal{R}}_{33}/\mathcal{D}_{33}$

(f) $\tilde{\mathcal{R}}_{31}/\mathcal{D}_{31}$

Figure 2.2: Spatial distributions of snapshots of the sign of $\tilde{\mathcal{R}}_{11}\mathcal{D}_{11}$ at time $t = 2$ on the central layer of the channel $y = 0$ for each entry of $\tilde{\mathcal{R}}/\mathcal{D}$

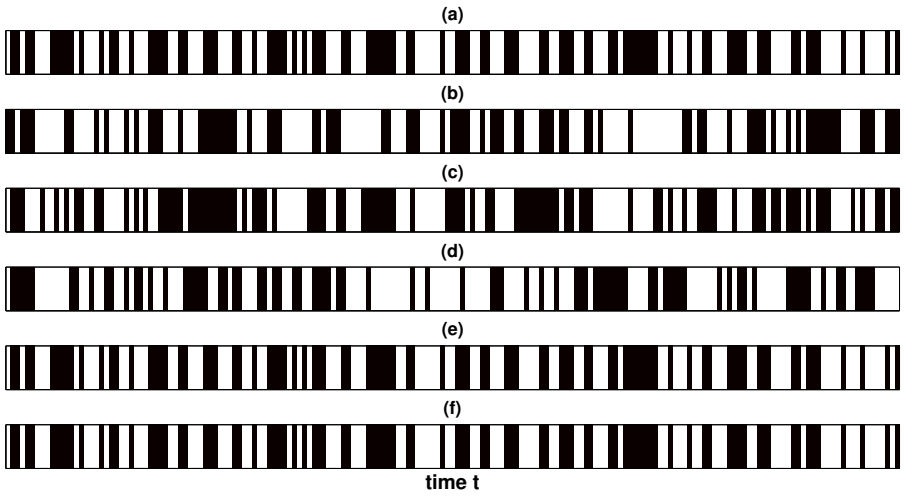

Figure 2.3: Time series of the sign of elements of $\tilde{\mathcal{R}}\mathcal{D}$ at location (3.81, 0, 1.90) over time interval $[0.2, 2]$. Black bars denote -1 and white bars denote $+1$. (a) $\tilde{\mathcal{R}}_{11}/\mathcal{D}_{11}$; (b) $\tilde{\mathcal{R}}_{22}/\mathcal{D}_{22}$; (c) $\tilde{\mathcal{R}}_{33}/\mathcal{D}_{33}$; (d) $\tilde{\mathcal{R}}_{12}/\mathcal{D}_{12}$; (e) $\tilde{\mathcal{R}}_{23}/\mathcal{D}_{23}$; (f) $\tilde{\mathcal{R}}_{31}/\mathcal{D}_{31}$

Further, in three-dimensional space, the three invariants $I_i\,(i = 1, 2, 3)$ of a matrix M can be expressed by the three eigenvalues $\lambda_i\,(i = 1, 2, 3)$ as follows:

$$\begin{aligned} I_1 &= \mathrm{tr}(M) = \sum_{i=1,2,3} \lambda_i, \\ I_2 &= \frac{1}{2}\left((\mathrm{tr}(M))^2 - \mathrm{tr}(MM)\right) = \lambda_1\lambda_2 + \lambda_2\lambda_3 + \lambda_3\lambda_1, \\ I_3 &= \det(M) = \prod_{i=1,2,3} \lambda_i. \end{aligned}$$

Given the relations in (2.2.7), we can express the invariants of $\mathcal{B}$ by those of $\mathcal{D}$. Now, the coefficient β can be formulated approximately as a function of the three principal invariants of $\mathcal{D}$. For various flows, we can specify the characteristic structure of the rate-of-strain tensor $\mathcal{D}$ so that an explicit form for the coefficient β may be obtained. To validate our mathematical derivation of turbulent models, we first take homogeneous turbulent flow as an example for its simple geometry and physics. Later on, we will work on a more realistic channel flow, chosen because of its relevance to a large variety of engineering applications and its ability to provide direct insight into fundamental turbulence phenomena. We will investigate these two examples further in Section 2.3.

2.3 Examples: Incompressible homogeneous turbulence and turbulent channel flow

Based on the mathematical analysis in the previous sections, we are now ready to give two examples to illustrate the procedure of deriving turbulent models for incompressible turbulent flows.

2.3.1 Homogeneous incompressible turbulence

For the homogeneous turbulence, the flow is statistically invariant under translations and/or rotations of the reference frame. Therefore, all entries in the strain tensor must be of the same order. Then, the full strain-rate tensor $\mathcal{D}$ has to be considered:

$$\mathcal{D} = \begin{bmatrix} u_x & \frac{1}{2}(u_y + v_x) & \frac{1}{2}(u_z + w_x) \\ \frac{1}{2}(u_y + v_x) & v_y & \frac{1}{2}(v_z + w_y) \\ \frac{1}{2}(u_z + w_x) & \frac{1}{2}(v_z + w_y) & w_z \end{bmatrix}. \tag{2.3.1}$$

The first principal invariant of $\mathcal{D}$ is zero due to the incompressibility of turbulent flows, i.e. ,

$$I_1 = \mathrm{tr}(\mathcal{D}) = \nabla_{\boldsymbol{x}} \cdot \boldsymbol{u} = 0.$$

The other two invariants can be calculated as follows:

$$I_2 = \frac{1}{2}\left((\mathrm{tr}(\mathcal{D}))^2 - \mathrm{tr}(\mathcal{D}\mathcal{D})\right) = -\frac{1}{2}\left\|\mathcal{D}\right\|_F^2, \quad I_3 = \det(\mathcal{D}), \tag{2.3.2}$$

where $\|\cdot\|_F$ is the Frobenius norm, i.e. , $\|\mathcal{D}\|_F = \sqrt{\sum_i \sum_j |\mathcal{D}_{ij}|^2}$. For the homogeneous flows, statistically, the averaged velocity derivatives should be the same. Therefore, the averaged strain-rate tensor $\mathcal{D}$ becomes a multiple of a matrix of ones. Thus the determinant of $\mathcal{D}$, i.e. , I_3, vanishes in the statistical sense (Betchov, 1956). However, for each snapshot of homogeneous turbulence, the determinant of $\mathcal{D}$ is not expected to vanish in general. Therefore, mathematically, the choice of β cannot be determined explicitly.

By Remark 2.2.7, the coefficient β can be written in the following form

$$\beta = \frac{\gamma}{\Delta t}, \tag{2.3.3}$$

where γ is a function of the principal invariants of $\mathcal{D}$.

Then, by dimensional analysis, we find that γ has the dimension of $\Delta^2(-2I_2)^{1/2} = \Delta^2 \|\mathcal{D}\|_F$ or $\Delta^2 I_3^{1/3} = \Delta^2(\det(\mathcal{D})^{1/3})$, where Δ is a typical length of the large-scale solution. In principle, γ can be a combination of I_2 and I_3:

$$\gamma = C\Delta^2 \|\mathcal{D}\|_F^{\varrho} \det(\mathcal{D})^{(1-\varrho)/3},$$

where C is a non-dimensional constant.

Assumption 2.3.1. *We assume that γ depends only on $\|\mathcal{D}\|_F$ or $\det(\mathcal{D})$. Then, β is a linear function of $\|\mathcal{D}\|_F$ or $(\det(\mathcal{D}))^{1/3}$, i.e. ,*

$$\beta(I_1, I_2, I_3) = C_1^2 \Delta^2 \|\mathcal{D}\|_F ,$$

or

$$\beta(I_1, I_2, I_3) = C_2 \Delta^2 (\det(\mathcal{D}))^{1/3},$$

where C_1 and C_2 are universal non-dimensional constants because of homogeneity.

Using the minimization technique to be described in Section 2.3.2, we can compute the pointwise distribution of C_1, as shown in Figure 2.4, and C_2, as shown in Figure 2.5. When choosing the norm $\|\mathcal{D}\|_F$ for the coefficient β, the distribution of C_1 is noticeably uniform. On the other hand, we see clearly the inhomogeneity of C_2 on both layers in wall-normal direction. Furthermore, the plots of r.m.s. C_1 and C_2 fluctuations in Figure 2.6 indicate the fact quantitatively that C_1 displays more uniform pattern than C_2 does. Although we cannot justify the use of the Frobenius norm mathematically, this is definitely an indicator of preference of the Frobenius norm over the determinant from this numerical study.

Based on the analysis and numerical verification above, we make the following assumption:

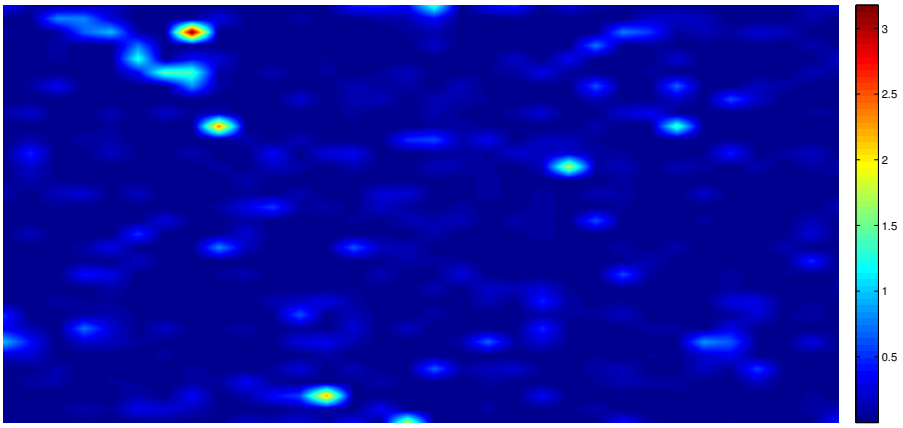

(a)

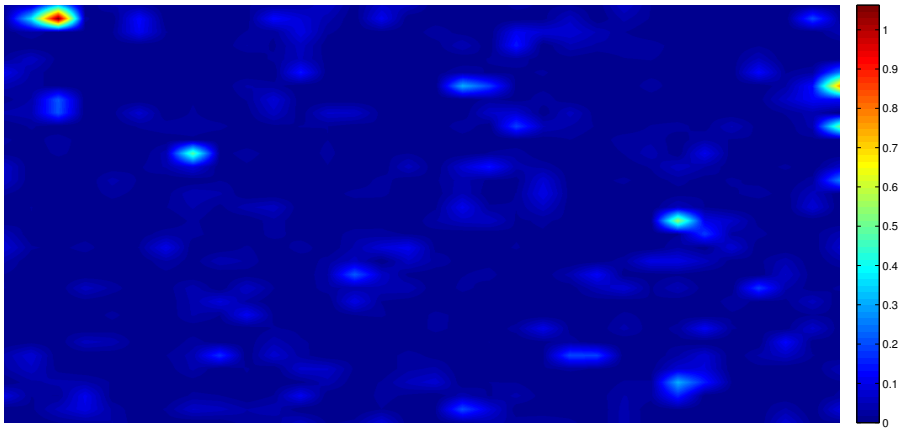

(b)

Figure 2.4: Contour plots of C_1 in x-z plane using $\|\mathcal{D}\|_F$ at (a) $y = 0$ and (b) $y = 0.92388$

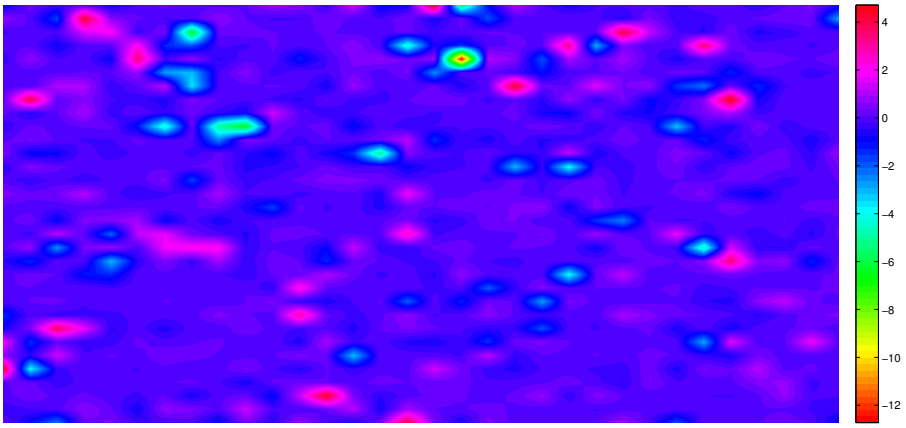

(a)

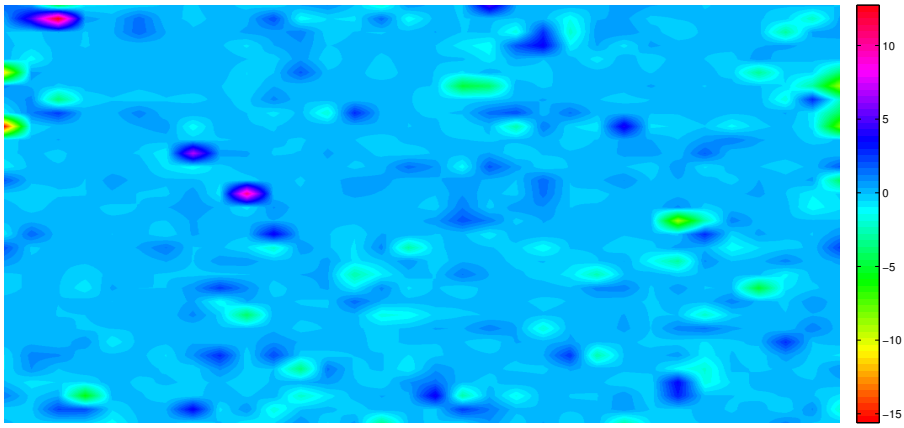

(b)

Figure 2.5: Contour plots of C_2 in x-z plane using $\det(\mathcal{D})$ at (a) $y = 0$ and (b) $y = 0.92388$

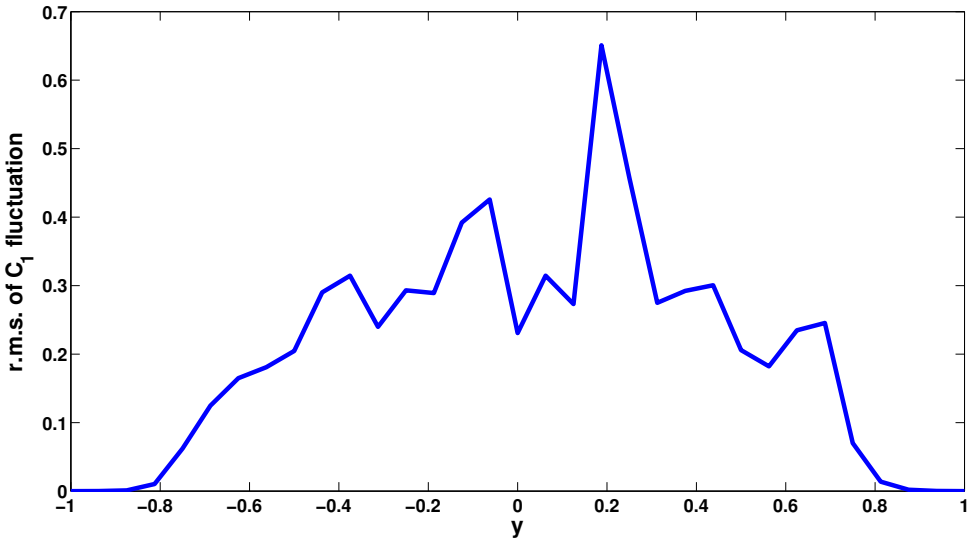

(a)

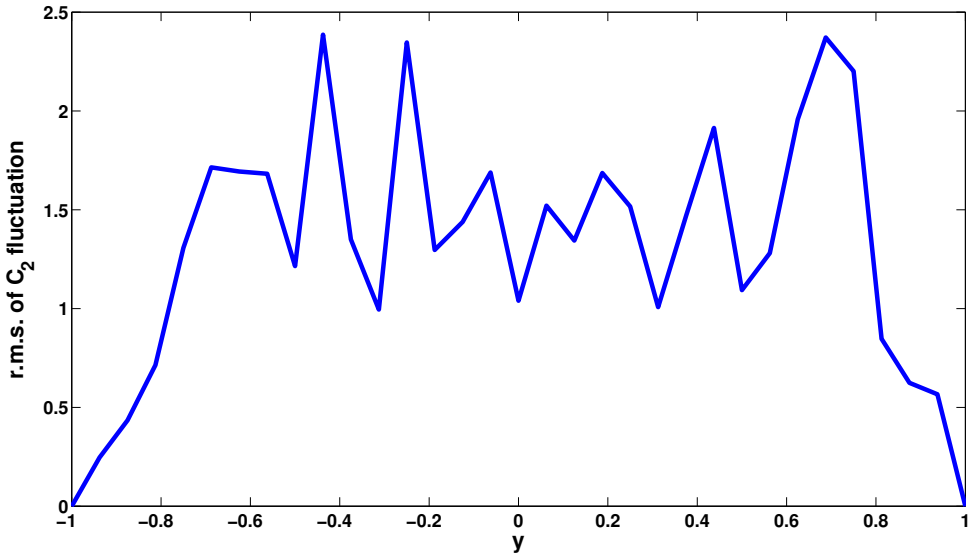

(b)

Figure 2.6: Profiles of r.m.s. $C_{1,2}$ fluctuations. (a): C_1 for Frobenius norm; (b): C_2 for determinant

Assumption 2.3.2. *we assume that β is a linear function of $\|\mathcal{D}\|_F$, i.e.*

$$\gamma(I_1, I_2, I_3) = C_s^2 \Delta^2 \|\mathcal{D}\|_F ,$$

where C_s is a universal constant because of homogeneity.

Theorem 2.3.3. *The following Smagorinsky model for the homogeneous turbulence can be recovered by multiscale analysis:*

$$\mathcal{R} = -(C_s \Delta)^2 \|\mathcal{D}\|_F \mathcal{D}. \tag{2.3.4}$$

Proof. Putting Eqs. (2.2.2) and (2.3.3) and Assumption 2.3.2 together, it is clear that the linear relation (2.3.4) holds, up to the second order of time step Δt. □

Remark 2.3.4. *The constant $C_s = 0.18$, as can be estimated by using the $k^{-5/3}$ Kolmogorov cascade to make the ensemble-averaged subgrid kinetic energy dissipation identical to the kinetic energy (Lilly, 1987).*

Remark 2.3.5. *In Eq.* (2.1.11a)*, the Reynolds stress is given as $\mathcal{R} = \langle [\boldsymbol{w} \otimes \boldsymbol{w}]^*_{\Delta\tau} \rangle$. While in the multiscale expansion* (2.1.4)*, the large- and small-scale velocities have the same order, i.e.*

$$\boldsymbol{u} \sim \boldsymbol{w}.$$

Hence, the order of the magnitude of $\mathcal{R}$ is

$$\mathcal{O}(||\mathcal{R}|\,|) = \mathcal{O}(||\boldsymbol{u}||^2),$$

where $||\cdot||$ is the norm w.r.t. matrices or vectors.

While, the magnitude of the right hand side in Eq. (2.3.4) *is*

$$\mathcal{O}(\Delta^2)\mathcal{O}\left(\frac{||\boldsymbol{u}||}{\Delta}\right)\mathcal{O}\left(\frac{||\boldsymbol{u}||}{\Delta}\right) = \mathcal{O}(||\boldsymbol{u}||^2).$$

Therefore, the Smagorinsky model obtained based on multiscale analysis is consistent in the sense of magnitude scaling of flow variables.

Table 2.1: Quantitative order of the velocity derivatives

$\partial u/\partial x$	$\partial u/\partial y$	$\partial u/\partial z$	$\partial v/\partial x$	$\partial v/\partial y$	$\partial v/\partial z$	$\partial w/\partial x$	$\partial w/\partial y$	$\partial w/\partial z$
$\sim 10^{-2}$	$\sim 10^{2}$	$\sim 10^{-2}$	$\sim 10^{-4}$	$\sim 10^{-1}$	$\sim 10^{-4}$	$\sim 10^{-2}$	$\sim 10^{2}$	$\sim 10^{-1}$

2.3.2 Turbulent channel flow

The modeling derivation procedure of the homogeneous turbulence also applies to the turbulent channel flow. The following modified Smagorinsky model can be recovered by adding the van Driest damping function

$$\mathcal{R} = -(C_s\Delta(1-\exp(-y^+/A)))^2 \left\|\mathcal{D}\right\|_F \mathcal{D},$$

where y^+ is the non-dimensional distance from the wall and $A = 25$ is the van Driest constant (van Driest, 1956). However, we can simplify the Smagorinsky model by taking advantage of the special structure of the strain rate $\mathcal{D}$ for the turbulent channel flow. Specifically, from an asymptotic boundary layer analysis, we find the order of the velocity derivatives are as follows:

$$\frac{\partial u}{\partial y}, \frac{\partial w}{\partial y} \gg \frac{\partial u}{\partial x}, \frac{\partial u}{\partial z}, \frac{\partial v}{\partial y}, \frac{\partial w}{\partial x}, \frac{\partial w}{\partial z} \gg \frac{\partial v}{\partial x}, \frac{\partial v}{\partial z}.$$

The scaling analysis of the velocity derivatives near the wall is consistent with the numerical results of DNS (see Table 2.1). Given the orders of the velocity derivatives, we neglect the small quantities in the entries of $\mathcal{D}$. Thus, $\mathcal{D}$ can be approximated as

$$\mathcal{D} \sim \begin{bmatrix} 0 & u_y/2 & 0 \\ u_y/2 & 0 & w_y/2 \\ 0 & w_y/2 & 0 \end{bmatrix}. \tag{2.3.5}$$

The eigenvalues of the above approximate $\mathcal{D}$ are $\lambda_1 = 0$, $\lambda_{2,3} = \pm\frac{1}{2}\sqrt{u_y^2 + w_y^2}$. Thus, it follows that the three principal invariants are $I_1 = I_3 = 0$, and $I_2 = -(u_y^2 + w_y^2)/4$. Now, the coefficients α and β are functionals of I_2 or $u_y^2 + w_y^2$ only [1]. Based on the same arguments as those for the homogeneous turbulence, we propose the following

[1] Notice that in this approximation, we don't have the dilemma of choices between invariants I_2 and I_3, as in the case of homogeneous turbulence. This is another indication of preference for the Frobenius norm over the determinant.

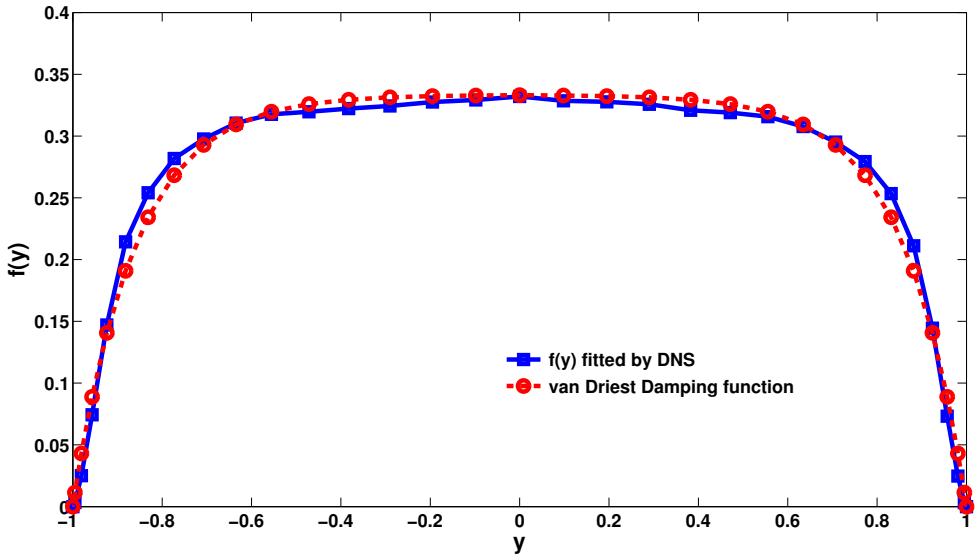

Figure 2.7: Profile of $f(y)$ fitted by DNS vs. the van Driest function

form for β:

$$\beta = \frac{\Delta^2}{\Delta t} f(y)(u_y^2 + w_y^2)^{1/2},$$

where $f(y)$ is a function of y or y^+ due to the inhomogeneity in y direction. Using DNS data, Figure 2.7 shows that $f(y^+)$ has the shape close to the van Driest damping function

$$f(y^+) = C_m^2((1 - \exp(-y^+/A)))^2,$$

where C_m is the universal constant, y^+ is the non-dimensional distance from the wall, and $A = 25$ is the van Driest constant (van Driest, 1956). The distance from the wall measured in wall units is important in the turbulent channel flow and defined as

$$y^+ = \frac{u_\tau(\delta - |y|)}{\nu}, \tag{2.3.6}$$

where δ is the channel half-width, u_τ is the wall shear velocity, and ν is the viscosity.

From the analysis and numerical verification, we have the following theorem:

Theorem 2.3.6. *For a channel flow, the following simplified model can be obtained*

by multiscale analysis:

$$\mathcal{R} = -(C_m \Delta(1 - \exp(-y^+/A)))^2 (u_y^2 + w_y^2)^{1/2} \mathcal{D}. \tag{2.3.7}$$

Remark 2.3.7. *In the simplified model* (2.3.7)*, Reynolds stress reduces to* 0 *naturally as the boundary is approached due to the van Driest damping function (see van Driest, 1956; Pope, 2000; Berselli* et al.*, 2006). This property ensures that the non-slip boundary condition at the walls is preserved.*

Remark 2.3.8. *In the process of obtaining the simplified model* (2.3.7)*, we have extended the asymptotic analysis, which is valid within the boundary layer, to the entire domain. This introduces additional modeling error, which will be illustrated in the following numerical examples.*

The constant C_m can be determined by locally minimizing the Reynolds stress error term

$$\min_{C_m} \left\| \mathcal{R} + \left(C_m \Delta(1 - \exp(-y^+/A))(u_y^2 + w_y^2)^{1/4} \right)^2 \mathcal{D} \right\|_F .$$

This gives us

$$C_m = \frac{\sqrt{-\mathcal{R} : \mathcal{D}}}{\Delta(1 - \exp(-y^+/A))(u_y^2 + w_y^2)^{1/4} \left\| \mathcal{D} \right\|_F}, \tag{2.3.8}$$

where $\mathcal{R} : \mathcal{D} = \sum_{i,j} \mathcal{R}_{ij} \mathcal{D}_{ij}$. We perform *a priori* computation to determine $\mathcal{R}$ in equation (2.3.8) using the multiscale formulation elaborated in the following algorithm.

Algorithm 2.3.9 (Determining the constant C_m)**.**

(i) Run a DNS simulation of (2.1.1) *to get the full velocity field* $\boldsymbol{u}^\epsilon(\boldsymbol{x}_i, t_n)$ *at each time step.*

(ii) Perform a reparameterization procedure, which is based on the Fourier expansion and explained in detail in Appendix B for the channel flow, to obtain $\boldsymbol{u}(\boldsymbol{x}_i, t_n)$ *and* $\boldsymbol{w}(\boldsymbol{x}_i, t_n, \boldsymbol{x}_i/\epsilon, t_n/\epsilon)$*.*

(iii) The Reynolds stress is given by

$$\mathcal{R}(\boldsymbol{x}, t) = \langle \boldsymbol{w} \otimes \boldsymbol{w} \rangle - \frac{1}{3} \mathrm{tr}(\langle \boldsymbol{w} \otimes \boldsymbol{w} \rangle) \mathcal{I}. \tag{2.3.9}$$

2.3.3 Verification of Algorithm 2.3.9 for the determination of constant C_m

In order to validate Algorithm 2.3.9, we run a test on a classical eddy viscosity model–the Smagorinsky model with van Driest damping. The Smagorinsky model (Smagorinsky, 1963) can be derived from the $k^{-5/3}$ spectra theorem. In a channel flow, the layer near the wall introduces a large amount of dissipation. The extra dissipation prevents the formation of eddies, thus eliminating turbulence from the beginning. Therefore, van Driest damping is introduced to reduce the Smagorinsky constant C_S to 0 when approaching the walls (for more discussions, see Pope, 2000; Sagaut, 2001). The Smagorinsky model with van Driest damping for Reynolds stress reads as

$$\mathcal{R}(\boldsymbol{x},t) = -(C_s\Delta(1-\exp(-y^+/A)))^2 \left\|\mathcal{D}\right\|_F \mathcal{D}, \tag{2.3.10}$$

where C_s is the Smagorinsky constant, $\Delta = \sqrt[3]{\Delta_x\Delta_y(y)\Delta_z}$ is the filter width, and y^+ is the non-dimensional distance from the wall.

The constant C_s can be estimated by using the $k^{-5/3}$ Kolmogorov cascade to make the ensemble-averaged subgrid kinetic energy dissipation identical to ε, which is the kinetic energy (see the review by Lilly, 1987). An approximate value for the constant is then

$$C_s \approx \frac{1}{\pi}\left(\frac{3C_K}{2}\right)^{-3/4}. \tag{2.3.11}$$

For a Kolmogorov constant C_K of 1.4, which is obtained by measurements in the atmosphere (Champagne *et al.*, 1977), this yields $C_s \approx 0.18$.

On the other hand, using the technique of an iterative homogenization of large- and small-scale solutions dynamically and locally minimizing the Reynolds stress error, the Smagorinsky constant C_s can be determined as follows:

$$C_s = \frac{\sqrt{-\mathcal{R}_d : \mathcal{D}}}{\Delta(1-\exp(-y^+/A))\left\|\mathcal{D}\right\|_F \sqrt{\left\|\mathcal{D}\right\|_F}}. \tag{2.3.12}$$

In Figure 2.8, we plot the evolution of the Smagorinsky constant C_s. C_s oscillates slightly around the value of 0.18, showing that Algorithm 2.3.9 determines the Smagorinsky constant accurately. Figure 2.9 indicates that the constant C_m is around

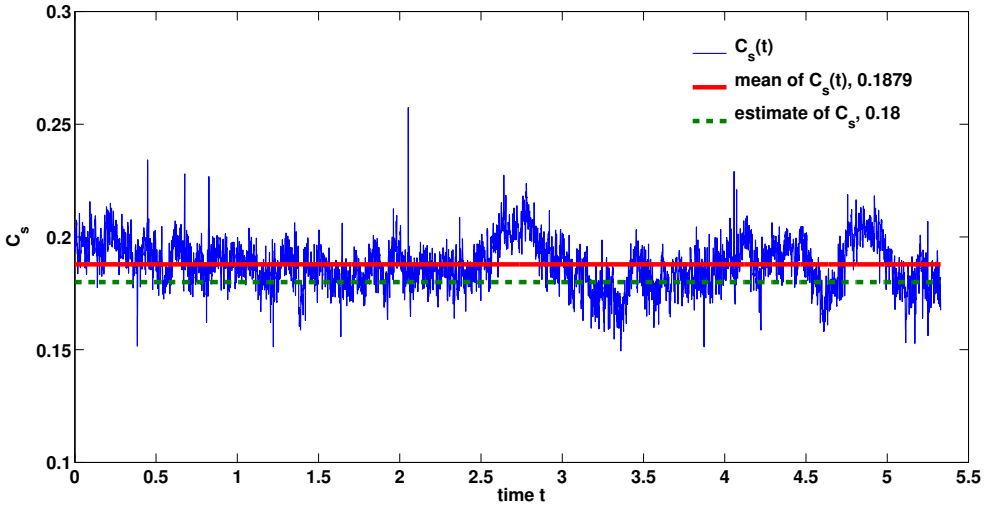

Figure 2.8: Temporal evolution of the constant C_s in the Smagorinsky model with van Driest damping function. The dashed line denotes the value of 0.18, which can be estimated by using the $k^{-5/3}$ Kolmogorov cascade to make the ensemble-averaged subgrid kinetic energy dissipation identical to the kinetic energy (Lilly, 1987).

0.2074. This is the value we will take in the following numerical simulation with the simplified Smagorinsky model for turbulent channel flow.

2.4 Nonlinear LES modeling

In Section 2.2, we use an Euler approximation of the inverse flow map function $\boldsymbol{\theta}$ to establish a linear constitutive relation (2.2.4). Essentially, the multiscale model we have done so far is a first order approximation process that allows us to recover the Smagorinsky model for homogeneous turbulence and to introduce a simplified Smagorinsky model for channel flow. In the following, we push to a second order approximation in order to obtain a nonlinear constitutive relation.

In order to obtain a nonlinear relation between the Reynolds stress and the strain rate, instead of using an Euler approximation, we must employ a second order scheme. Here, the second order Runge-Kutta, which is essentially a two-step marching of the first order Euler scheme, is adopted. The first step marching gives us $\boldsymbol{\theta}$ at $t + \Delta t/2$:

$$\boldsymbol{\theta}(t + \Delta t/2, \boldsymbol{x}) \;=\; \boldsymbol{x} - \frac{1}{2}\boldsymbol{u}(t, \boldsymbol{x})\Delta t + \mathcal{O}(\Delta t^2), \tag{2.4.1}$$

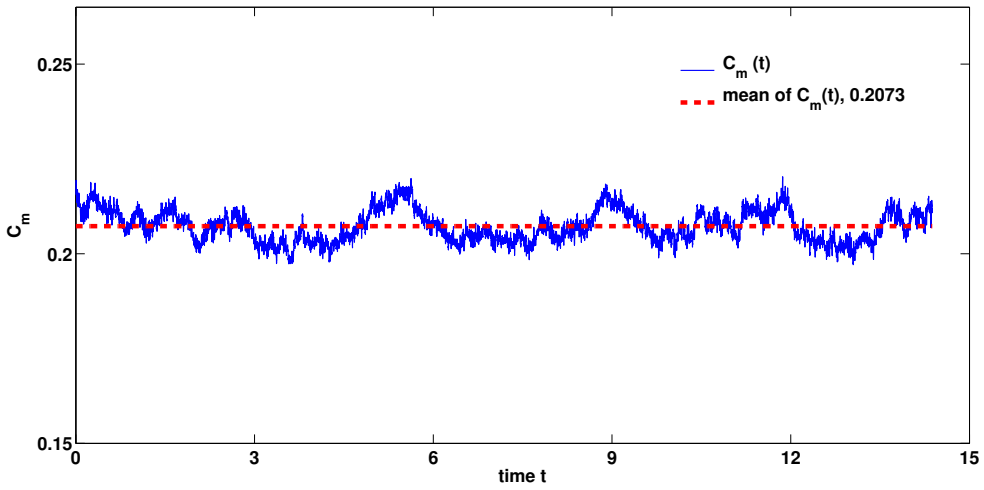

Figure 2.9: Temporal evolution of the constant C_m in the simplified Smagorinsky model obtained by Algorithm 2.3.9. The dashed line denotes the value of 0.2073, which is a universal constant for the turbulent channel flow.

then the second step of marching gives

$$\begin{aligned}\boldsymbol{\theta}(t+\Delta t,\boldsymbol{x}) &= \boldsymbol{x}-\Delta t(\boldsymbol{u}(t+\Delta t/2,\boldsymbol{x})\cdot\nabla)\boldsymbol{\theta}(t+\Delta t/2,\boldsymbol{x})\\ &= \boldsymbol{x}-\Delta t\boldsymbol{u}(t,\boldsymbol{x})+\frac{1}{2}\Delta t^2(\boldsymbol{u}(t,\boldsymbol{x})\cdot\nabla)\boldsymbol{u}(t,\boldsymbol{x})\\ &\quad -\frac{1}{2}\Delta t^2\boldsymbol{u}_t(t,\boldsymbol{x})+\mathcal{O}(\Delta t^3). \end{aligned} \tag{2.4.2}$$

Recall that $\boldsymbol{u}$ satisfies equation (2.1.11). Hence,

$$\boldsymbol{u}_t=-(\boldsymbol{u}\cdot\nabla)\boldsymbol{u}-\nabla p-\nabla\cdot\mathcal{R}-\nu\nabla^2\boldsymbol{u}. \tag{2.4.3}$$

In the above equation, we assume that the viscosity ν is small and the effect of the term $\nu\nabla^2\boldsymbol{u}$ can be neglected [2].

Accordingly, we have the following second order approximation to the inverse flow map $\boldsymbol{\theta}$:

$$\boldsymbol{\theta}(t,\boldsymbol{x})=\boldsymbol{x}-\boldsymbol{u}\Delta t+\Delta t^2(\boldsymbol{u}\cdot\nabla)\boldsymbol{u}+\frac{1}{2}\Delta t^2(\nabla p+\nabla\cdot\mathcal{R})+\mathcal{O}(\Delta t^3). \tag{2.4.4}$$

[2]To avoid confusion notations, Δ is reserved for the filter width in the LES model and $\nabla^2=\nabla\cdot\nabla$ denotes the Laplacian operator.

It follows that

$$\begin{aligned}
\mathcal{A} &= D_{\boldsymbol{x}}\boldsymbol{\theta} = \mathcal{I} - \Delta t\nabla\boldsymbol{u} + \Delta t^2\nabla\left[(\boldsymbol{u}\cdot\nabla)\boldsymbol{u}\right] \\
&\quad + \frac{1}{2}\Delta t^2\nabla(\nabla p + \nabla\cdot\mathcal{R}) + \mathcal{O}(\Delta t^3), \qquad (2.4.5)\\
\mathcal{A}^{-1} &= \mathcal{I} + \Delta t\nabla\boldsymbol{u} - \Delta t^2\nabla\left[(\boldsymbol{u}\cdot\nabla)\boldsymbol{u}\right] + \Delta t^2\nabla\boldsymbol{u}\nabla\boldsymbol{u} \\
&\quad - \frac{1}{2}\Delta t^2\nabla(\nabla p + \nabla\cdot\mathcal{R}) + \mathcal{O}(\Delta t^3), \qquad (2.4.6)\\
\mathcal{B} &= \mathcal{A}\mathcal{A}^T = \mathcal{I} - 2\Delta t\mathcal{D} + \Delta t^2(\mathcal{E} + \mathcal{E}') + \mathcal{O}(\Delta t^3), \qquad (2.4.7)
\end{aligned}$$

where $\mathcal{E}$ and $\mathcal{E}'$ are defined as

$$\begin{aligned}
\mathcal{E} &= \nabla\boldsymbol{u}\nabla\boldsymbol{u}^T + \nabla\left[(\boldsymbol{u}\cdot\nabla)\boldsymbol{u}\right] + \nabla^T\left[(\boldsymbol{u}\cdot\nabla)\boldsymbol{u}\right] \\
&= \nabla\boldsymbol{u}\nabla\boldsymbol{u}^T + \nabla\boldsymbol{u}\nabla\boldsymbol{u} + \nabla\boldsymbol{u}^T\nabla\boldsymbol{u}^T + 2(\boldsymbol{u}\cdot\nabla)\mathcal{D}, \qquad (2.4.8)\\
\mathcal{E}' &= \frac{1}{2}\left[\nabla(\nabla p + \nabla\cdot\mathcal{R}) + \nabla^T(\nabla p + \nabla\cdot\mathcal{R})\right]. \qquad (2.4.9)
\end{aligned}$$

Remark 2.4.1. *In the formulations* (2.4.5)-(2.4.7)*, the second order nonlinear terms come from the convection term in the Navier-Stokes equations.*

Remark 2.4.2. *Note that $\mathcal{E}$ and $\mathcal{E}'$ are symmetric. This does not conflict with the fact that the Reynolds stress $\mathcal{R}$ is symmetric.*

Once these fundamental quantities are computed, the tensor product of $\langle\tilde{\boldsymbol{w}}\otimes\tilde{\boldsymbol{w}}\rangle$ can be calculated as follows:

$$\begin{aligned}
\langle\tilde{\boldsymbol{w}}\otimes\tilde{\boldsymbol{w}}\rangle &= a_0\mathcal{I} + a_1\mathcal{B} + a_2\mathcal{B}^2 \\
&= a_0\mathcal{I} + a_1\left(\mathcal{I} - 2\Delta t\mathcal{D} + \Delta t^2(\mathcal{E}+\mathcal{E}') + \mathcal{O}(\Delta t^3)\right) \\
&\quad + a_2\left(\mathcal{I} - 2\Delta t\mathcal{D} + \Delta t^2(\mathcal{E}+\mathcal{E}') + \mathcal{O}(\Delta t^3)\right)^2 \\
&= \alpha\mathcal{I} - \tilde{\beta}\Delta t\mathcal{D} + \Delta t^2(\mathcal{F}+\mathcal{F}') + \mathcal{O}(\Delta t^3),
\end{aligned}$$

where the coefficients $\alpha = a_0 + a_1 + a_2$ and $\tilde{\beta} = 2(a_1 + 2a_2)$ and the second order term

$\mathcal{F}$ is defined as

$$\begin{aligned}
\mathcal{F} &= (a_1 + 2a_2)\,\mathcal{E} + 4a_2\mathcal{D}\mathcal{D}^T \\
&= (a_1 + 3a_2)\,\nabla\boldsymbol{u}\nabla\boldsymbol{u} + (a_1 + 3a_2)\nabla\boldsymbol{u}\nabla\boldsymbol{u}^T + (a_1 + 3a_2)\,\nabla\boldsymbol{u}^T\nabla\boldsymbol{u}^T \\
&\quad + a_2\nabla\boldsymbol{u}^T\nabla\boldsymbol{u} + 2(a_1 + 2a_2)(\boldsymbol{u}\cdot\nabla)\mathcal{D}, \qquad (2.4.10) \\
\mathcal{F}' &= (a_1 + 2a_2)\mathcal{E}'. \qquad (2.4.11)
\end{aligned}$$

Finally, returning to the description using $\boldsymbol{w}$, the Reynolds stress can be expressed up to second order in time:

$$\begin{aligned}
\mathcal{R} &= \langle \boldsymbol{w} \otimes \boldsymbol{w} \rangle \\
&= \mathcal{A}^{-1}\langle \tilde{\boldsymbol{w}} \otimes \tilde{\boldsymbol{w}} \rangle (\mathcal{A}^{-1})^T \\
&= \alpha\mathcal{I} - \beta\Delta t\mathcal{D} + \Delta t^2(\mathcal{G} + \mathcal{G}') + \mathcal{O}(\Delta t^3), \qquad (2.4.12)
\end{aligned}$$

and the second order term $\mathcal{G}$ and $\mathcal{G}'$ are defined as follows:

$$\begin{aligned}
\mathcal{G} &= -\alpha\left(\nabla\left[(\boldsymbol{u}\cdot\nabla)\boldsymbol{u}\right] + \nabla^T\left[(\boldsymbol{u}\cdot\nabla)\boldsymbol{u}\right]\right) \\
&\quad -\beta\left(\nabla\boldsymbol{u}\mathcal{D} + (\nabla\boldsymbol{u}\mathcal{D})^T\right) + \mathcal{F} + \alpha\nabla\boldsymbol{u}\nabla\boldsymbol{u}^T \\
&= \zeta\nabla\boldsymbol{u}\nabla\boldsymbol{u}^T + \eta\nabla\boldsymbol{u}^T\nabla\boldsymbol{u} + \xi(\nabla\boldsymbol{u}\nabla\boldsymbol{u} + \nabla\boldsymbol{u}^T\nabla\boldsymbol{u}^T) + \chi(\boldsymbol{u}\cdot\nabla)\mathcal{D}, \qquad (2.4.13) \\
\mathcal{G}' &= \kappa\left[\nabla(\nabla p + \nabla\cdot\mathcal{R}) + \nabla^T(\nabla p + \nabla\cdot\mathcal{R})\right], \qquad (2.4.14)
\end{aligned}$$

where the coefficients are

$$\begin{aligned}
\alpha &= a_0 + a_1 + a_2, \\
\beta &= -2(a_0 - a_2), \\
\zeta &= -(a_0 + a_1), \\
\xi &= a_0, \\
\eta &= a_2, \\
\chi &= -2(a_0 + a_2), \\
\kappa &= \frac{1}{2}(a_1 + a_2 - a_0).
\end{aligned}$$

The Reynolds stress appears implicitly in Equation (2.4.12). By iterating in $\mathcal{R}$ and keeping the terms up to second order in time, we have

$$\begin{aligned}\mathcal{R} &= \alpha\mathcal{I} - \beta\Delta t\mathcal{D} + \Delta t^2\mathcal{G} + 2\kappa\Delta t^2\left(\nabla(\nabla p)\right) \\ &\quad +2\kappa\Delta t^2\nabla(\nabla\cdot(\alpha\mathcal{I})) + \mathcal{O}(\Delta t^3), \end{aligned} \tag{2.4.15}$$

since Hessian matrix $\nabla(\nabla p)$ is symmetric.

We have the following observations:

(i) $\nabla\cdot(\alpha\mathcal{I}) = \nabla(\alpha)$;

(ii) $\nabla\cdot(\nabla(\nabla p)) = \nabla(\nabla^2 p)$;

(iii) $\nabla\cdot(\nabla(\nabla\cdot(\alpha\mathcal{I}))) = \nabla(\nabla^2\alpha)$.

Therefore, the effect of the terms $\alpha\mathcal{I}$, $2\kappa\Delta t^2\left(\nabla(\nabla p)\right)$ and $2\kappa\Delta t^2\nabla(\nabla\cdot(\alpha\mathcal{I}))$ in (2.4.15) can be absorbed in pressure with a modified pressure

$$p' = p + \alpha + 2\kappa\Delta t^2(\nabla^2 p + \nabla^2\alpha).$$

Hence, we can drop the terms $\alpha\mathcal{I}$, $2\kappa\Delta t^2\left(\nabla(\nabla p)\right)$ and $2\kappa\Delta t^2\nabla(\nabla\cdot(\alpha\mathcal{I}))$ in (2.4.15).

Therefore, the nonlinear relation is given by

$$\mathcal{R} = -\beta\Delta t\mathcal{D} + \Delta t^2\mathcal{G} + \mathcal{O}(\Delta t^3). \tag{2.4.16}$$

The above nonlinear model (2.4.16) can be rewritten as

$$\begin{aligned}\mathcal{R} &= -\beta\Delta t\mathcal{D} + D_1\Delta^2\mathcal{D}^2 + D_2\Delta^2(\mathcal{D}\Omega - \Omega\mathcal{D}) \\ &\quad + D_3\Delta^2\Omega^2 + D_4\Delta^2(\boldsymbol{u}\cdot\nabla)\mathcal{D}, \end{aligned} \tag{2.4.17}$$

where $D_1 = (\zeta+\eta+2\xi)\Delta t^2/\Delta^2$, $D_2 = (\eta-\zeta)\Delta t^2/\Delta^2$, $D_3 = (2\xi-\zeta-\eta)\Delta t^2/\Delta^2$, and $D_4 = \chi\Delta t^2/\Delta^2$.

From Lemma 2.2.6, we know that

$$\beta \sim \frac{1}{\Delta t}, \quad \text{or} \quad \beta\Delta t \sim 1.$$

If we take the limit $\Delta t \to 0$, we assume $\mathcal{G}$ does not vanish. Therefore, we make the following assumption:

Assumption 2.4.3. *We assume the following order of the coefficient set*

$$(\zeta, \eta, \xi, \chi) \sim \frac{1}{\Delta t^2},$$

or

$$(D_2, D_3, D_4) \sim \frac{1}{\Delta^2}.$$

Lemma 2.4.4. *The coefficient D_1 in Eq. (2.4.17) is the order of $1/\Delta^2$, i.e.*

$$D_1 \sim \frac{1}{\Delta^2}. \tag{2.4.18}$$

Proof. The proof is similar to the proof of Lemma 2.2.6. Denote λ_1 and μ_1 are the eigen-values of $\mathcal{D}$ and $\mathcal{R}$, respectively. Let ψ_1 be the orthonormal eigen-vector shared by $\mathcal{D}$ and $\mathcal{R}$. By Assumption 2.4.3, the entries in $D_2\Delta^2(\mathcal{D}\Omega - \Omega\mathcal{D})$, $D_3\Delta^2\Omega^2$ and $D_4\Delta^2(\boldsymbol{u}\cdot\nabla)\mathcal{D}$ are $\mathcal{O}(1)$ or smaller.

Multiplying both sides of Eq. (2.4.17) by the eigen-vector ψ_1 and discarding $\mathcal{O}(\Delta t^3)$ terms, we have

$$\mathcal{R}\psi = -\beta\Delta t\mathcal{D}\psi_1 + D_1\Delta^2\mathcal{D}^2\psi_1.$$

Using the fact that λ_1 and μ_1 are eigen-values associated with ψ_1, it gives

$$\mu_1\psi_1 = -\beta\Delta t\lambda_1\psi_1 + D_1\Delta^2\lambda_1^2\psi_1 + (D_2\Delta^2(\mathcal{D}\Omega - \Omega\mathcal{D}) + D_3\Delta^2\Omega^2 + D_4\Delta^2(\boldsymbol{u}\cdot\nabla)\mathcal{D})\psi_1$$

Then taking the dot product with ψ_1 itself, it follows

$$\begin{aligned}\mu_1 = &-\beta\Delta t\lambda_1 + D_1\Delta^2\lambda_1^2 \\ &+ < (D_2\Delta^2(\mathcal{D}\Omega - \Omega\mathcal{D}) + D_3\Delta^2\Omega^2 + D_4\Delta^2(\boldsymbol{u}\cdot\nabla)\mathcal{D})\psi_1, \psi_1 > .\end{aligned}$$

By Assumption 2.4.3, $< (D_2\Delta^2(\mathcal{D}\Omega - \Omega\mathcal{D}) + D_3\Delta^2\Omega^2 + D_4\Delta^2(\boldsymbol{u}\cdot\nabla)\mathcal{D})\psi_1, \psi_1 > \sim \mathcal{O}(1)$. Then, we have

$$D_1 = \frac{\mu_1 + \beta\Delta t\lambda_1 + \mathcal{O}(1)}{\Delta^2\lambda_1^2}.$$

Note that $\beta\Delta t \sim 1$, then

$$D_1 \sim \frac{1}{\Delta^2}.$$

□

Finally, by dimensional analysis and the argument for homogeneous turbulence in Section 2.3.1, the nonlinear relation reads as follows:

$$\begin{aligned}\mathcal{R} &= -(C_s\Delta)^2 \|\mathcal{D}\|_F \mathcal{D} + D_1\Delta^2\mathcal{D}^2 + D_2\Delta^2(\mathcal{D}\Omega - \Omega\mathcal{D}) \\ &\quad + D_3\Delta^2\Omega^2 + D_4\Delta^2(\boldsymbol{u}\cdot\nabla)\mathcal{D}. \end{aligned} \tag{2.4.19}$$

Remark 2.4.5. *It is clear that the first order term $-\beta\Delta t\mathcal{D}$ is the Smagorinsky model, which captures the effect of dissipation due to the non-negative sign of β, although the Smagorinsky model has excessive dissipation (Clark* et al.*, 1979).*

The second order terms $\mathcal{G}$ can be divided into two components $\mathcal{G} = \mathcal{G}_1 + \mathcal{G}_2$ as follows:

$$\begin{aligned}\mathcal{G}_1 &= \xi\nabla\boldsymbol{u}\nabla\boldsymbol{u}^T + \eta\nabla\boldsymbol{u}^T\nabla\boldsymbol{u} + \zeta(\nabla\boldsymbol{u}\nabla\boldsymbol{u} + \nabla\boldsymbol{u}^T\nabla\boldsymbol{u}^T), \\ \mathcal{G}_2 &= \chi(\boldsymbol{u}\cdot\nabla)\mathcal{D}.\end{aligned}$$

The terms in $\mathcal{G}_1$ have similar effects. Analogous to the first order term, if we 'freeze' one component, say $\nabla\boldsymbol{u}^T$, it is clear that the effect of $\nabla\cdot\nabla\boldsymbol{u}$ is dissipation/anti-dissipation, depending on the signs of $\nabla\boldsymbol{u}^T$ and the coefficients. This is what enables the nonlinear model (2.4.12) *to model the backward energy cascade phenomena.*

If we 'freeze' $\boldsymbol{u}$ in $\mathcal{G}_2$ analogously, the effect of $\nabla\cdot\mathcal{G}_2$ is dispersive, which leads to different scales being separated into a train of oscillations.

In addition, for the homogenous turbulence, the coefficients D_1, D_2, D_3, D_4 are non-dimensional constants.

2.4.1 The gradient model

An alternative to the Smagorinsky model is the gradient model, where $\mathcal{R}$ is expressed as an inner product of velocity gradients,

$$\mathcal{R} = \frac{1}{12}\Delta^2 \nabla \boldsymbol{u} \nabla \boldsymbol{u}^T, \tag{2.4.20}$$

where Δ is the typical length of the large scale structure. However, the pure gradient model (2.4.20) appears to be unstable (Vreman *et al.*, 1996). Two remedies have been proposed. As explained in Remark 2.4.5, the gradient term $\nabla \boldsymbol{u} \nabla \boldsymbol{u}^T$ may introduce energy backscatter, which might make the model unstable. A limiter can be applied to prevent this anti-cascade scenario (Liu *et al.*, 1994; Vreman *et al.*, 1997). The second remedy adds the Smagorinsky model in order to suppress the instability (Clark *et al.*, 1979). However, the resultant mixed model inherits the excessive dissipation of the Smagorinsky model.

In our nonlinear model (2.4.12), the first order term recovers the Smagorinsky model and the gradient model is the first term of the second order. The coefficient can be obtained similarly by dimensionality analysis. As a matter of fact, the gradient terms of $\mathcal{G}$ in (2.4.13) have similar effects. After including more gradient terms, the nonlinear model (2.4.12) may not have excessive dissipation while remaining stable.

2.4.2 Generic nonlinear model of Lund and Novikov

In the generic nonlinear model, the subgrid tensor is assumed to be a function of the resolved velocity field gradients and the typical scale length Δ (Lund & Novikov, 1992):

$$\mathcal{R} = F(D, \Omega, \Delta), \tag{2.4.21}$$

where Ω is the anti-symmetric part of $\nabla \boldsymbol{u}$:

$$\Omega = \frac{1}{2}\left(\nabla \boldsymbol{u} - \nabla \boldsymbol{u}^T\right).$$

The most general form of (2.4.21) is a polynomial of infinite degree in tensors of the form $D^{p_1}\Omega^{p_2}D^{p_3}\Omega^{p_4}\cdots$. From the Cayley-Hamilton theorem, symmetry properties

and other assumptions, the following generic polynomial form can be obtained:

$$\begin{aligned}\mathcal{R} &= C_1\Delta^2 \left\|\mathcal{D}\right\|_F \mathcal{D} + C_2\Delta^2\mathcal{D}^2 + C_3\Delta^2\Omega^2 \\ &\quad + C_4\Delta^2\left(\mathcal{D}\Omega - \Omega\mathcal{D}\right) + C_5\Delta^2\frac{1}{\left\|\mathcal{D}\right\|_F}\left(\mathcal{D}^2\Omega - \mathcal{D}\Omega^2\right), \end{aligned} \tag{2.4.22}$$

where the $C_i,\ i = 1, \cdots, 5$, are constants. Meneveau *et al.* (1992) found that no significant improvement is achieved over the linear model in the prediction of the subgrid tensor eigenvectors. *A priori* tests by Horiuti (2001) have shown that the $(\mathcal{D}\Omega - \mathcal{D}\Omega)$ term is responsible for a significant improvement of the correlation coefficient with the true subgrid tensor.

We make the following observations comparing the nonlinear model (2.4.19) to the generic nonlinear model (2.4.22):

(i) Both models include the Smagorinsky model, which models the forward energy cascade.

(ii) Other than the Smagorinsky term, both models successfully obtain the terms $\mathcal{D}^2$, $(\mathcal{D}\Omega - \Omega\mathcal{D})$ and Ω^2, which may model the backward energy cascade effect.

(iii) Our model (2.4.17) does not have the term

$$\frac{1}{\left\|\mathcal{D}\right\|_F}\left(\mathcal{D}^2\Omega - \mathcal{D}\Omega^2\right).$$

This is the third order term in our nonlinear terms and can be recaptured if we increase by one more order in our numerical approximation.

(iv) The generic model (2.4.22) fails to include the terms $(\boldsymbol{u}\cdot\nabla)\mathcal{D}$. In fact, the term $(\boldsymbol{u}\cdot\nabla)\mathcal{D}$ models the dispersive effect.

2.5 Conclusions and discussions

In this chapter, a multiscale analysis for the Navier-Stokes equations was briefly introduced. The velocity has been decomposed formally into two parts using a nested multiscale expansion: the large-scale and the small-scale components. It is noted that the velocity is not required to have a two-scale structure. The velocity could

include infinitely many scales. The formal separation into two scales is achieved in the spectral space. Basically, the velocity is separated into a low-frequency part and a high-frequency part by setting up a cutting frequency. An example in the case of turbulent channel flow can be found in Appendix B. Following the scale separation, a multiscale system can be derived, but this system is computationally expensive to solve even if an adaptive technique could be adopted.

By using the frame invariance property of the cell problems and an iterative homogenization of large- and small-scale velocities dynamically, the crucial structure of the Reynolds stress can be obtained explicitly for general turbulent flows. However, the explicit form of the Reynolds stress has to be analyzed for particular turbulent flows on a case by case basis. In this chapter, examples of homogeneous and channel flows are given. In the case of homogeneous turbulence, the Smagorinsky model has been fully recovered. A simplified modified-Smagorinsky model has been proposed with the aid of detailed near-wall structure in the channel flow. For both cases, the constants in the models can be calculated by locally minimizing the Reynolds stress error term from the DNS data. The numerically calculated constants are close to the values predicted by the theoretical estimate.

In order to capture the backward energy cascade phenomena, a nonlinear LES modeling is introduced using a second order approximation of the inverse flow map function $\boldsymbol{\theta}$. Not only does it bring in the anti-cascade effect, the nonlinear model also introduces a term that accounts for the dispersion. Our nonlinear model covers the mixed model which combines the Smagorinsky model and the gradient model. Furthermore, unlike the generic nonlinear model of Lund and Novikov, our nonlinear model can represent the dispersive effect. On the other hand, a term missing in our model but present in the generic nonlinear model of Lund and Novikov could be recaptured by using a third order approximation in our derivation.

The large eddy simulation technique has problems with boundary layer flows. A famous problematic example is the inner region of boundary layers, whose intrinsic scale is the wall unit. Firstly, the mechanisms generating the turbulence are associated with fixed characteristic length scales on the average. Moreover, the turbulence production is associated with a backward energy cascade, which dominates

over the cascade mechanism in certain regions of the boundary layer. Sub-grid models eventually fail to directly capture all the scales of motion responsible for turbulence production in the boundary layer, because they no longer permit a reduction of the number of degrees of freedom while ensuring at the same time a fine representation of the flow. There are two possible approaches to resolve this issue (Moin & Jimenez, 1993):

(i) Resolving the near-wall dynamics directly. Since the production mechanisms escape the scope of subgrid modeling, a sufficiently fine grid has to be used to capture the effect. Zang (1991) indicates that three grid points should be allocated in the $y^+ < 10$ zone in order to capture the production mechanisms. Chapman (1979) estimates that resolving the dynamics of the inner region requires $\mathcal{O}(Re^{1.8})$ degrees of freedom, while only $\mathcal{O}(Re^{0.4})$ are needed to represent the outer zone. In addition, non-isotropic models have to be directly resolved, and it is known that the number of degrees of freedom of the solution (in space) scales as $\mathcal{O}(Re^2)$ (Bagget *et al.*, 1997).

(ii) Wall modeling. In order to use the same order of grid points near the wall as in the outer zone, a model representing the dynamics of the inner region could be used. Since only a part of the dynamics is modeled, this introduces additional errors. The most popular wall models for large eddy simulation are the following: (i) The Schumann model and its variants, which rely on a linear relation between the wall stress and the velocity component at the first off-wall grid point (Schumann, 1975); (ii) The optimized ejection model, which is based on experimental correlation data (Marusic *et al.*, 2001); (iii) A special near-wall subgrid-scale model based on wall parallel filtering and wall-normal averaging of the streamwise momentum equation (Chung & Pullin, 2009); (iv) Hybrid RANS/LES approaches, where a RANS model is used in the near-wall region and a smooth transition to LES is made off the wall (Hamba, 2003, 2006; Spalart *et al.*, 1997; Squires *et al.*, 2005).

From the view point of the first approach, the quality of the results is essentially due to the resolution of the dynamics in the near-wall region ($y^+ < 100$). This implies

that, if a wall model is not used, the computational grid has to be fine enough to resolve the dynamics of the vortex structures. For channel flow, a Chebyshev polynomial expansion can be taken in the normal direction so that near the wall more grid points are assigned. This can be regarded as an adaptive numerical scheme. However, no flow information is embedded in the adaptivity. Because of the necessarily fine grids near the wall, the high resolution limits the possible Reynolds numbers. Even though zonal embedded grids have been employed, the largest friction Reynolds number achieved to date is $Re_\tau = 4000$ (Kravchenko *et al.*, 1996).

Chapter 3

Numerical results of the simplified Smagorinsky model

In this chapter, an extensive numerical study of the simplified Smagorinsky model (2.3.7) at two Reynolds numbers ($Re_\tau = 180$ and $Re_\tau = 395$) is presented for the channel flow. Good qualitative agreement is achieved when comparing the results of the simplified model with those obtained by DNS and experiments. However, due to experimental and modeling errors, we do observe some noticeable differences, e.g. , r.m.s vorticity fluctuations at $Re_\tau = 180$.

3.1 Numerical methods and settings

The same computational domain as that in Kim *et al.* (1987) has been employed (see Figure 3.1). The streamwise (x) and spanwise (z) computational periods are chosen to be 4π and 2π, and the half-width of the channel is 1. Fully developed turbulent flow in a channel is homogeneous in the streamwise and spanwise directions. Therefore, we assume periodic boundary conditions in these two directions. The no-slip boundary condition is chosen in the wall-normal direction (y).

The numerical scheme uses a Chebychev-tau formulation in the wall-normal direction (y) and Fourier expansions in the streamwise (x) and spanwise (z) directions. Further, we change variables in the Chebyshev expansion to take advantage of the fast Fourier transform. In the DNS by Kim *et al.* (1987), the 2/3 rule was used to remove the aliasing errors induced by the pseudo-spectral method. Here, we use the high-order Fourier smoothing method introduced by Hou & Li (2007). A low-storage

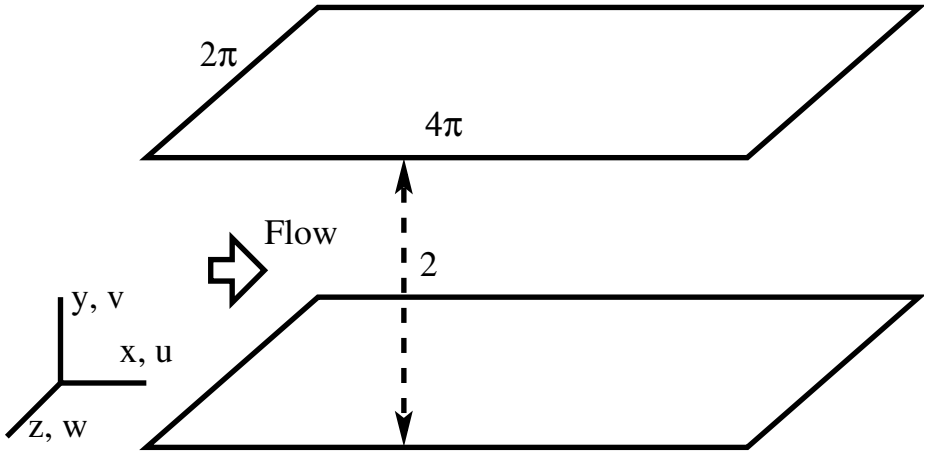

Figure 3.1: Computational domain in a channel

third-order Runga-Kutta time discretization developed by Spalart *et al.* (1994) is used. A constant pressure gradient is applied to drive the flow in the streamwise direction. For a DNS with $Re_\tau = 180$, Kim *et al.* (1987) used an effective resolution of $128(x) \times 129(y) \times 128(z)$, while we use only $64(x) \times 65(y) \times 64(z)$ for the simplified Smagorinsky model. For a DNS with $Re_\tau = 395$, Moser *et al.* (1999) used an effective resolution of $256(x) \times 257(y) \times 256(z)$. In comparison, we use only $128(x) \times 129(y) \times 128(z)$ for the simplified model.

The fully developed turbulent flow in a channel using the simplified Smagorinsky model is obtained by taking the first N modes of the velocities given by the DNS as initial data, where N is the number of grid points used for the simulation of the simplified model. The code is run by integrating forward in time until a statistical steady state is achieved. The steady state is identified by the quasi-periodic behavior of the total kinetic energy and by a linear profile of total shear stress, $-\overline{u'v'} + (1/Re)\partial\bar{u}/\partial y$. Once the velocity field reaches the statistical steady state, the simplified model is further integrated in time to obtain a time-average of various statistical quantities. The statistical quantities are obtained by averaging over the horizontal plane (both homogeneous directions x and z) and time t. The coordinates and flow quantities are normalized by the channel half width δ and the friction velocity $u_\tau = (\tau_w/\rho)^{1/2}$, where τ_w is the statistically averaged wall shear stress and ρ is the density.

3.1.1 Model validation

To validate the simplified model (2.3.7) using the multiscale analysis, we make a complete comparison of the mean streamwise velocity profiles and r.m.s. velocity fluctuations among DNS, the Smagorinsky model, and the simplified model. The comparison of the mean streamwise velocity is displayed in Figure 3.2. In the near-wall region $y^+ < 10$, the three profiles collide and all of them obey the linear relation very well. The simplified model approaches DNS a little more closely than it does the Smagorinsky model in the region $10 < y^+ < 40$. This is because the Smagorinsky model includes too much diffusion. While near the center of the channel flow, the profile of the simplified model is noticeably lower than those of DNS and the Smagorinsky model. The main reason has been explained in Section 2.3.2, i.e. , the asymptotic structure near the wall is not valid for the center of the channel flow. Figure 3.3 shows the r.m.s. velocity fluctuations for $Re_\tau = 180$. Generally, both the simplified model and Smagorinsky model give satisfactory performance when compared to DNS. Note that the simplified model performs better than the Smagorinsky model near the wall $y^+ < 25$ for r.m.s. u and w. Away from the wall, the Smagorinsky model approaches DNS more closely. Again, this is because the asymptotic analysis in Section 2.3.2 holds within the boundary layer. In addition, the Smagorinsky model slightly exceeds the simplified model in r.m.s. normal velocity fluctuation throughout the computational domain.

3.2 Turbulent structure near the wall

The two most prominent structural features of the near-wall turbulence are illustrated in Figures 3.4 and 3.5:

(i) Streaks of low momentum fluid, regions of $u' < 0$, which have been lifted into the buffer region by the vortices.

(ii) Elongated streamwise vortices, identified by the region of negative λ_2 proposed by Jeong & Hussain (1995).

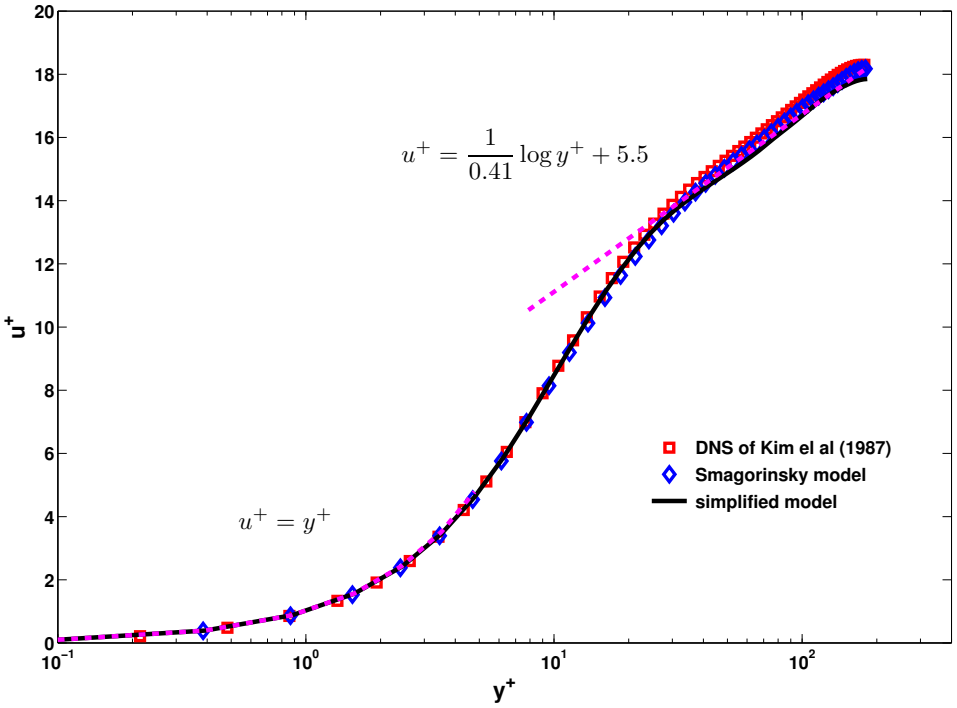

Figure 3.2: Comparison of mean streamwise velocity profiles for $Re_\tau = 180$. □: DNS by Kim *et al.* (1987); ◇: the Smagorinsky model; solid line: the simplified model

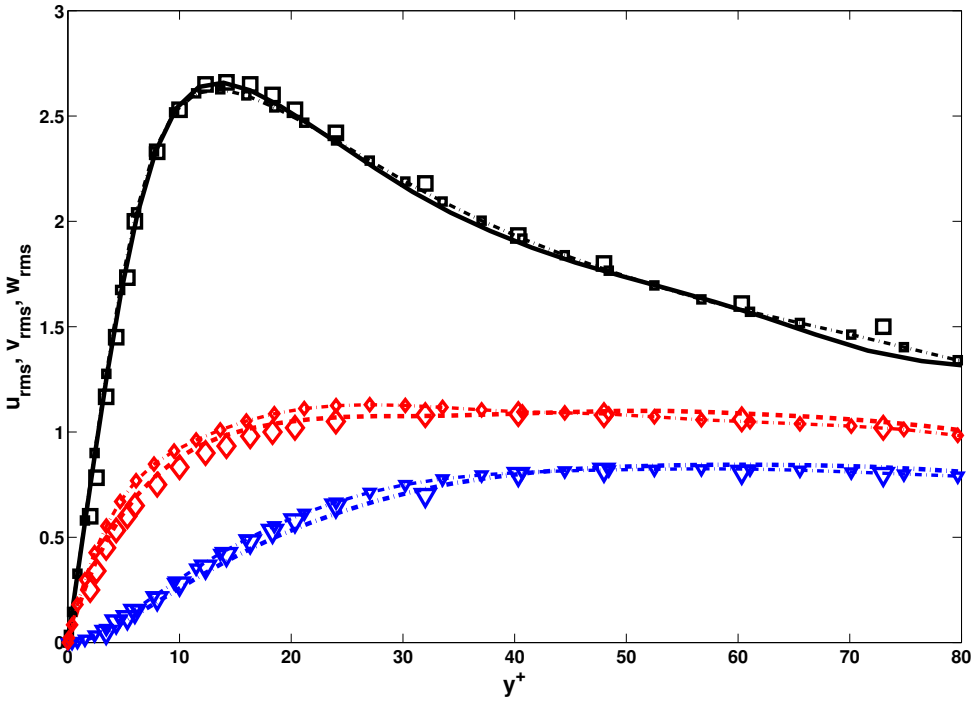

Figure 3.3: Comparison of r.m.s. velocity fluctuations for $Re_\tau = 180$. DNS by Kim *et al.* (1987): $\square$, u_{rms}; $\bigtriangledown$ v_{rms}, $\diamond$ w_{rms}. Smagorinsky model: dashed line with $\square$, u_{rms}, dashed line with $\bigtriangledown$: v_{rms}; dashed line with $\diamond$, w_{rms}. Simplified model: solid line, u_{rms}; dash-dot line, v_{rms}, dashed line, w_{rms}

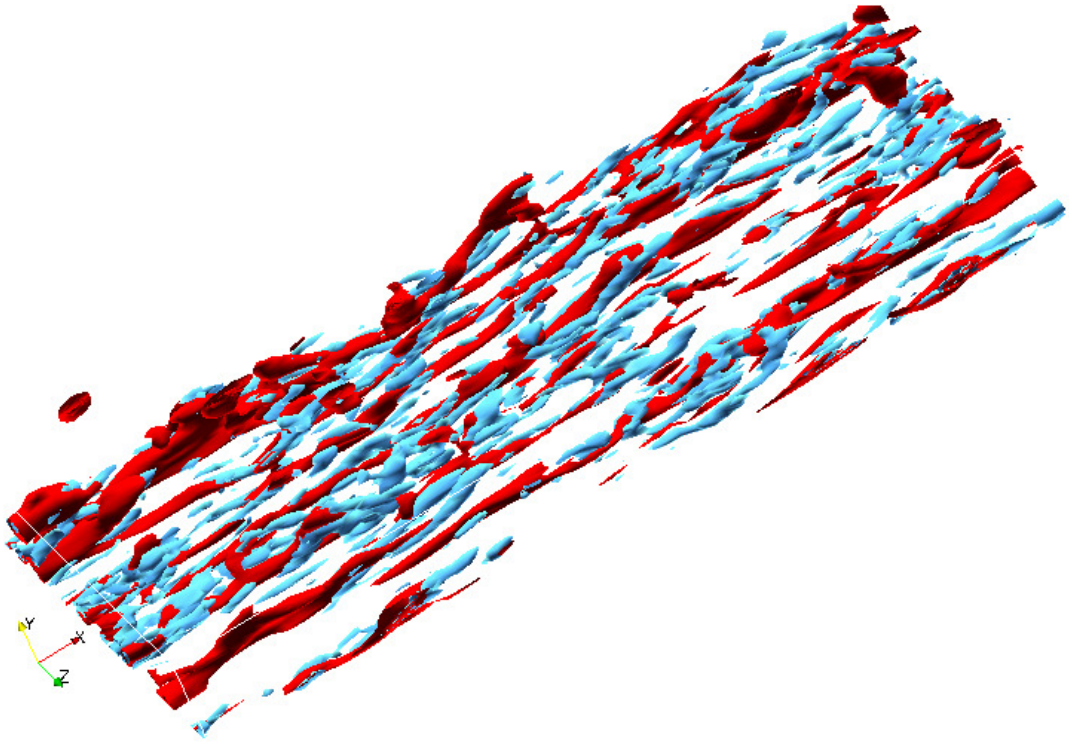

Figure 3.4: Turbulent structure near the wall obtained using the simplified Smagorinsky model. Iso-surface of streamwise vortices (blue) indicated by the λ_2 definition ($\lambda_2 = -\lambda_{\mathrm{rms,max}} = -176.54$) (Jeong & Hussain, 1995) and lifted low-speed streaks (red) denote $u' < 0$ in the region $0 < y^+ < 60$, $Re_\tau = 180$.

Currently, it is well accepted that by Biot-Savart induction, near-wall streamwise vortices lift the low-speed fluid to form the streaks. On the other hand, the streamwise vortices are generated from the many normal-mode-stable streaks via a new scenario, identified by the streak transient growth (STG) mechanism (for details, see Schoppa & Hussain, 2002). The phase averages of the vortices, their characteristics and their dynamical role have been discussed by Jeong *et al.* (1997). Figure 3.4 is quite consistent with these details of near-wall structures.

3.3 Mean flow properties

Figure 3.6 shows the profile of the mean velocity normalized by the wall-shear velocity u_τ for $Re_\tau = 180$. In the viscous sublayer $y^+ < 10$, we observe excellent agreement with the linear relation $u^+ = y^+$. In the log-law region ($y^+ > 30$, $y/\delta < 0.3$), it is

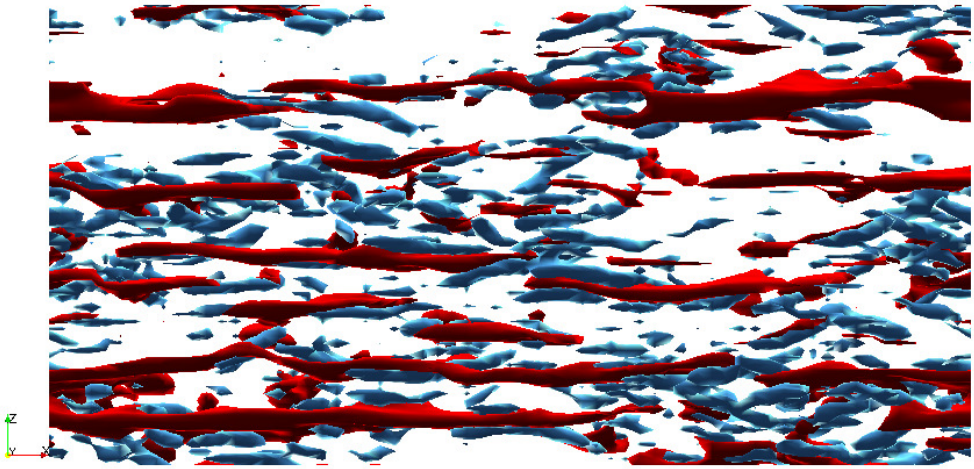

Figure 3.5: Top view of turbulent structure near the wall. Iso-surface of streamwise vortices (blue) indicated by the λ_2 definition ($\lambda_2 = -\lambda_{\mathrm{rms,max}} = -176.54$) (Jeong & Hussain, 1995) and lifted low-speed streaks (red) denote $u' < 0$ in the region $0 < y^+ < 60$, $Re_\tau = 180$.

well known that the logarithmic law of the wall due to von Kármán (1930) can be expressed as

$$u^+ = \frac{1}{\kappa} \ln y^+ + B,$$

where $\kappa = 0.41$ is the Kármán constant and B is the additive constant. In the simplified Smagorinsky model, the additive constant B is 5.5, which is the approximate value reported in the literature (Eckelmann, 1974; Kim *et al.*, 1987; Spalart, 1988). In the log-law region, the profiles of the mean streamwise velocity of both the simplified model and DNS (Kim *et al.*, 1987) are lower than in the experimental results reported by Eckelmann (1974).

The profile of the mean velocity u^+ for $Re_\tau = 395$ is shown in Figure 3.7 and compared to the DNS results obtained by Moser *et al.* (1999) and the experimental results by Hussain & Reynolds (1970) for $Re_\tau = 642$. In the viscous sublayer, the results of the simplified model obey the linear relation accurately. The profile conforms to the log law with the constant $B = 5.5$ in the log-law region, while both DNS by Moser *et al.* (1999) and our simplified model give slightly larger values of u^+ than the experiments by Hussain & Reynolds (1970).

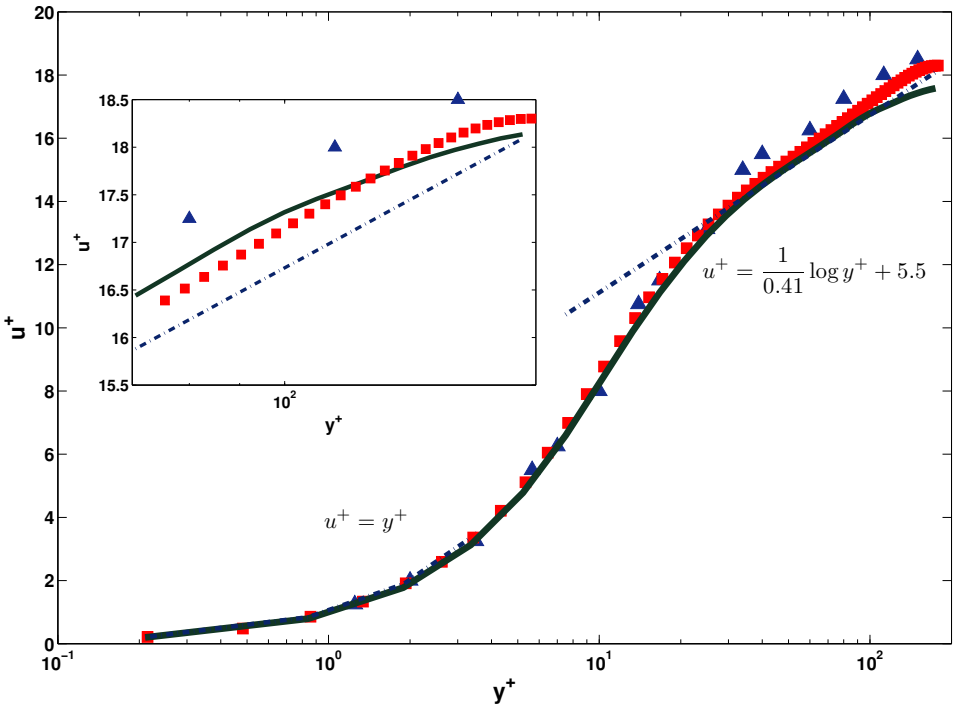

Figure 3.6: Profiles of the mean streamwise velocity u^+ for $Re_\tau = 180$, compared with DNS by Kim *et al.* (1987) and experiments by Eckelmann (1974). △, experiments by Eckelmann (1974); □, DNS by Kim *et al.* (1987); solid-line, simplified model; dash-dot line, linear relation and log-law

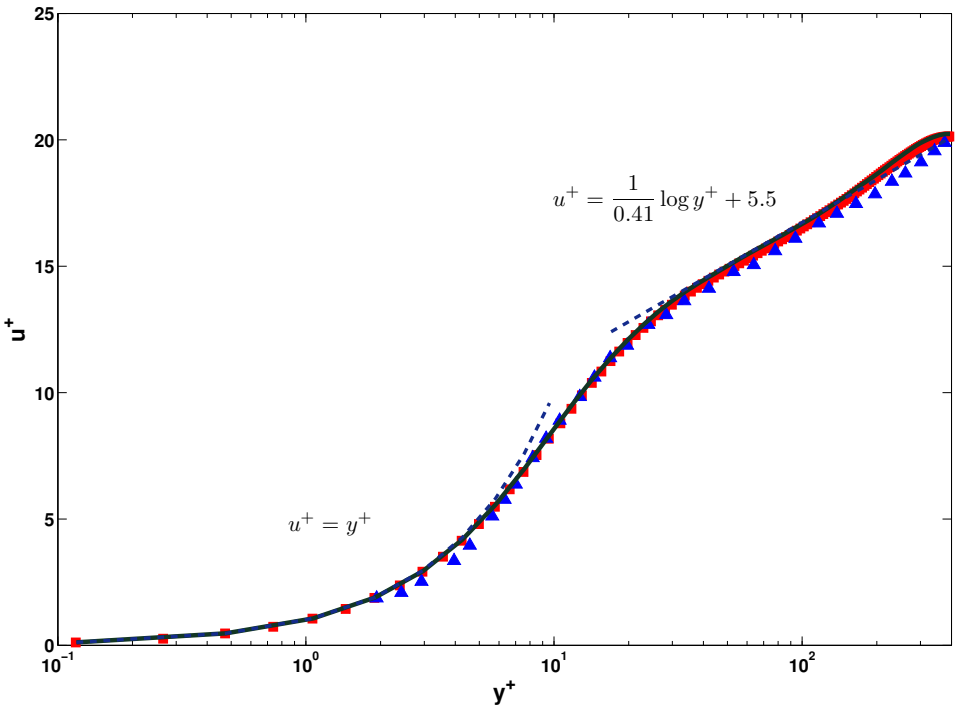

Figure 3.7: Near wall profiles of the mean streamwise velocity u^+ for $Re_\tau = 395$, compared with DNS by Moser *et al.* (1999) and experiments by Hussain & Reynolds (1970). □, DNS by Moser *et al.* (1999); △, experiments by Hussain & Reynolds (1970); solid-line, simplified model; dashed line, linear relation and log-law

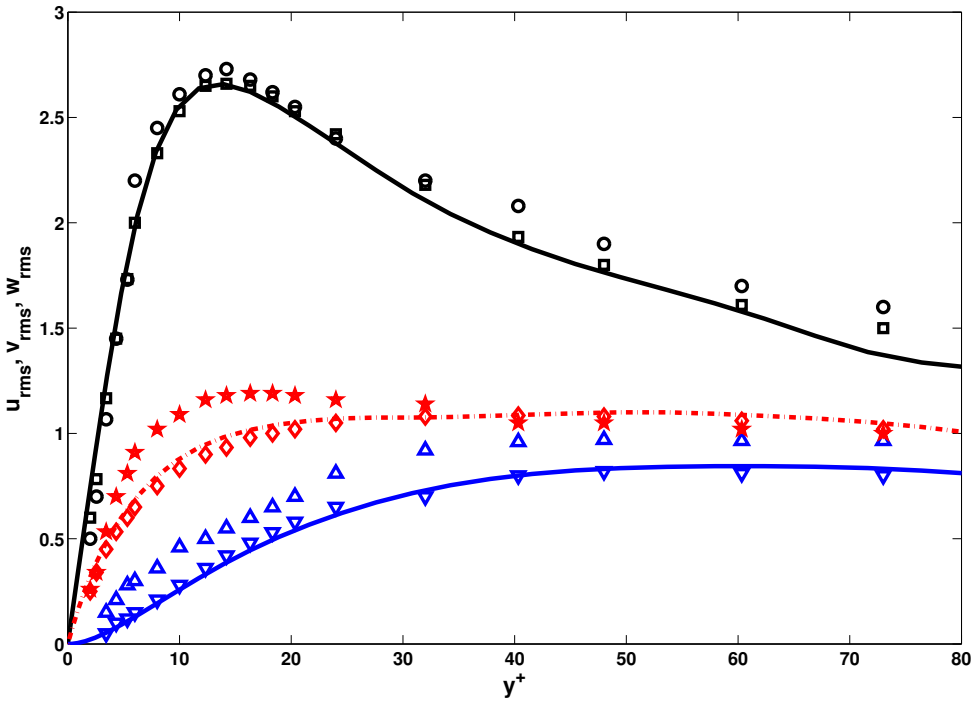

Figure 3.8: R.m.s. velocity fluctuations normalized by the wall shear velocity u_τ for the simplified model with $Re_\tau = 180$, compared with DNS by Kim *et al.* (1987) and experiments by Kreplin & Eckelmann (1979). $\circ$ u_{rms}, $\triangle$ v_{rms}, $\star$ w_{rms} by Kreplin & Eckelmann (1979); $\square$ u_{rms}, $\triangledown$ v_{rms}, $\diamond$ w_{rms} by Kim *et al.* (1987); solid line u_{rms}, dash-dot line v_{rms}, dashed line w_{rms} by simplified model

3.4 Turbulence intensities

One of the Reynolds number effects in wall-bounded turbulence is in the root-mean-square (r.m.s.) velocity profiles (u_{rms}, v_{rms}, w_{rms}). These turbulence intensities normalized by the friction velocity are shown and compared with DNS (Kim *et al.*, 1987; Moser *et al.*, 1999) and experiments (Kreplin & Eckelmann, 1979) in Figure 3.8 for $Re_\tau = 180$ and Figure 3.9 for $Re_\tau = 395$.

In the case of $Re_\tau = 180$, the profiles obtained by the simplified model are in good agreement with those of Kim *et al.* (1987) and Kreplin & Eckelmann (1979). The peak value of $u_{\rm rms}$, about 2.5, is lower than that by DNS. This may be due to the high damping coefficient near the wall. As pointed out by Kim *et al.* (1987), the values of numerical simulations are lower than the measured values in the experiment by

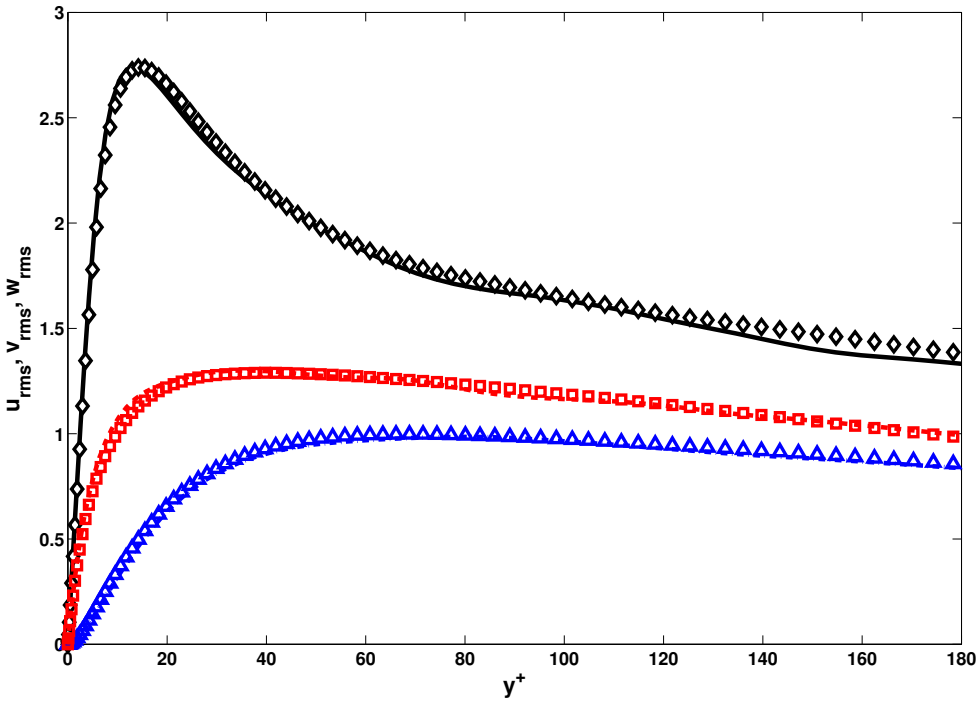

Figure 3.9: R.m.s. velocity fluctuation normalized by the wall shear velocity u_τ for the simplified model with $Re_\tau = 395$, compared with DNS by Moser *et al.* (1999). $\diamond$ u_{rms}, $\triangle$ v_{rms}, $\square$ w_{rms} by Moser *et al.* (1999); solid line u_{rms}, dash-dot line v_{rms}, dashed line w_{rms} by simplified model

Kreplin & Eckelmann (1979), principally because of unavoidable hot-wire errors in near-wall measurements. The r.m.s. normal velocity fluctuation $v_{\rm rms}$ is in remarkably good agreement with DNS, but both are lower than the experimental results near the wall.

In the case of $Re_\tau = 395$, the peak value of $u_{\rm rms}$ is marginally lower than DNS results by Moser *et al.* (1999) around $y^+ = 20$. The values of $v_{\rm rms}$ and $w_{\rm rms}$ of the simplified model are in good agreement with those obtained by DNS throughout the normal direction. Moreover, the values of $u_{\rm rms}$ match quite well the DNS result throughout the computational domain.

As observed by Spalart (1988), the peak value of $u_{\rm rms}$ is Re dependent, which is clearly shown by comparing $u_{\rm rms}$ in Figure 3.8 with Figure 3.9. Antonia *et al.* (1992) pointed out that the Reynolds number dependence of $w_{\rm rms}$ is significant compared to those of $u_{\rm rms}$ and $v_{\rm rms}$. This is also evident in Figures 3.8 and 3.9. In the presented results for the simplified model, all three r.m.s. velocity fluctuations are enhanced with increasing Re. This may be because of the remarkable increase of the energy redistribution (Abe *et al.*, 2001).

3.5 Reynolds shear stress

The total shear stress, $-\overline{u'v'}+(1/Re)\partial\bar{u}/\partial y$, is shown in Figure 3.10 for the simplified model at two Reynolds numbers $Re_\tau = 180$ and $Re_\tau = 395$. In the fully developed turbulent channel flow considered in this section, this profile is a straight line when the flow reaches an equilibrium state. For this simplified model, Figure 3.10 clearly shows that our computations of the two Reynolds numbers have achieved statistical steady state. The behavior of the Reynolds shear stress in the immediate vicinity of the wall can be explained by the following nondimensionalized equation (Tennekes & Lumley, 1972)

$$-\frac{\overline{u'v'}}{u_\tau^2}+\frac{{\rm d}u^+}{{\rm d}y^+}=1-\frac{y^+}{\delta^+}, \tag{3.5.1}$$

where $\delta^+ = u_\tau\delta/\nu$. The stress at the wall is purely viscous. Nondimensionalized in this way, the Reynolds number dependence is absorbed into the scale of y so that the viscous term does not become small at large Reynolds numbers. Thus, for small

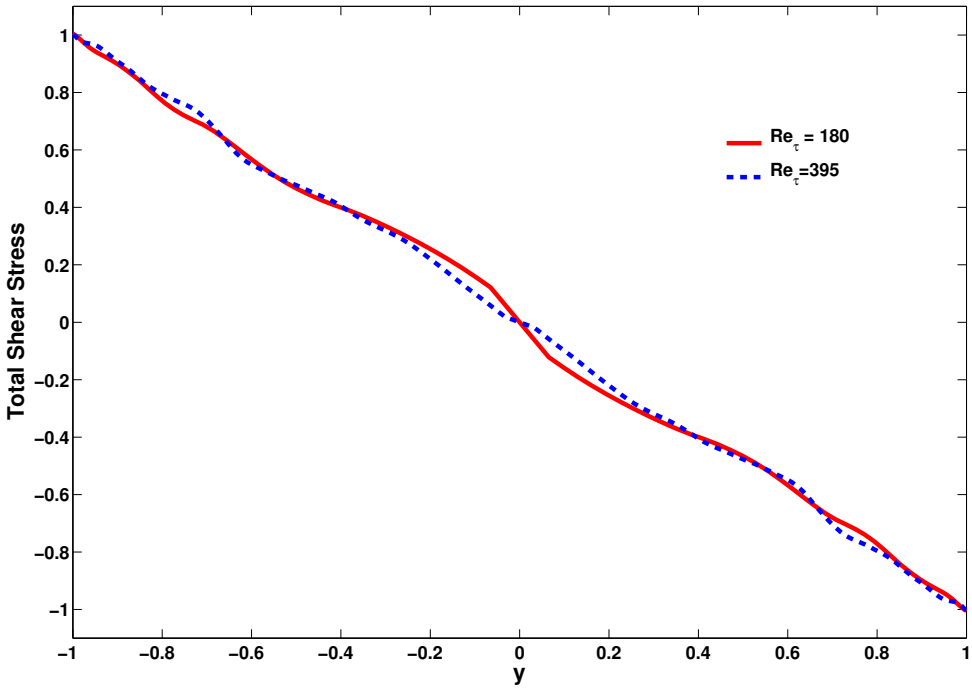

Figure 3.10: Total shear stress, $-\overline{u'v'} + (1/\mathrm{Re})\partial\bar{u}/\partial y$, normalized by the wall shear velocity for $Re_\tau = 180$ (solid line) and $Re_\tau = 395$ (dashed line)

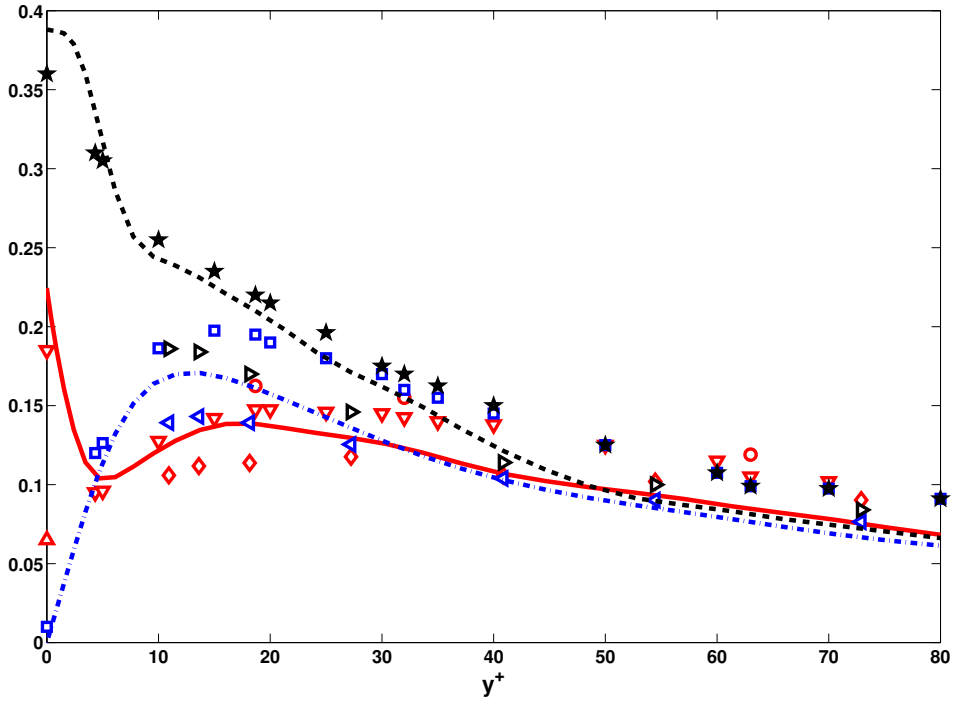

Figure 3.11: R.m.s. vorticity fluctuations normalized by the mean shear near the wall for $Re_\tau = 180$, compared with DNS by Kim *et al.* (1987) and experiments by Kreplin & Eckelmann (1979), Kastrinakis & Eckelmann (1983) and Balint *et al.* (1991). $\diamond$ ω_x, $\triangleleft$ ω_y, $\triangleright$ ω_z by Balint *et al.* (1991); $\triangle$ ω_x by Kreplin & Eckelmann (1979); $\circ$ ω_x by Kastrinakis & Eckelmann (1983); $\bigtriangledown$ ω_x, $\square$ ω_y, $\star$, ω_z by Kim *et al.* (1987); solid line ω_x, dash-dot line ω_y, dashed line ω_z by simplified model

y^+/δ^+, the Reynolds shear stress does not vary with Reynolds numbers and collapses into one curve. In Figure 3.10, the two lines are close to each other, especially near the wall when $|y|$ is close to 1. Also, it can be seen that the slopes for $Re_\tau = 180$ and $Re_\tau = 395$ are close to 1 as well, as confirmed in (3.5.1). Again, the difference is mainly due to the modeling error when the simplified form is also used in the center of the channel.

3.6 Vorticity

The r.m.s. vorticity fluctuations normalized by the mean shear at the wall $\omega_i \nu / u_\tau^2$, $(i = x, y, z)$ are shown in Figures 3.11 and 3.12 for $Re_\tau = 180$ and $Re_\tau = 395$, respectively.

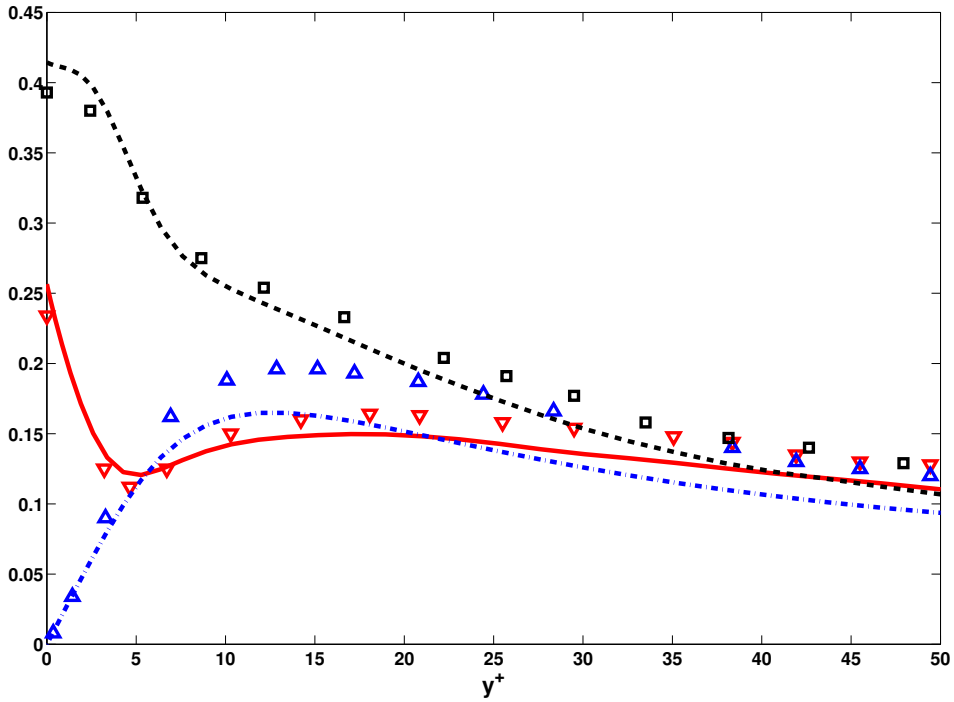

Figure 3.12: R.m.s. vorticity fluctuations normalized by the mean shear near the all for $Re_\tau = 395$, compared with DNS by Moser *et al.* (1999). $\bigtriangledown$ ω_x, $\bigtriangleup$ ω_y, $\square$ ω_z by Moser *et al.* (1999); solid line ω_x, dash-dot line ω_y, dashed line ω_z by simplified model

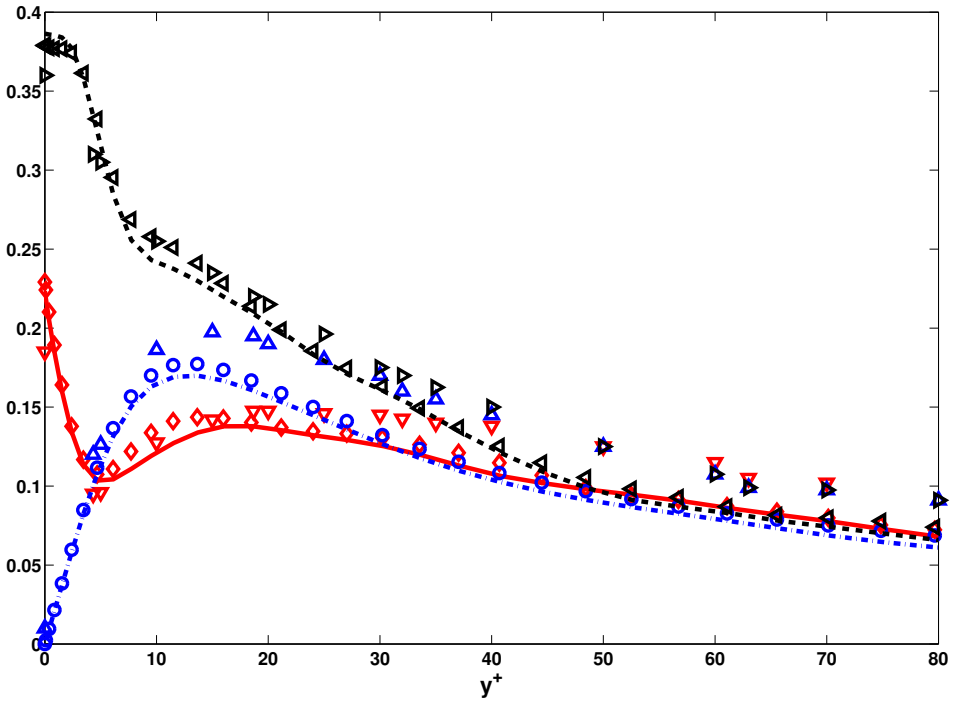

Figure 3.13: R.m.s. vorticity fluctuations normalized by the mean shear near the wall, $Re_\tau = 180$. Simplified model: solid line, ω_x; dash-dot line, ω_y; dashed line, ω_z. DNS by Kim *et al.* (1987): $\bigtriangledown$, ω_x; $\bigtriangleup$, ω_y; $\triangleright$, ω_z. Smagorinsky: $\diamond$, ω_x; $\bigcirc$, ω_y; $\triangleleft$, ω_z

The simplified model results agree well with the DNS by Kim *et al.* (1987). On the wall, the values of $\omega_x \nu / u_\tau^2$ given by the simplified multiscale model and DNS are larger than those obtained experimentally by Kreplin & Eckelmann (1979). As pointed out in Kim *et al.* (1987), most of the existing data in the wall region gathered using standard hot-wire techniques may contain significant error caused by cross-contamination. Away from the wall, the simplified model performs slightly worse than DNS Kim *et al.* (1987) when compared to the limited experimental data of Kastrinakis & Eckelmann (1983) in terms of the normalized r.m.s. ω_x, but slightly better than DNS when compared to the experiment by Balint *et al.* (1991). In addition, distinct differences between the simplified model and DNS is observed for the normalized r.m.s. ω_y, although the profile from the simplified model is closer to that from the experiment by Balint *et al.* (1991). In order to examine the source of discrepancy numerically, we plot the profiles from the simplified model, DNS, and the Smagorinsky model in Figure 3.13. In all three components, the Smagorinsky model slightly outperforms the simplified model, because the latter extends the results of asymptotic analysis to the center, which incurs additional model error. However, there is still noticeable difference from DNS for the Smagorinsky model. Therefore, the main reason of discrepancy between DNS and the Smagorinsky and the simplified models is the error introduced by the modeling process.

Near the wall, the streamwise and spanwise vorticity fluctuations increase with increasing Re. The r.m.s. ω_z especially shows a larger value for a higher Re. This is simply because of the large shear stress in the immediate vicinity of the wall. To see this, write down the vorticity equation in the local coordinates (x, n, s) (Lamb, 1945) for linearized perturbations of a $U(x)$ streak distribution. The inviscid evolution equation for the vorticity perturbation ω_x', which is the most important component, can be derived as

$$\frac{\partial \omega_x'}{\partial t} + \bar{u}\frac{\partial \omega_x'}{\partial x} = h_s \Omega \frac{\partial u_x'}{\partial s} + h_n \omega_n' \frac{\mathrm{d}\bar{u}}{\mathrm{d}n} = \Omega \frac{\partial u_s'}{\partial x}, \tag{3.6.1}$$

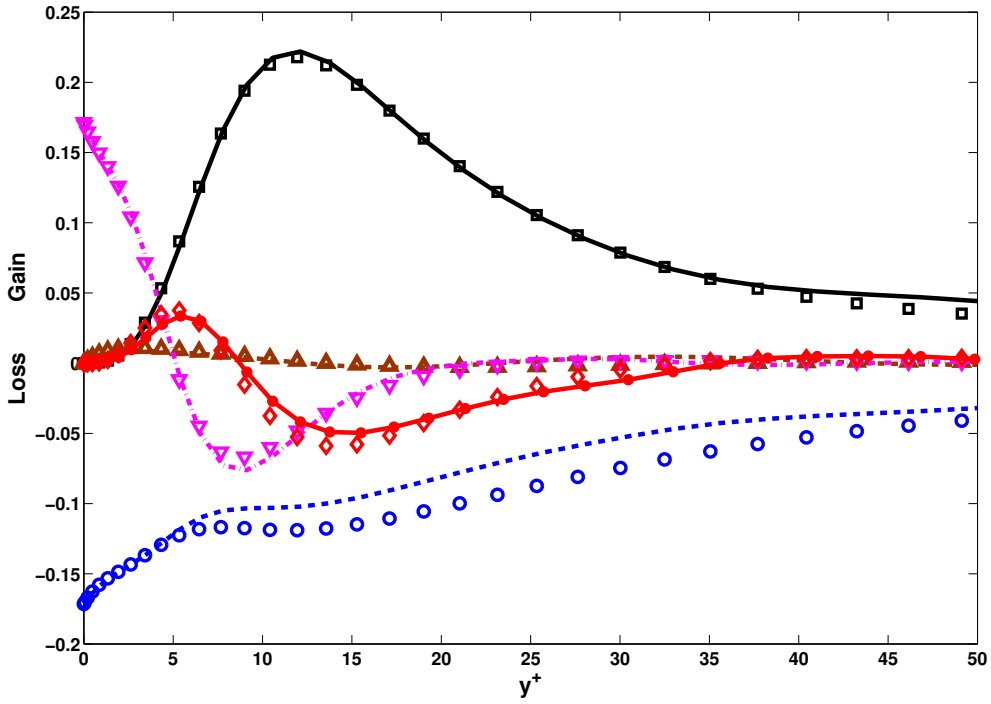

Figure 3.14: The turbulent-kinetic budget normalized by ν/u_τ^4 near the wall for $Re_\tau = 180$, compared with DNS by Kim *et al.* (1987). Production term: simplified model, solid line; DNS, □. Diffusion term: simplified model, dash-dash line; DNS, ◯; Pressure transport term: simplified model, dash-dash line with ◯; DNS, △. Viscous diffusion term: simplified model, dash-dot line; DNS, ▽. Turbulent convection term: simplified model, solid line with ◯; DNS, ⋄

where the direction cosine amplitudes h_n and h_s satisfy

$$h_n^2 = \left(\frac{\partial n}{\partial y}\right)^2 + \left(\frac{\partial n}{\partial z}\right)^2, \quad h_s^2 = \left(\frac{\partial s}{\partial y}\right)^2 + \left(\frac{\partial s}{\partial z}\right)^2. \tag{3.6.2}$$

The base flow vorticity is given by $\Omega = -h_n \mathrm{d}\bar{u}/\mathrm{d}n$ in local coordinates, which permits simplification by combining the two ω_x' production terms. Thus, the profile of u_s' is critical for ω_x' generation. This has been illustrated in the streak transient growth mechanism for the generation of near-wall streamwise vortices (Schoppa & Hussain, 2002).

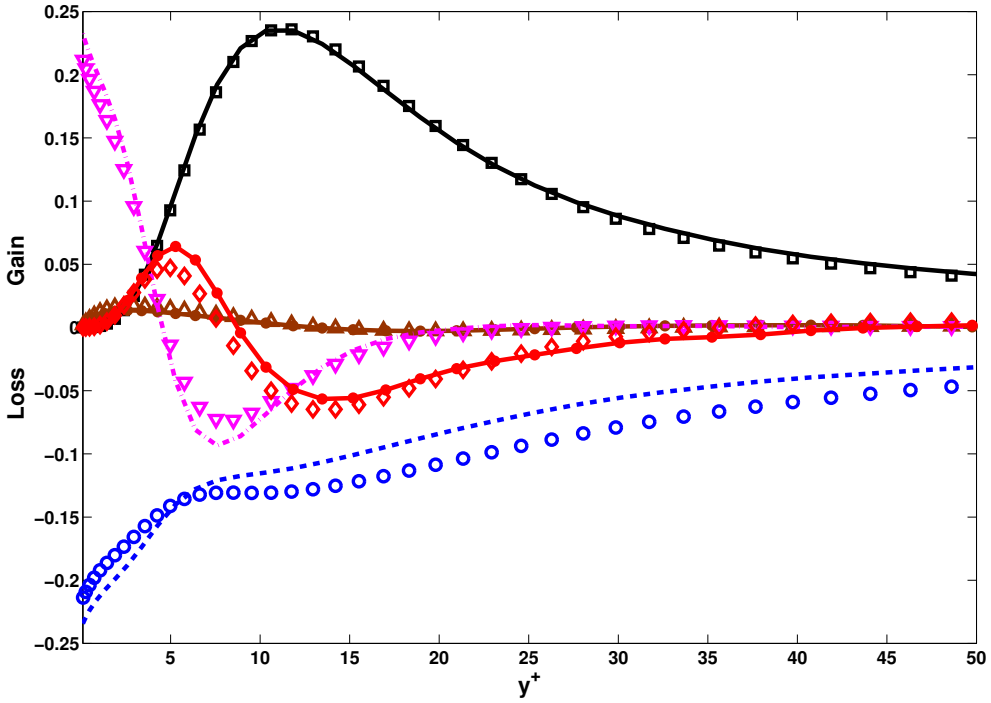

Figure 3.15: The turbulent-kinetic budget normalized by ν/u_τ^4 near the wall for $Re_\tau = 395$, compared with DNS by Moser *et al.* (1999). Production term: simplified model, solid line; DNS, $\square$. Diffusion term: simplified model, dash-dash line; DNS, $\bigcirc$; Pressure transport term: simplified model, dash-dash line with $\bigcirc$; DNS, $\triangle$. Viscous diffusion term: simplified model, dash-dot line; DNS, $\bigtriangledown$. Turbulent convection term: simplified model, solid line with $\bigcirc$; DNS, $\diamond$

3.7 Budget of turbulent kinetic energy k

For fully developed turbulent channel flow, the balance equation for turbulent kinetic energy is (Pope, 2000)

$$0 = \mathcal{P} - \varepsilon + \nu\frac{\mathrm{d}^2 k}{\mathrm{d}y} - \frac{\mathrm{d}}{\mathrm{d}y}\langle\tfrac{1}{2}v\mathbf{u}\cdot\mathbf{u}\rangle - \frac{1}{\rho}\frac{\mathrm{d}}{\mathrm{d}y}\langle vp'\rangle. \tag{3.7.1}$$

Budget terms of the turbulent kinetic energy in (3.7.1) are given by

(i) the production term

$$\mathcal{P} = -\langle u_i' u_j'\rangle\frac{\partial\langle U_i\rangle}{\partial y}, \tag{3.7.2}$$

(ii) the diffusion term

$$-\varepsilon = -\nu\left\langle\frac{\partial u_i'}{\partial x_k}\frac{\partial u_i'}{\partial x_k}\right\rangle, \tag{3.7.3}$$

(iii) the viscous dissipation term

$$\nu\frac{\mathrm{d}^2 k}{\mathrm{d}y}, \tag{3.7.4}$$

(iv) the turbulent convection term

$$-\frac{\mathrm{d}}{\mathrm{d}y}\langle\tfrac{1}{2}v'\mathbf{u}'\cdot\mathbf{u}'\rangle, \quad \text{and} \tag{3.7.5}$$

(v) the pressure transport term

$$-\frac{1}{\rho}\frac{\mathrm{d}}{\mathrm{d}y}\langle v'p'\rangle. \tag{3.7.6}$$

Figures 3.14 and 3.15 show the budget terms of the turbulent kinetic energy normalized by ν/u_τ^4 for Reynolds number $Re_\tau = 180$ and $Re_\tau = 395$ obtained by the simplified model. The results are compared with DNS by Kim *et al.* (1987) and Moser *et al.* (1999).

For $Re_\tau = 180$, each kinetic energy budget term obtained by the simplified model agrees well with the DNS results by Kim *et al.* (1987). More specifically, the production behaves like the order of y^3 from 0 near the wall. For the simplified model, the production reaches its peak value at around $y^+ = 12$, where the production-to-dissipation ratio is approximately 1.8, which agrees with the ratio obtained by Kim *et al.* (1987).

The effects of different Reynolds numbers on all these budget terms are reflected in the comparison of Figures 3.14 and 3.15 for $Re_\tau = 180$ and $Re_\tau = 395$, respectively. The values of all terms in the budget of the turbulent kinetic energy increase with the increase of Re_τ. Particularly, the wall values of the dissipation and the viscous dissipation increase remarkably with the increasing Reynolds number. This is simply because the increase of the shear stress dominates the decrease of the viscosity (Abe *et al.*, 2001).

3.8 Conclusion and discussion

In this chapter, an extensive numerical study has been executed to validate the simplified model for turbulent channel flow by using some well-established benchmark tests. Good qualitative agreements have been shown for various statistical quantities of channel flow for two Reynolds numbers, $Re_\tau = 180$ and $Re_\tau = 395$. These include mean velocity profiles, r.m.s. velocity and vorticity fluctuations, and turbulent kinetic energy budget.

The simplified model is able to grasp the turbulent features of the near-wall structures, i.e. , the streaks of low momentum fluid and the elongated streamwise vortices. Furthermore, the simplified model gives a very good match of mean velocity profile with theory, DNS, and experiment. However, we do observe some noticeable differences among the results obtained by the simplified model, DNS, and experiments, especially in the profiles of r.m.s. velocity fluctuations near the wall. There are two sources of errors that could contribute to these discrepancies. The first one is measurement (hot wire) errors near the wall (Kim *et al.*, 1987). The second one is the modeling error. Additionally, error is introduced by applying the asymptotic analysis, which is valid in the boundary layer, to the outer layer of channel flow (see Section 2.3.2).

Chapter 4

Stochastic perspective of turbulence

Traditional turbulence models, including the Smagorinsky model presented in previous chapters, are based on Reynolds averaging techniques and give rise to modeled equations for statistical moments in general. On the other hand, due to their high irregularity, turbulent flows are characterized by stochastic processes. Lagrangian probability density function (PDF) methods have been developed to achieve closure through a modeled transport equation for the one-point, one-time PDF of certain fluid properties in turbulent flows (see Pope, 1985, 1994, 2000). Lagrangian PDF methods can handle arbitrarily complex convections and reactions naturally, without assumptions (see Pope, 1985). However, they are relatively expensive in terms of computation.

In this chapter, instead of calculating the statistics of turbulent flows using PDF methods, turbulent flows are treated as stochastic processes. However, the probabilistic dimensionality of turbulence is prohibitively huge. Even with cutting-edge computational resources with thousands of CPU cores, it is still not feasible to numerically capture all the information of turbulent flows. However, if we are only interested in certain statistical properties of turbulent flows, the effective probabilistic dimension might not be essentially large. This leads us to calculate the first several modes in the Karhunen-Loéve (K-L) expansions of the stochastic variables that are of interest, e.g. , the normal distribution of stream-wise velocity after averaging over x-z plane in turbulent channel flow.

4.1 A brief introduction to numerical stochastic PDEs

There has been growing interest and significant progress over the past decades in modeling complex physical and engineering systems with uncertainties. Consequently, many methods have been devised to address these problems. It should be noticed that stochastic systems considered in this chapter are different from classic stochastic equations (SDEs), where the random inputs are modeled processes, e.g. , Poisson process, Wiener processes, etc

One of the most commonly used and robust methods is Monte Carlo (MC) sampling and its variants. In MC methods, (independent) realizations of random inputs are generated based on their prescribed probability distribution. For each realization, once the random inputs have been generated, the system becomes deterministic and usual numerical techniques are employed to solve the resultant system. Then, the ensemble of solutions can be collected and statistical information can be extracted, e.g. , mean and variance, etc. Although MC methods are straightforward to implement with robust performance, the statistics of solutions converge relatively slowly. For example, the mean value typically converges at the rate of $1/\sqrt{N}$, where N is the number of realizations (Fishman, 1996). For systems that are computationally intensive in their deterministic settings, it is prohibitively expensive to perform MC simulations. Techniques have been developed to expedite the convergence, e.g. , quasi-Monte Carlo sampling (see Niederreiter *et al.*, 1998, for instance).

Recently, the generalized polynomial chaos (gPC) method has been developed and is receiving more and more attention (Xiu & Karniadakis, 2002). Using the gPC method, stochastic solutions are expanded as a series of orthogonal polynomials of the input random parameters. The prominent shortcoming of the gPC method is that the types of orthogonal polynomials are chosen empirically according to the distributions of the input random parameters. If the stochastic systems are highly nonlinear and correlated, there is no guarantee that the correspondence between the distribution of the random input and the type of orthogonal polynomials remains valid.

Inspired by the multiscale finite element method (Hou & Wu, 1997) and the proper

orthogonal decomposition (POD) method (Sirovich, 1987; Venturi *et al.*, 2008), a new algorithm, the data-driven stochastic method (DDSM), has been proposed (Cheng *et al.*, 2011) and successfully combined with (adaptive) ANOVA to address the issue of high dimensionality in random space (Hu *et al.*, 2012). Efforts have been taken to construct gPC bases under which the stochastic solutions have sparse decompositions based on Karhunen-Loève (K-L) expansions. Generally, those gPC bases cannot be derived in an explicit analytic form, but they can be calculated numerically and stored, along with their moments, for future use.

4.2 The data-driven stochastic method

Consider the stochastic PDE

$$\begin{aligned} &\mathcal{L}(t,\boldsymbol{x},\omega)u(t,\boldsymbol{x},\omega) = f(t,\boldsymbol{x},\omega), \\ &u(0,\boldsymbol{x},\omega) = u_0(\boldsymbol{x},\omega), \\ &\alpha u(t,\boldsymbol{x},\omega) + \beta\partial_{\boldsymbol{x}} u(t,\boldsymbol{x},\omega) = u_{\partial D}(t,\boldsymbol{x},\omega), \quad \text{on boundary } \partial D \end{aligned} \tag{4.2.1}$$

where $t \in [0,T],\ \boldsymbol{x} \in D,\ \omega \in \Omega$, and $\mathcal{L}(t,\boldsymbol{x},\omega)$ is a stochastic differential operator. The stochastic ingredients may reside in the differential operator $\mathcal{L}(t,\boldsymbol{x},\omega)$, forcing term $f(t,\boldsymbol{x},\omega)$, initial condition $u_0(\boldsymbol{x},\omega)$, and/or boundary condition $u_{\partial D}(t,\boldsymbol{x},\omega)$.

In DDSM, the attempt has been made to construct gPC bases under which the stochastic solutions have a sparse decomposition based on their Karhunen-Loève (K-L) expansions. For $u(t,\boldsymbol{x},\omega) \in L^2([0,T]\times D\times\Omega)$, its K-L expansion reads as follows:

$$u(t,\boldsymbol{x},\omega) = \mathbb{E}[u] + \sum_{i=1}^{\infty} \sqrt{\lambda_i} A_i(\omega)\phi_i(t,\boldsymbol{x}), \tag{4.2.2}$$

where $\{\lambda_i\}$ and $\{\phi_i(t,\boldsymbol{x})\}$ are the eigenpairs of the covariance kernel $C(\boldsymbol{x},\mathbf{y})$, i.e. ,

$$\int_D C(\boldsymbol{x},\mathbf{y})\phi(\mathbf{y})d\mathbf{y} = \lambda\phi(\boldsymbol{x}), \tag{4.2.3}$$

and $\{A_i(\omega)\}$ are random variables defined as

$$A_i(\omega) = \frac{1}{\sqrt{\lambda_i}} \int_D (u(\boldsymbol{x}, \omega) - \mathbb{E}[u])\phi_i(\boldsymbol{x}) d\boldsymbol{x}. \tag{4.2.4}$$

Hereafter, the time t is compressed for the simplicity of notation. We will write functions depending on t explicitly wherever time t is important.

The mutually uncorrelated random variables $\{A_i(\omega)\}$ satisfy

$$\mathbb{E}[A_i] = 0, \quad \mathbb{E}[A_i A_j] = \delta_{ij}. \tag{4.2.5}$$

In numerical practice, only a finite series expansion is adopted, depending on the decay rate of the ordered eigenvalues $\{\lambda_i\}$,

$$u(\boldsymbol{x}, \omega) = \mathbb{E}[u] + \sum_{i=1}^{M} \sqrt{\lambda_i} A_i(\omega)\phi_i(\boldsymbol{x}). \tag{4.2.6}$$

Here, M is the number of gPC bases; the choice of M has a major impact on the accuracy of the statistics of the stochastic solutions.

For a given covariance function, the decay rate of the eigenvalues depends inversely on the correlation length. Long correlation length implies that the random process is strongly correlated and results in a fast decay of the eigenvalues. A weakly correlated process has short correlation length and results in a slow decay of the eigenvalues. Under some assumptions (Schwab & Todor, 2006), the eigenvalues in the K-L expansion decay exponentially (or sub-exponentially) fast in dimension $d = 1$ (or $d > 1$).

The DDSM algorithm consists of an offline part and an online part. In the offline part, an approximately complete subset of gPC bases $\{A_i(\omega)\}$, which are mutually orthonormal, are obtained from K-L expansions. In the online part, stochastic solutions are projected onto the subspace spanned by the gPC bases, and the coefficient functions in their K-L expansions are obtained by solving a coupled deterministic system. It should be noted that in this framework, the set of gPC bases are problem dependent.

4.2.1 Offline computation

The purpose of the offline computation is to obtain an approximately complete finite subset of gPC bases based on K-L expansion of the stochastic solutions. Various techniques can be employed to obtain an ensemble of stochastic solutions. In this part, we obtain not only the gPC bases $\{A_i(\omega)\}$ numerically, but also a variety of statistical information on the set of bases $\{A_i(\omega)\}$, such as their third moment

$$\mathbb{E}[A_i A_j A_k] = \frac{1}{N}\sum_{n=1}^{N} A_i(\omega_n)A_j(\omega_n)A_k(\omega_n).$$

Once the stochastic solution samples $u(\boldsymbol{x},\omega)$ are obtained, the mean and covariance are computed as follows:

$$\bar{u}(\boldsymbol{x}) = \frac{1}{N}\sum_{i=1}^{N} u(\boldsymbol{x},\omega_i), \tag{4.2.7}$$

$$C(\boldsymbol{x},\mathbf{y}) = \frac{1}{N}\sum_{i=1}^{N} u(\boldsymbol{x},\omega_i)u(\mathbf{y},\omega_i) - \bar{u}(\boldsymbol{x})\bar{u}(\mathbf{y}). \tag{4.2.8}$$

Afterwards, the first M eigen-pairs are obtained by solving

$$\lambda_i\phi_i(\boldsymbol{x}) = \int_D C(\boldsymbol{x},\mathbf{y})\phi_i(\mathbf{y})d\mathbf{y}, \quad i = 1,\cdots,M. \tag{4.2.9}$$

Finally, the gPC bases $\{A_i(\omega)\}$ are obtained by computing

$$A_i(\omega) = \frac{1}{\sqrt{\lambda_i}}\int_D \left(u(\boldsymbol{x},\omega) - \bar{u}(\boldsymbol{x})\right)\phi_i(\boldsymbol{x})d\boldsymbol{x}. \tag{4.2.10}$$

Remark 4.2.1. *It is easy to verify that each basis element $A_i(\omega)$ has mean zero and it is mutually orthogonal with $\{A_i(\omega)\}_{i=0}^{M}$.*

4.2.2 Online computation

In this part, only deterministic equations need to be solved since all the statistical information has been collected and stored in the offline part. This means that the online computation can be fast. The bases $\{A_i(\omega)\}$ span a finite-dimensional subspace

in $L^2(\Omega)$. The stochastic solution $u(t, \boldsymbol{x}, \omega)$ is projected onto this subspace, i.e. ,

$$u(t, \boldsymbol{x}, \omega) \approx \sum_{i=0}^{M} u_i(t, \boldsymbol{x}) A_i(\omega). \tag{4.2.11}$$

For simplicity of notation, we take $A_0 = 1$ and $u_0(t, \boldsymbol{x}) = \mathbb{E}[u(t, \boldsymbol{x}, \omega)]$.

In order to obtain the coupled deterministic equations, the Galerkin projection is utilized. Multiplying (4.2.1) by $A_j(\omega)$ and taking the expectation of both sides gives us

$$\begin{aligned}
&\sum_{i=0}^{M} \mathbb{E}\left[\mathcal{L}(t, \boldsymbol{x}, \omega) A_i(\omega) A_j(\omega)\right] u_i(t, \boldsymbol{x}) = \mathbb{E}\left[f(t, \boldsymbol{x}, \omega) A_j(\omega)\right], \\
&u_j(0, \boldsymbol{x}) = \mathbb{E}\left[u_0(\boldsymbol{x}, \omega) A_j(\omega)\right], \\
&\alpha u_j(t, \boldsymbol{x}) + \beta \partial_{\boldsymbol{x}} u_j(t, \boldsymbol{x}) = \mathbb{E}\left[u_{\partial D}(t, \boldsymbol{x}, \omega) A_j(\omega)\right], \quad \text{on boundary } \partial D,
\end{aligned} \tag{4.2.12}$$

for $j = 0, \cdots, M$.

This DDSM method has been extensively verified via solving elliptic PDE with random coefficients (Cheng *et al.*, 2011; Hu *et al.*, 2012).

4.3 DDSM for fully developed turbulence

The idea of DDSM can be extended to the simulations of fully developed turbulence. The nominal probabilistic dimensionality of turbulent variables, such as velocity $\boldsymbol{u}(t, \boldsymbol{x}, \omega)$ and pressure $p(t, \boldsymbol{x}, \omega)$, is prohibitively huge. Although nearly optimal gPC bases are chosen, the number of dominant terms in the K-L expansion remains prohibitively large and the resultant deterministic system includes too many unknowns. These lead to extraordinarily intensive computation, far greater even than that of DNS.

On the other hand, in fully developed turbulence, the series of time snapshots could be thought of as a stochastic process. Only statistical quantities over random space, time, and/or physical space are concerned, and only the core information (e.g. , drag and lift) are of interest to be extracted from the turbulent flows. Once some

variables have been averaged in the sense of sampling, time, and/or space, the size of the dominant gPC basis $\{A_i(\omega)\},\ i = 0, \cdots, M$, can become more tractable. Then, the turbulent variables can be projected onto the low-dimensional random subspace spanned by these gPC bases $\{A_i(\omega)\}$. For example, the velocity field $\boldsymbol{u}(t, \boldsymbol{x}, \omega)$ can be approximated as

$$\boldsymbol{u}(t, \boldsymbol{x}, \omega) \approx \sum_{i=0}^{M} \boldsymbol{u}_i(t, \boldsymbol{x}) A_i(\omega). \tag{4.3.1}$$

After plugging the expansion (4.3.1) into the Navier-Stokes equations and taking inner products with the gPC base elements $A_i(\omega)$, the following coupled system of equations for $\boldsymbol{u}_i(t, \boldsymbol{x})$ and $p_i(t, \boldsymbol{x})$ $(i = 0, \cdots, M)$ is obtained:

$$\begin{aligned} &\frac{\partial \boldsymbol{u}_i(t, \boldsymbol{x})}{\partial t} + \sum_{j=0}^{M} \sum_{k=0}^{M} \nabla \cdot (\boldsymbol{u}_j(t, \boldsymbol{x}) \boldsymbol{u}_k(t, \boldsymbol{x}) \mathbb{E}\left[A_i(\omega) A_j(\omega) A_k(\omega)\right] \\ &\qquad + \nabla p_i(t, \boldsymbol{x}) = \nu \Delta \boldsymbol{u}_i(t, \boldsymbol{x}), \end{aligned} \tag{4.3.2a}$$

$$\nabla \cdot \boldsymbol{u}_i(t, \boldsymbol{x}) = 0, \tag{4.3.2b}$$

$$\boldsymbol{u}_i(0, \boldsymbol{x}) = \mathbb{E}\left[\boldsymbol{u}_0(\boldsymbol{x}, \omega) A_i(\omega)\right]. \tag{4.3.2c}$$

Using the approximate gPC bases for the turbulent variables, the majority of statistical information can be accurately computed. This will be illustrated in great detail, using turbulent channel flow as an example, in the following.

4.3.1 Turbulent channel flow with random initial data

The computational settings are given in Section 3.1. Throughout this numerical demonstration, the nominal friction Reynolds number is chosen to be $Re_\tau = 180$. In order to obtain the statistical information of turbulent channel flow, a total of 100 runs of DNS have been computed to the point of entering into the fully developed turbulence regime.

Fully developed channel flow is completely specified by the density ρ, viscosity ν, half channel width δ, and mean axial pressure gradient $\mathrm{d}p_w/\mathrm{d}x$. The friction velocity

u_τ is given as

$$u_\tau = \left(-\frac{\delta}{\rho} \frac{\mathrm{d}p_w}{\mathrm{d}x} \right). \tag{4.3.3}$$

The definitions of wall-shear stress τ_w and subsequent u_τ are as follows:

$$\tau_w = \rho\nu \left(\frac{\mathrm{d}\langle u \rangle}{\mathrm{d}y} \right)_{y=0}, \quad u_\tau = \sqrt{\frac{\tau_w}{\rho}}, \tag{4.3.4}$$

where $\langle \cdot \rangle$ indicates an average over the x-z plane.

In the simulations, the mean axial pressure gradient normalized by density is 1, i.e. , $-\frac{1}{\rho}\mathrm{d}p_w/\mathrm{d}x = 1$ and the half channel width $\delta = 1$. Thus equation (4.3.3) gives $u_\tau = 1$. Accordingly, the friction Reynolds number can be calculated as follows:

$$Re_\tau = \frac{\delta u_\tau}{\nu} = \left(\frac{\mathrm{d}\langle u \rangle}{\mathrm{d}y} \right)_{y=0} \approx \frac{1}{2} \left(\left. \frac{\mathrm{d}\langle u \rangle}{\mathrm{d}y} \right|_{y=-1} - \left. \frac{\mathrm{d}\langle u \rangle}{\mathrm{d}y} \right|_{y=1} \right). \tag{4.3.5}$$

From the 100 realizations of turbulent channel flow, the mean of the friction Reynolds number is 179.0993, which matches excellently with the nominal friction Reynolds number $Re_\tau = 180$. The relative error is 0.005, which is far better than $1/\sqrt{N} = 0.1$. Moreover, the standard deviation is 2.3363.

Figure 4.1 shows the profile of the sampling mean of the velocity profile $u^+(y^+)$, which is averaged over the x-z plane and normalized by the wall-shear velocity u_τ. In the viscous sublayer $y^+ < 10$, excellent agreement with the linear relation $u^+ = y^+$ is observed. In the log-law region ($y^+ > 30$, $y/\delta < 0.3$), the profile matches the well-known logarithmic law of the wall $u^+ = \frac{1}{\kappa} \ln y^+ + B$ with $\kappa = 0.41$ and $B = 5.5$. The additive constant $B = 5.5$ is the approximate value reported in the literature (Eckelmann, 1974; Kim *et al.*, 1987; Spalart, 1988).

The variance of the velocity $u^+(y^+)$ is displayed in Figure 4.2. As indicated in Figure 4.2, the variance near the wall is tiny, less than 10^{-4}, which means that the sampling average of the mean velocity approaches the linear relation very closely, because of the relatively large viscous effect near the wall. Away from the wall, the variance is between 10^{-3} and 10^{-2}, which means that the fluctuation of the velocity $u^+(y^+)$ is relatively large. In addition, note that the velocity $u^+(y^+)$ is at least one

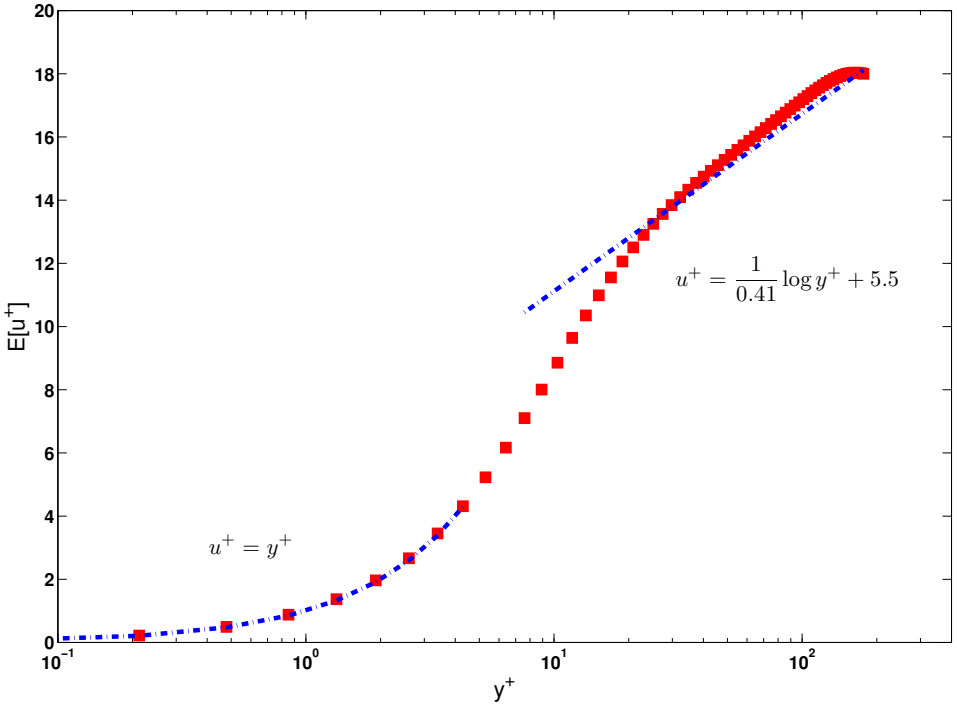

Figure 4.1: $\mathbb{E}[\bar{u}^+(y^+, \omega)]$ vs. y^+

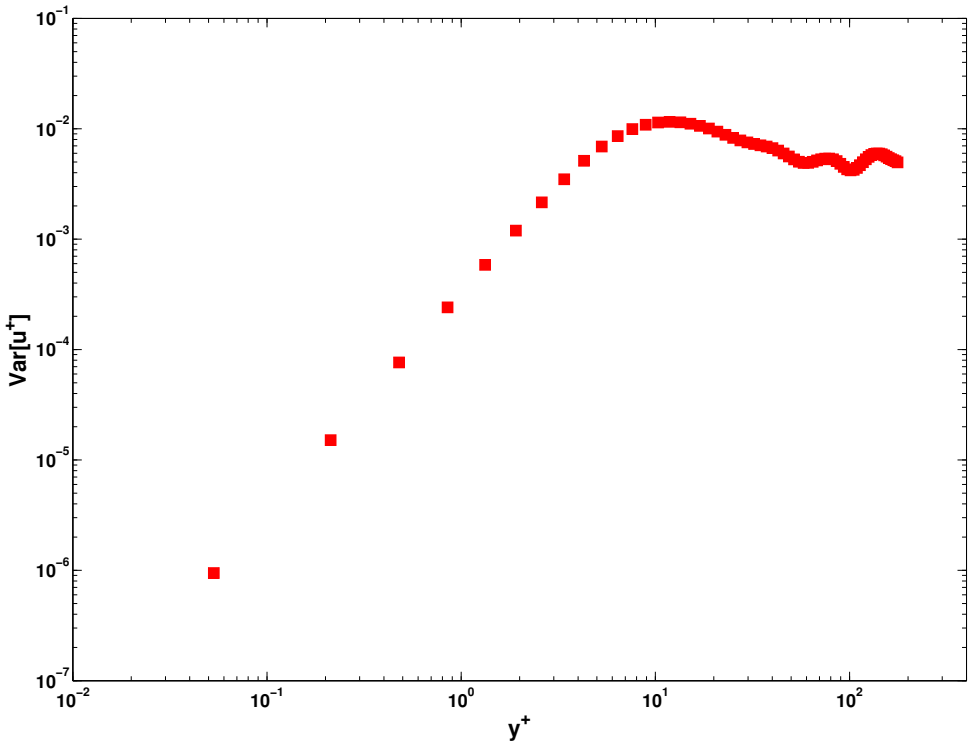

Figure 4.2: Var$[\bar{u}^+(y^+,\omega)]$ vs. y^+

order larger away from the wall than it is near the wall.

4.3.2 Optimal gPC bases for turbulent channel flow

Strictly speaking, the entire velocity field of turbulent channel flow should be utilized in order to obtain the gPC bases in equation (4.2.10). However, in this numerical simulation of turbulent channel flow with $Re_\tau = 180$, the effective number of grid points is $128 \times 129 \times 128 = 2,113,536$. Thus the covariance matrix is of size $2,113,536 \times 2,113,536$, which prevents us from computing the eigen-system of the covariance matrix.

In the numerical practice, the eigen-system can only be obtained for part of the velocity field. Figure 4.3 shows the eigen-value decay of the covariance matrices generated for velocities $u(t, \boldsymbol{x}, \omega)$, $v(t, \boldsymbol{x}, \omega)$, and $w(t, \boldsymbol{x}, \omega)$ in the box $[3.17, 4.16] \times [0.90, 0.99] \times [1.58, 2.08]$. Note that this box is close to the wall. If the ratio of eigen-values larger than 10^{-2} is desired, the corresponding number of gPC bases would be larger than 1200 for u and w and 900 for v. Moreover, near the central layer of the channel in the box $[3.17, 4.16] \times [0.20, 0.56] \times [1.58, 2.08]$, the decay of eigen-values for all the three velocity components u, v, and w is even slower, as indicated in Figure 4.4. The phenomena of slow eigen-value decay indicates that in the fully developed turbulent channel flow, the dimensionality in the probabilistic space remains huge.

Conceptually, a corresponding set of gPC bases could be obtained and velocities $u(t, \boldsymbol{x}, \omega)$, $v(t, \boldsymbol{x}, \omega)$, and $w(t, \boldsymbol{x}, \omega)$ could then be projected onto the subspace spanned by these gPC bases. However, it is noted that the number of the gPC bases could be more than 1000, which would lead to an immense system of coupled coefficient functions $u_i(t, \boldsymbol{x})$, $v_i(t, \boldsymbol{x})$ and $w_i(t, \boldsymbol{x})$ $(i = 0, \cdots, M)$. Although each equation for u_i, v_i, or w_i could be solved using a coarse grid, the total computational cost would greatly outweigh that of DNS.

Remark 4.3.1. *Since the turbulent flow is periodic in both the streamwise (x) and spanwise (z) directions, it is assumed that the flow is statistically homogeneous and isotropic in the streamwise and spanwise directions. On the other hand, the flow is anisotropic in the normal direction (y). Nevertheless, it can be checked that the gPC*

bases obtained using different layers in the normal direction are mutually expressible, i.e., the probabilistic space spanned by both sets of gPC bases is essentially the same.

4.3.3 A reduced set of gPC bases for turbulent channel flow

As mentioned in Section 4.3.2, the resultant system of equations for the coupled coefficient functions $u_i(t, \boldsymbol{x})$, $v_i(t, \boldsymbol{x})$, and $w_i(t, \boldsymbol{x})$ is computationally prohibitive since too many terms are involved. However, in most cases, only the statistical intensities of the turbulent flows are of interest. Therefore, it is possibly not necessary to calculate the gPC bases using the entirety of the velocity field. Instead, some statistical intensities, after averaging with respective to sampling, time, and/or space, could contain enough information about the fully developed turbulence. Thus, the gPC bases based on these statistical intensities are sufficient to represent the statistical quantities, which are of essential interest in theoretical analysis and/or engineering applications. In the following, we will demonstrate that the projection using a reduced set of gPC bases can retain most statistical information in the context of the turbulent channel flow.

The most prominent statistical characteristic of fully developed turbulent channel flow is the mean velocity profile. Fully developed channel flow is completely determined by ρ, ν, δ, and u_τ. Consequently the mean velocity profile $u(y)$ can be written (see Pope, 2000)

$$u(y) = u_\tau F_0 \left(\frac{y}{\delta}, Re_\tau \right), \tag{4.3.6}$$

where F_0 is a universal non-dimensional function to be determined.

Specifically, in the inner layer close to the wall ($y/\delta \ll 1$), the mean velocity obeys the law of the wall:

$$u^+(y^+) = y^+ + \mathcal{O}(y^{+2}). \tag{4.3.7}$$

At high Reynolds number, the outer part of the inner layer corresponds to large y^+.

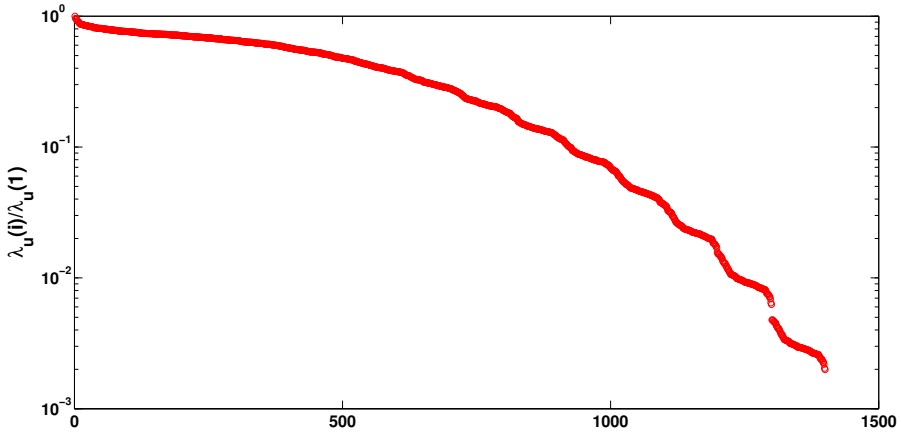

(a) Decay of eigen-values for u

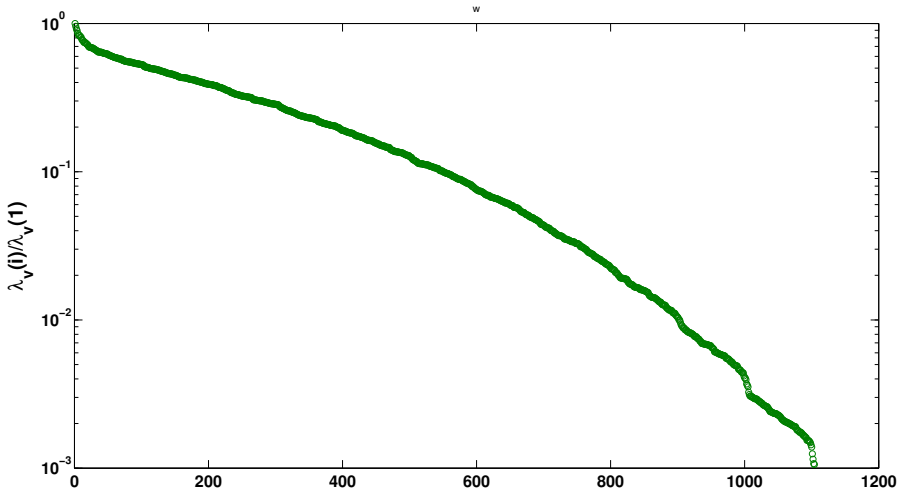

(b) Decay of eigen-values for v

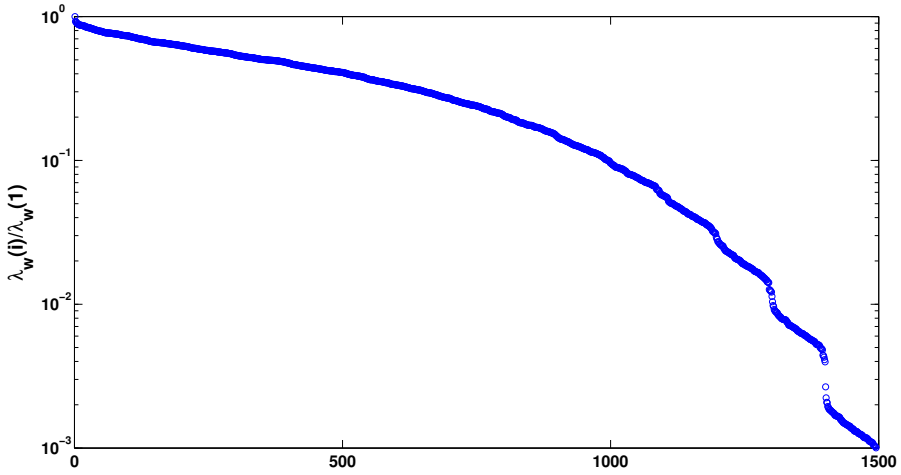

(c) Decay of eigen-values for w

Figure 4.3: Decay of eigen-values of covariance matrix in the box $[3.17, 4.16] \times [0.90, 0.99] \times [1.58, 2.08]$

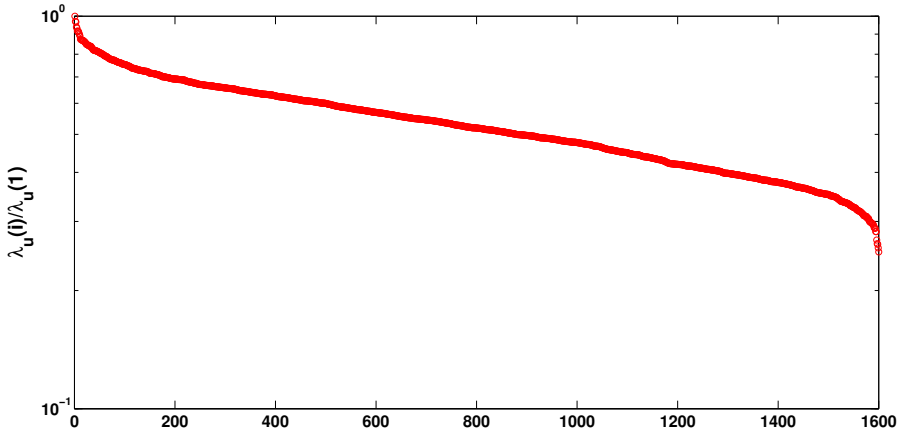

(a) Decay of eigen-values for u

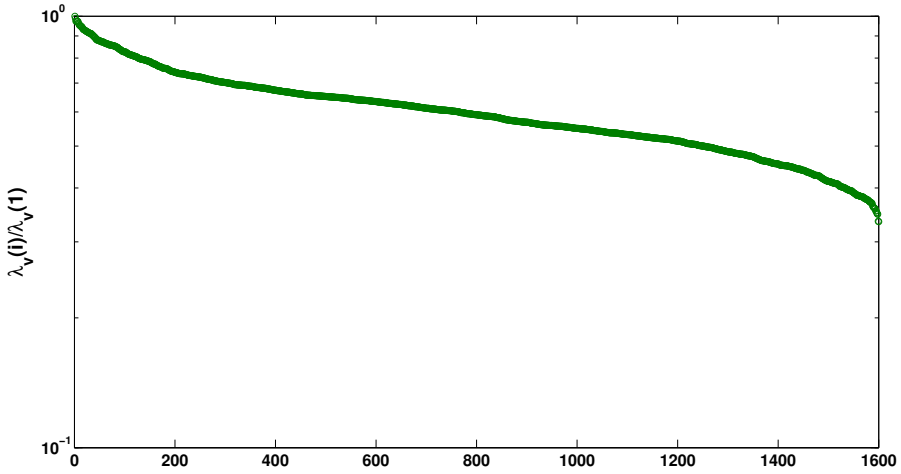

(b) Decay of eigen-values for v

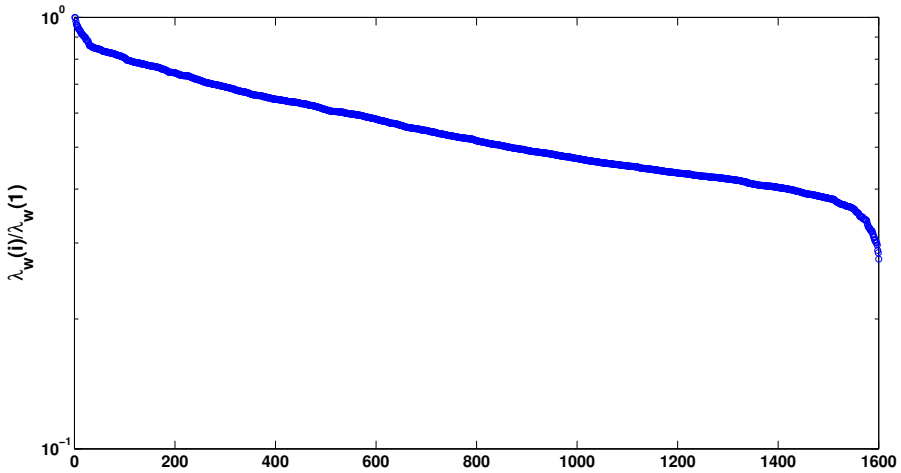

(c) Decay of eigen-values for w

Figure 4.4: Decay of eigen-values of covariance matrix in the box $[3.17, 4.16] \times [0.20, 0.56] \times [1.58, 2.08]$

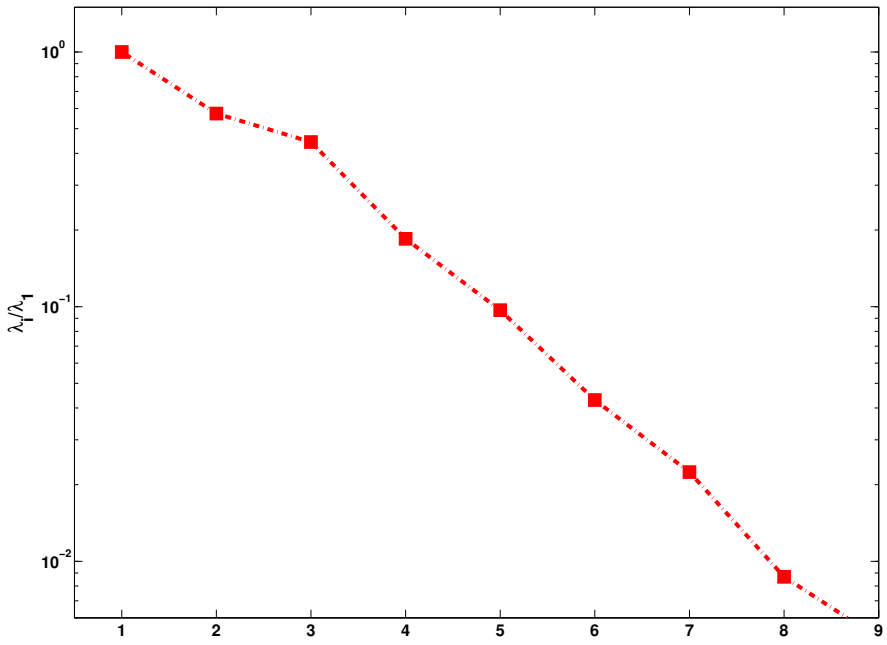

Figure 4.5: Decay of eigen-values based on the mean streamwise velocity $\bar{u}(y)$

The mean velocity satisfies the log-law in this region:

$$u^+ = \frac{1}{\kappa} \ln y^+ + B, \tag{4.3.8}$$

where κ is the von Kármán constant and $B \approx 5.5$ is an integration constant. Figure 4.1 shows the profile of the mean velocity $u^+(y^+)$ using 100 realizations of DNS executions.

Figure 4.5 shows the decay of the eigen-values of the covariance matrix based on the mean velocity profile $u^+(y^+)$. It is noted that after 8 eigenvalues, the ratio λ_i/λ_1 falls below 10^{-2}. This means that for the criterion $\lambda_i/\lambda_1 > 10^{-2}$, only 9 terms, including the mean term, in the expansion are sufficient. In other words, after averaging over the x-z plane, the probabilistic space is compressed significantly and the effective dimensionality is small enough that the coupled system becomes tractable.

Thus, the following data-driven algorithm is proposed for the simulation of turbulent flows.

Algorithm 4.3.2 (DDSM for the turbulent channel flow)**.**

(i) N realizations of DNS executions of fully developed turbulent channel flow are performed and the associated mean streamwise velocity profile $\bar{u}(y,\omega)$ in the wall-normal direction is obtained.

(ii) Use equation (4.2.8) *to obtain the covariance matrix $C(y,y')$, calculate the gPC bases $\{A_i(\omega)\}$ using equation* (4.2.10)*, and store them.*

(iii) Calculate and store statistical moments, $\mathbb{E}[A_i(\omega)A_j(\omega)A_k(\omega)]$.

(iv) Solve the system of equations (4.3.2) *to obtain the approximate velocity field $\boldsymbol{u}(t,\boldsymbol{x},\omega) = \sum_{i=0}^{M} \boldsymbol{u}_i(t,\boldsymbol{x})A_i(\omega)$ and pressure $p(t,\boldsymbol{x},\omega) = \sum_{i=0}^{M} p_i(t,\boldsymbol{x})A_i(\omega)$. Finally, calculate the statistical intensities of interest.*

Remark 4.3.3. *As mentioned earlier, the gPC bases are problem dependent. For different turbulent flows, different sets of gPC bases are required for accurate approximation. Also, statistical quantities other than the mean velocity profile can be used to generate the gPC bases.*

4.3.4 Numerical results

In this section, the numerical results using DDSM will be presented. Based on the analysis of eigen-value decay in Section 4.3.3, only 9 terms ($M = 8$) in the K-L expansion (4.3.1) are used in the approximation of $\boldsymbol{u}(t,\boldsymbol{x},\omega)$ in the numerical simulation. An effective grid of size $44(x) \times 45(y) \times 44(z)$ is used in the coupled system (4.3.2). The numerical procedure, which is described in detail in Section 3.1, needs slight revision to be applied to solve the system of equations (4.3.2). The time step $\Delta t = 0.001$ is used uniformly for all velocity components $\boldsymbol{u}_i(t,\boldsymbol{x})$, $i = 0, \cdots, M$ and a high-order Fourier smoothing method is implemented to remove dealiasing errors (see Hou & Li, 2007).

The calculated friction Reynolds number is 180.56, which is in excellent agreement with the nominal friction Reynolds number $Re_\tau = 180$. Figure 4.6 shows the comparison of the mean velocity profiles obtained by Monte Carlo DNS, the mean term in the K-L expansion and the full K-L expansion with $M = 8$. In the inner layer, all three results obey the linear relation perfectly. The discrepancy between

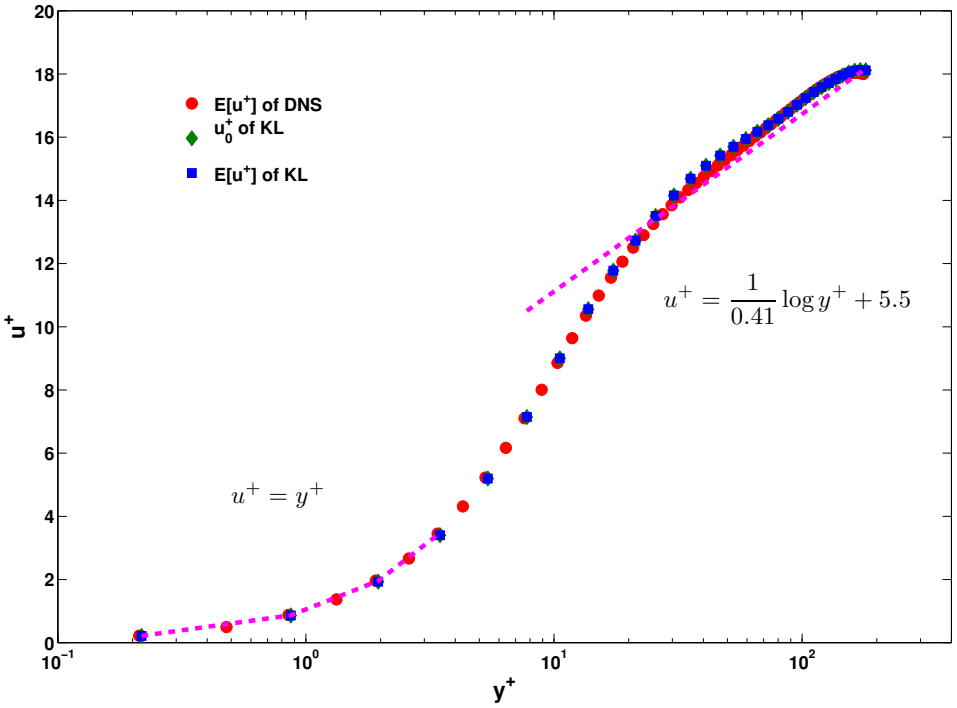

Figure 4.6: Mean profiles of u^+ as a function of y^+. $\circ$: Expectation of $u^+(y^+)$ by DNS; $\diamond$: $u_0^+(y^+)$, mean term in K-L expansion of u.; $\square$: Expectation of $u^+(y^+)$ by K-L expansion with $M = 8$

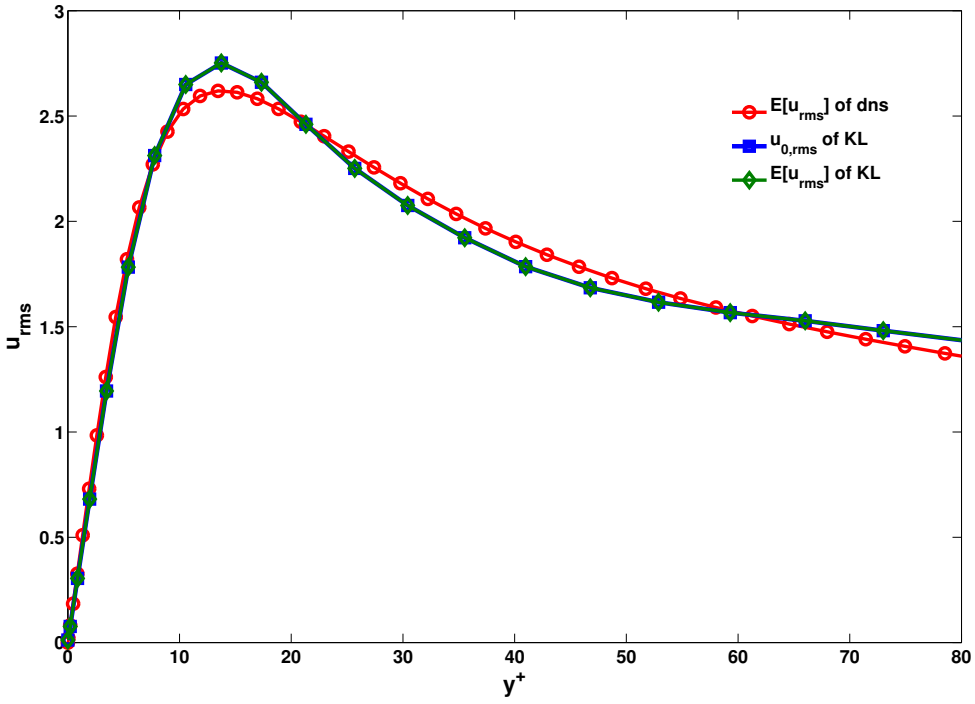

Figure 4.7: R.m.s. velocity fluctuation of $u(t, \boldsymbol{x}, \omega)$ normalized by the wall shear velocity u_τ. $\circ$: Expectation of $u_{\mathrm{rms}}(y^+)$ by DNS; $\diamond$: $u_{0,\mathrm{rms}}(y^+)$, mean term in K-L expansion of $u(t, \boldsymbol{x}, \omega)$; $\square$: Expectation of $u_{\mathrm{rms}}(y^+)$ by K-L expansion with $M = 8$

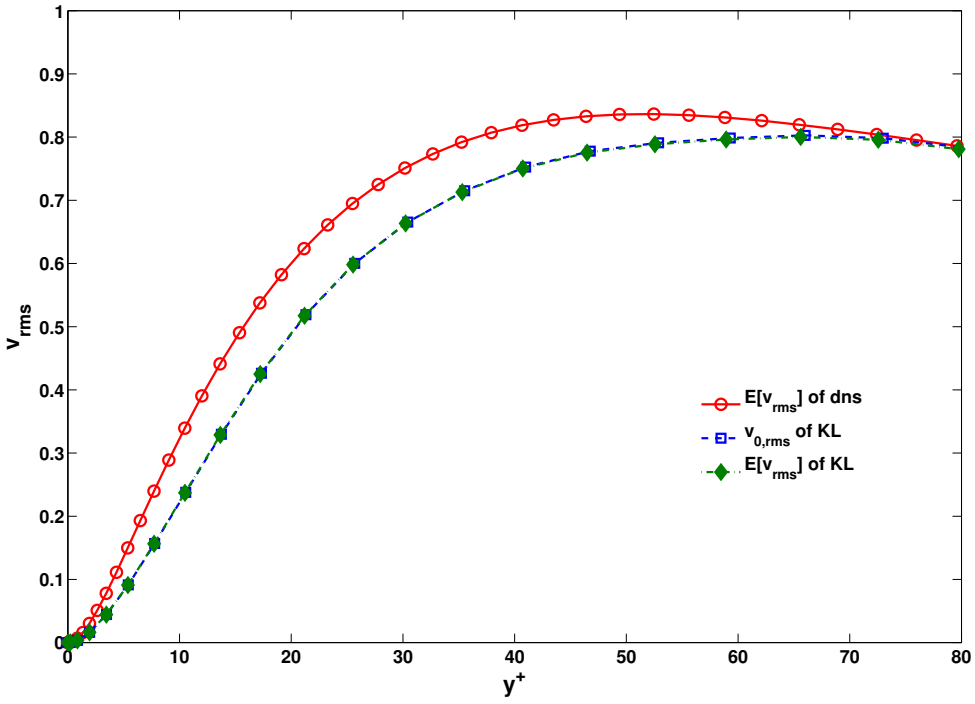

Figure 4.8: R.m.s. velocity fluctuation of $v(t, \boldsymbol{x}, \omega)$ normalized by the wall shear velocity u_τ. $\circ$: Expectation of $v_{\mathrm{rms}}(y^+)$ by DNS; $\diamond$: $v_{0,\mathrm{rms}}(y^+)$, mean term in K-L expansion of $v(t, \boldsymbol{x}, \omega)$; $\square$: Expectation of $v_{\mathrm{rms}}(y^+)$ by K-L expansion with $M = 8$

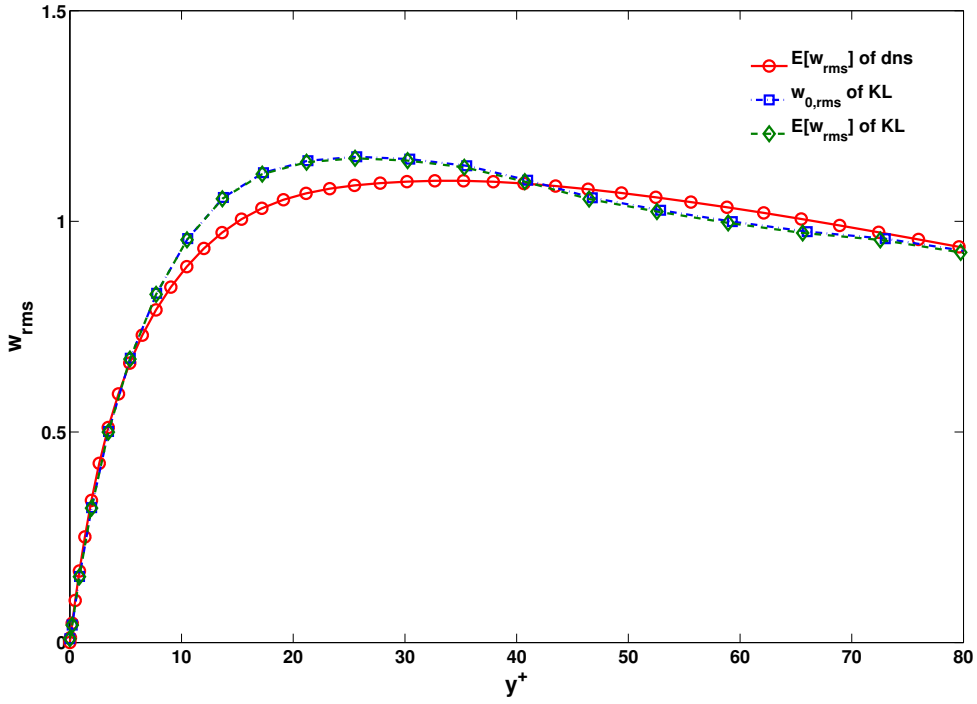

Figure 4.9: R.m.s. velocity fluctuation of $w(t, \boldsymbol{x}, \omega)$ normalized by the wall shear velocity u_τ. $\circ$: Expectation of $w_{\mathrm{rms}}(y^+)$ by DNS; $\diamond$: $w_{0,\mathrm{rms}}(y^+)$, mean term in K-L expansion of $w(t, \boldsymbol{x}, \omega)$; $\square$: Expectation of $w_{\mathrm{rms}}(y^+)$ by K-L expansion with $M = 8$

the Monte Carlo DNS and the DDSM is barely visible, while in the outer region, the Monte Carlo DNS approaches the log-law slightly better than the DDSM. The profile obtained from the data-driven method appears higher than that obtained from the Monte Carlo simulations.

The r.m.s. profiles normalized by the wall-shear velocity are shown in Figures 4.7-4.9 for $u(t, \boldsymbol{x}, \omega)$, $v(t, \boldsymbol{x}, \omega)$ and $w(t, \boldsymbol{x}, \omega)$, respectively. The peak value of the DDSM is noticeably higher for the r.m.s. profile of the streamwise velocity u. After around $y^+ = 20$, the profile of the data-driven method falls below that of Monte Carlo simulations. Moreover, the DDSM provides decent approximations to the r.m.s. profiles of the wall-normal velocity v and the spanwise velocity w as shown in Figures 4.8 and 4.9, respectively.

There might be two main reasons behind the discrepancy in r.m.s. velocity fluctuations between the DDSM and the MC simulations:

(i) Modeling error: the gPC bases $\{A_i(\omega)\}$ are obtained based on the statistical information of mean streamwise velocity. Accordingly, the DDSM yields better performance on the mean streamwise velocity profile (Figure 4.6) than the r.m.s. velocity fluctuation profiles (Figures 4.7-4.9).

(ii) Numerical error: the resolution of the DDSM might be the main reason of the discrepancy. As we discussed in Chapter 2, the near-wall vortex structure has to be resolved in order to capture the turbulence production mechanism. This means that if no wall model is used and not enough grid points are assigned near the wall, the model errors can lead to noticeable discrepancy in the r.m.s. velocity fluctuation.

The above issues will be addressed in Sections 4.3.5 and 4.3.6.

Remark 4.3.4. *It is interesting to notice that the mean term in the K-L expansion can capture most of the information of the statistical quantities, as shown in Figures 4.6-4.9. This is mainly due to the property of gPC bases* (4.2.5)*. In other words, the mean term in the K-L expansion* (4.3.1) *contains the majority of the statistical information on turbulent flows; the other terms can be regarded as stochastic fluctuations.*

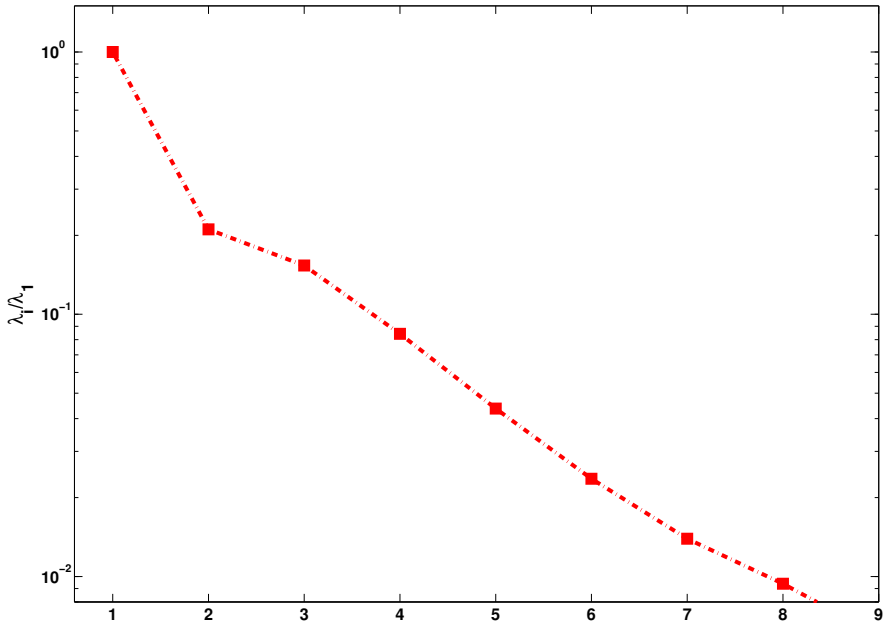

Figure 4.10: Decay of eigen-values based on r.m.s. streamwise velocity fluctuation u

4.3.5 Effects of different types of gPC bases

In Section 4.3.4, we see that the mean velocity profile obtained by the data-driven method with 8 gPC bases matches very well with the MC simulations. Note that the bases are calculated using the mean streamwise velocity of MC simulations. These gPC bases are then used to calculate the turbulence velocity field, which is used to compute the r.m.s. velocity fluctuations. However, the gPC bases are not necessarily obtained using the statistical information of the mean streamwise velocity.

Figure 4.10 shows the decay of sorted eigen-values based on the r.m.s. streamwise velocity fluctuation u. Clearly, the ratio of λ_i/λ_1 falls below 10^{-2} after 8 eigenmodes. The corresponding gPC bases can also be used for the expansion (4.3.1). We have examined the following three cases: (C1): only the first 8 bases $A_{m,i}$ calculated from the mean streamwise velocity u are used; (C2): only the first 8 bases $A_{r,i}$ calculated from the r.m.s. velocity fluctuation u are used; (C3): a set of hybrid bases combining the first 8 bases $A_{m,i}$ and the first 4 bases $A_{r,i}$ are used. In (C3), the bases $A_{m,i}$ and $A_{r,i}$ can be shown to be independent of each other and can be combined to form a

new larger set of bases using an orthogonalization technique like the Gram-Schmidt process. Note that beside these gPC bases, A_0, which is the mean term, is taken to be 1 for simplicity of notation.

Figures 4.11-4.13 show the profiles of r.m.s. fluctuations u, v, w, respectively. In the case of r.m.s. fluctuation u, C3 gives a slightly better profile than C1 and C2 when compared to MC samplings of DNS when $y^+ < 20$, while it performs worse for $30 < y^+ < 60$. There is not much difference using different bases with the same number of bases in C1 and C2. From Figure 4.12, it can be seen that using more bases in C3 does not improve the performance of r.m.s. fluctuation v. In contrast, in the region $10 < y^+ < 30$, C3 gives noticeably better approximation of the r.m.s. spanwise velocity fluctuation, as shown in Figure 4.13. Overall, different bases with the same number do not give distinguishable performance and a hybrid set with more bases, formed by combining different types of bases, does not improve the performance substantially.

4.3.6 Effects of numerical resolution

In this section, we examine the resolution effects of the velocity components $\boldsymbol{u}_i(t, \boldsymbol{x})$ in the coupled system (4.3.2), which may lead to noticeable difference in the r.m.s. velocity fluctuations, as shown in Figures 4.7-4.9. An effective grid of size $64(x) \times 65(y) \times 64(z)$ is used. This computation uses only 8 gPC bases from the mean velocity u. The r.m.s. velocity fluctuations u_{rms}, v_{rms} and w_{rms} are displayed in Figures 4.14-4.16, respectively. It can be seen that for the given resolution, the data-driven method gives very good performance when compared to MC simulations of DNS, especially for the r.m.s. velocity fluctuation v. The error bars (standard deviation) of the mean r.m.s. velocity fluctuations are also shown in these figures and the profiles calculated by the data-driven method fall inside the error bars for all three components. This demonstrates that resolution plays an essential role for the accuracy of the data-driven method in turbulent flows. It is sufficient to use 8 gPC bases and a resolution of $64(x) \times 65(y) \times 64(z)$ for channel flow for a moderate friction Reynolds number $Re_\tau = 180$.

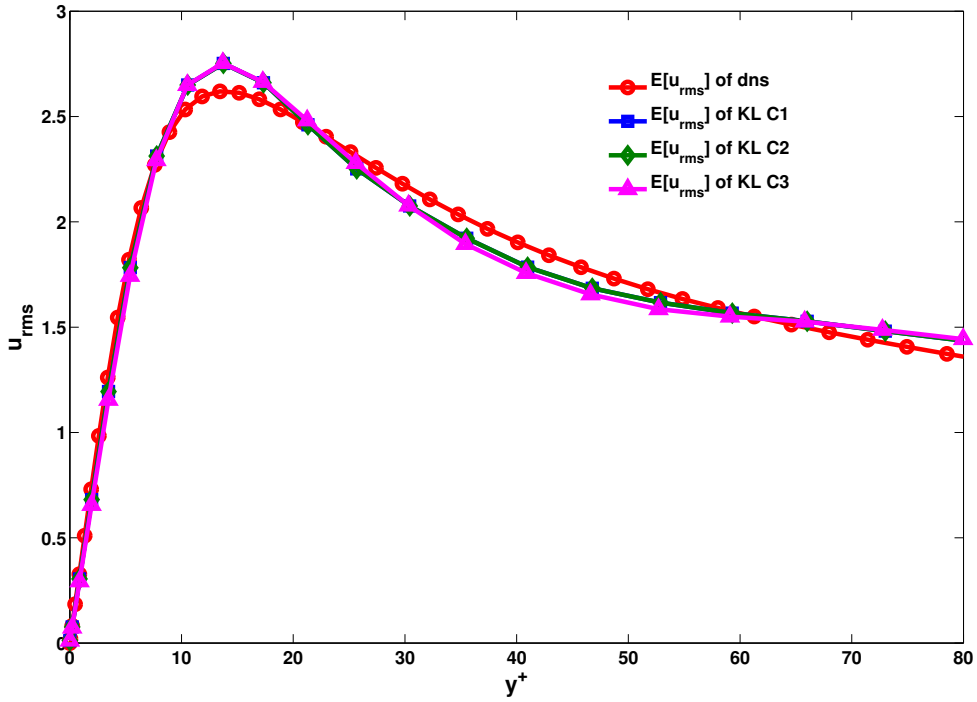

Figure 4.11: R.m.s. velocity fluctuation of $u(t, \boldsymbol{x}, \omega)$ normalized by the wall shear velocity u_τ. $\circ$: Expectation of $u_{\rm rms}(y^+)$ by DNS; $\square$: Expectation of $u_{\rm rms}(y^+)$ by K-L expansion of case C1; $\diamond$: Expectation of $u_{\rm rms}(y^+)$ by K-L expansion of case C2; $\triangle$: Expectation of $u_{\rm rms}(y^+)$ by K-L expansion of case C3

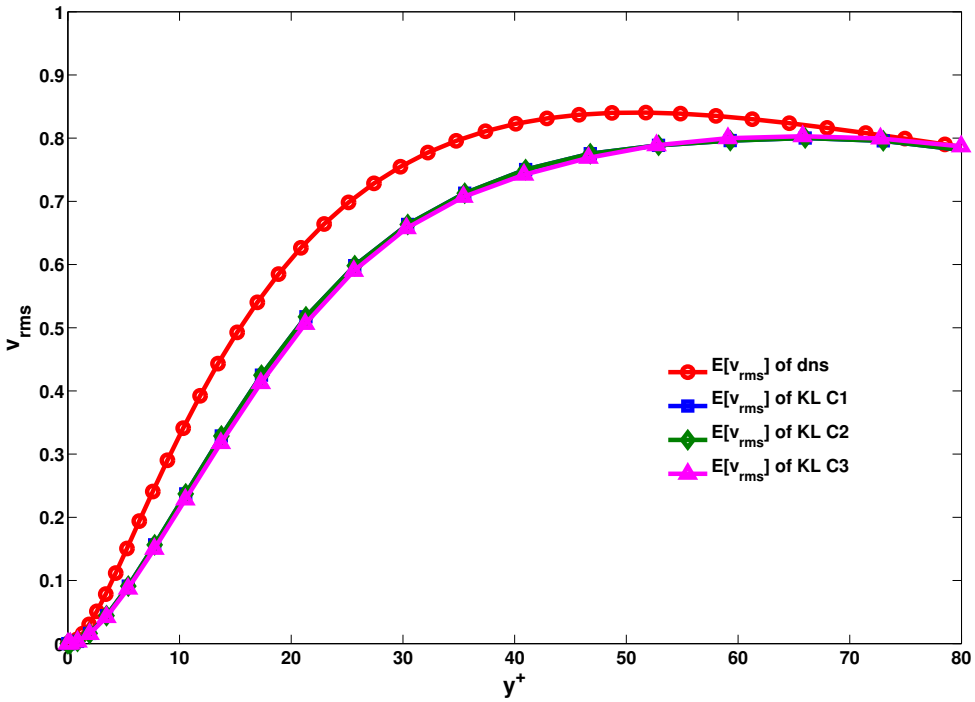

Figure 4.12: R.m.s. velocity fluctuation of $v(t, \boldsymbol{x}, \omega)$ normalized by the wall shear velocity u_τ. $\circ$: Expectation of $v_{\rm rms}(y^+)$ by DNS; $\square$: Expectation of $v_{\rm rms}(y^+)$ by K-L expansion of case C1; $\diamond$: Expectation of $v_{\rm rms}(y^+)$ by K-L expansion of case C2; $\triangle$: Expectation of $v_{\rm rms}(y^+)$ by K-L expansion of case C3

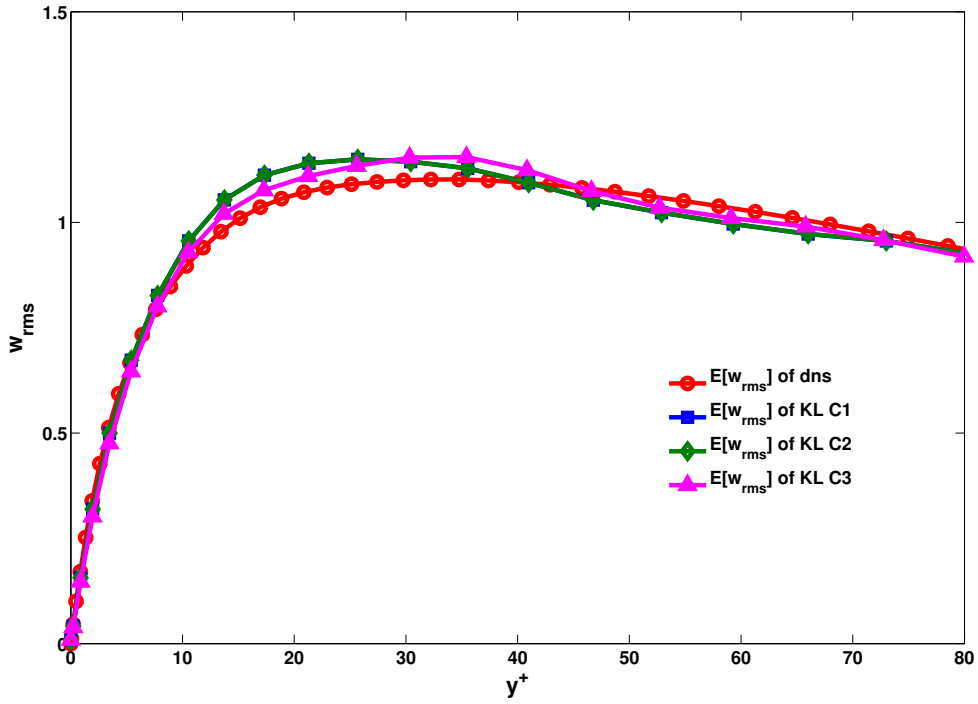

Figure 4.13: R.m.s. velocity fluctuation of $w(t, \boldsymbol{x}, \omega)$ normalized by the wall shear velocity u_τ. $\circ$: Expectation of $w_{\rm rms}(y^+)$ by DNS; $\square$: Expectation of $w_{\rm rms}(y^+)$ by K-L expansion of case C1; $\diamond$: Expectation of $w_{\rm rms}(y^+)$ by K-L expansion of case C2; $\triangle$: Expectation of $w_{\rm rms}(y^+)$ by K-L expansion of case C3

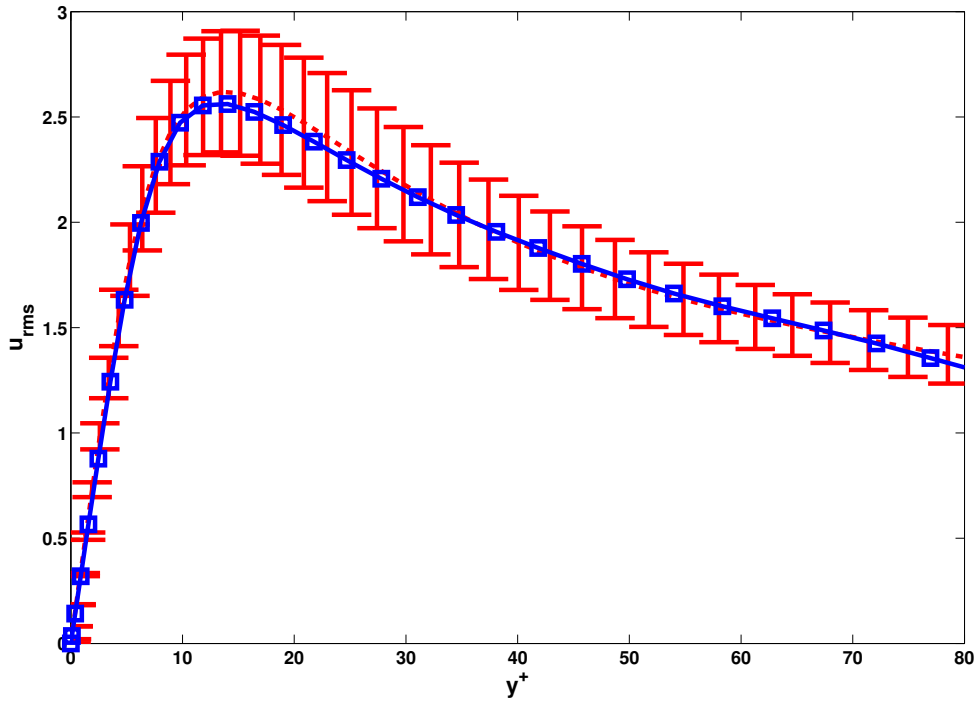

Figure 4.14: R.m.s. velocity fluctuation $u(t, \boldsymbol{x}, \omega)$ (solid line with $\square$) compared to MC of DNS (dashed line with error bars)

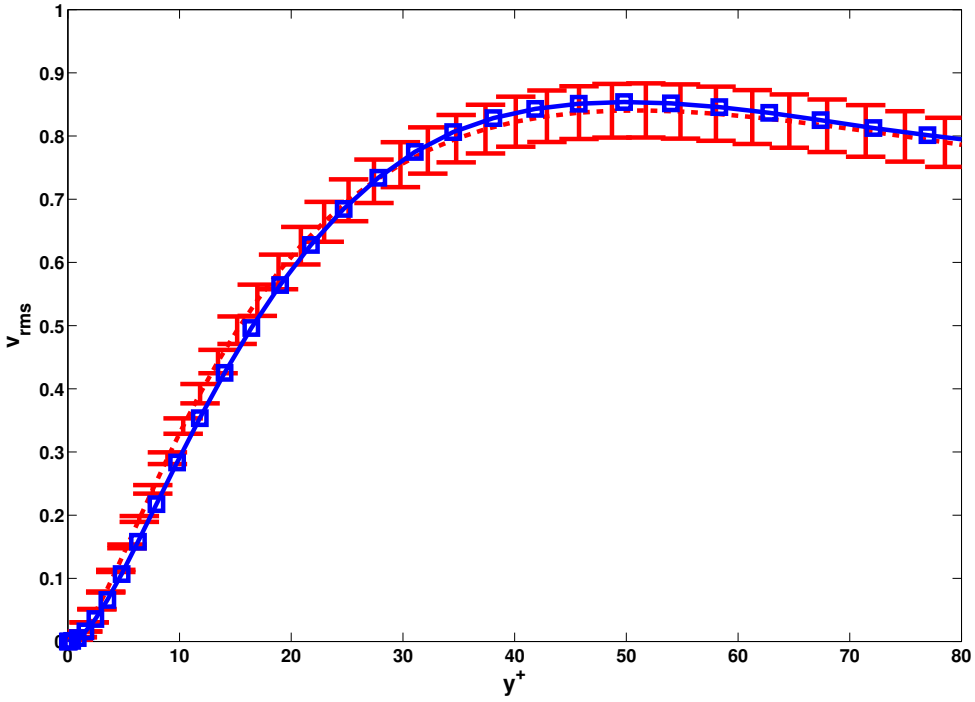

Figure 4.15: R.m.s. velocity fluctuation of $v(t, \boldsymbol{x}, \omega)$ (solid line with $\square$) compared to MC of DNS (dashed line with error bars)

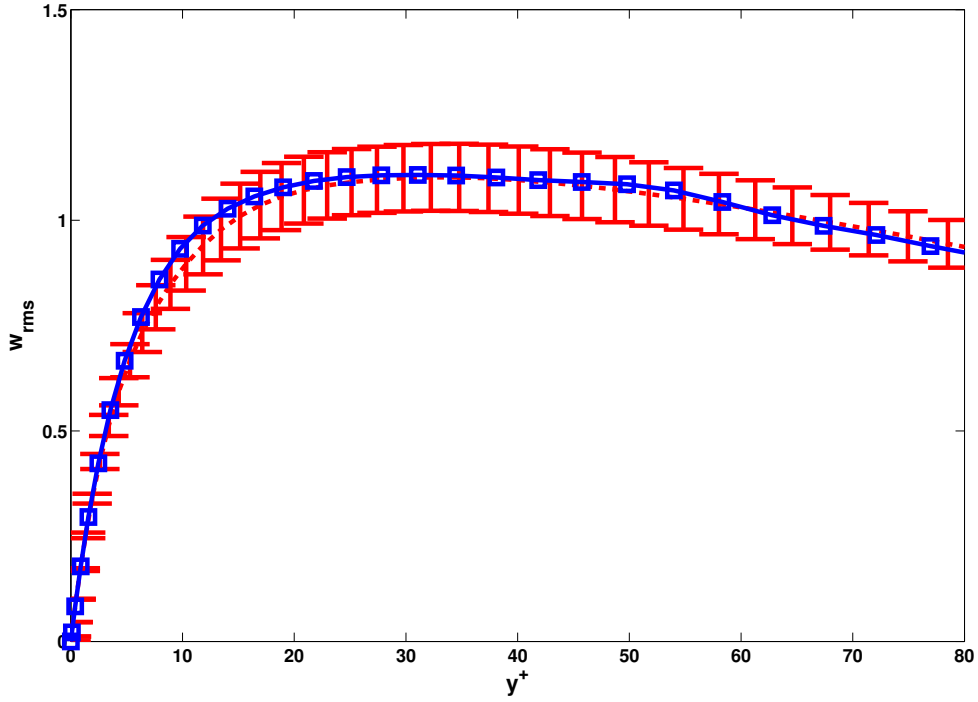

Figure 4.16: R.m.s. velocity fluctuation of $w(t, \boldsymbol{x}, \omega)$ (solid line with $\square$) compared to MC of DNS (dashed line with error bars)

4.4 Conclusion and discussion

In this chapter, turbulent flows are treated as stochastic processes. 100 Monte Carlo samples of DNS executions of the Navier-Stokes equations for the channel flow have been performed and applied to: (i) compute statistical quantities to compare with the results of the DDSM; (ii) compute a mean streamwise velocity profile $\bar{u}(y, \omega)$ that is used to calculate the gPC bases for the data-driven method. The gPC bases span a low-dimensional probabilistic subspace and a system of coupled equations can be solved numerically in this probabilistic subspace.

Once the gPC bases are obtained, the stochastic fluid variables $\boldsymbol{u}(t, \boldsymbol{x}, \omega)$ and $p(t, \boldsymbol{x}, \omega)$ are projected onto the subspace spanned by these gPC bases and the system of equations is solved to obtain approximate samples of $\boldsymbol{u}(t, \boldsymbol{x}, \omega)$ and $p(t, \boldsymbol{x}, \omega)$. Statistical quantities, such as the mean velocity profile and r.m.s. velocity fluctuations, are calculated and compared with the Monte Carlo simulations.

Two possible factors that determine the accuracy of the data-driven method have been carefully examined. The first is the number and the type of the gPC bases; the second is the numerical resolution of the velocity components $\boldsymbol{u}_i(t, \boldsymbol{x})$ in the coupled system (4.3.2). It turns out that the number and the type of gPC bases do not affect significantly the accuracy of the data-driven method. In contrast, choosing a sufficiently large resolution does improve the accuracy of the r.m.s. velocity fluctuations substantially.

Overall, the data-driven method offers decent approximation with low resolution $(64(x) \times 65(y) \times 64(z))$ and relatively small number of gPC bases ($M = 8$, in the case of turbulent channel flow). The same idea can be applied to other applications, such as flows through porous media, where the probabilistic dimensionality is huge as well and only the statistical quantities are of essential interest.

Chapter 5

Concluding remarks and discussion

In this thesis, we have approached multiscale modeling and computation of 3D incompressible turbulent flows from two different points of view. The first is the traditional view, where only low-frequency modes are calculated and the high-frequency fluctuations are modeled. Our multiscale analysis has been able to mathematically recover the Smagorinsky model for homogeneous turbulence and derive a simplified Smagorinsky model for turbulent channel flow with minimal assumptions. The second approach takes the stochastic viewpoint, where the turbulent flows are regarded as stochastic processes with random initial data. The turbulent velocities and pressure are projected onto the subspace spanned by orthonormal gPC bases. The approximate samples are obtained by solving a coupled system of equations for the velocity components in the K-L expansion.

In Chapter 2, we presented a new mathematical derivation of a closure relating the Reynolds stress to the mean strain rate for incompressible turbulent flows. This derivation is based on a multiscale analysis of the Navier-Stokes equations in three-dimensional space. By using a systematic multiscale analysis and an iterative homogenization of the large- and small-scale solutions dynamically, we identified a crucial structure of the Reynolds stress. As a consequence, we established a linear constitutive relationship between the Reynolds stress and the mean strain rate for the incompressible turbulent flows, up to the leading order of the time step. Further consideration of specific flows enabled us to produce an explicit formula for the Reynolds stress in two examples: homogeneous turbulence and turbulent channel flow. The Smagorinsky model for homogeneous turbulence has been recovered using this math-

ematical derivation. In addition, we have developed a simplified Smagorinsky model for turbulent channel flow.

To capture the backward energy cascade phenomena, a nonlinear LES model is introduced which uses a second order approximation of the inverse flow map function $\boldsymbol{\theta}$. Besides the dissipation effect in the first order, which is the Smagorinsky model, this nonlinear model captures the anti-cascade and dispersion effects. Our nonlinear model covers the mixed model that combines the Smagorinsky model and the gradient model. Furthermore, in contrast to the generic nonlinear model of Lund and Novikov, our nonlinear model captures the additional dispersive effect. On the other hand, a term missing in our model but present in the generic nonlinear model could be recaptured using a third order approximation in our derivation.

In Chapter 3, an extensive numerical study has been performed to validate the simplified model for the turbulent channel flow, using well-established benchmark tests at two Reynolds numbers, $Re_\tau = 180$ and $Re_\tau = 395$. Qualitative agreements have been shown for various statistical quantities of the channel flow. These include the mean streamwise velocity profiles, r.m.s. velocity and vorticity fluctuations, and the turbulent kinetic energy budget. However, we observed some noticeable differences among the results obtained from the simplified model, DNS, and experiments, especially in the profiles of r.m.s. vorticity fluctuations near the wall. We identified two main error sources that could contribute to these discrepancies. The first one is the measurement (hot wire) errors near the wall (Kim *et al.*, 1987). The second one is the modeling error. Additionally, error has been identified in the process of applying the asymptotic analysis, which is valid in the boundary layer, to the outer region of the channel flow.

Turbulent flows are treated as stochastic processes in Chapter 4. A data-driven stochastic method has been employed and tested for turbulent channel flow with random initial data. In the offline portion, 100 MC realizations of DNS were executed in order to calculate gPC bases for K-L expansions. The gPC bases were obtained using the mean streamwise velocity profile after averaging over the streamwise x and spanwise z directions, instead of the full velocity field. The basic idea is that in fully developed turbulence, only statistical quantities are of interest. The statistical infor-

mation has been highly compressed. If we only desire the statistics of the turbulent flow, it is feasible to use the already compressed information, such as mean velocities, r.m.s. velocity fluctuations, etc., to construct the gPC bases. In the online portion, the turbulent velocities and pressure are projected onto the subspace spanned by the gPC bases and a coupled system is solved to recover the velocity components in the K-L expansions. Preliminary numerical results show that decent approximations of turbulent statistics can be achieved with low resolution ($64(x) \times 65(y) \times 64(z)$) and a relatively small number of gPC bases ($M = 8$, in the case of turbulent channel flow).

Appendix A

Multiscale analysis of the Navier-Stokes equation

In this appendix, we develop a systematic multiscale analysis for the three-dimensional incompressible Navier-Stokes equations with multiscale initial data. This multiscale analysis sheds more light on the understanding of scale interactions for incompressible flows. Additionally, it provides an introduction to the approach of turbulence modeling illustrated in Chapter 2. More details can be found in Hou *et al.* (2005, 2008).

A.1 Derivation of the nested multiscale expansion

The original multiscale expansion is along the exact Lagrangian map. However, for convenience in engineering applications, large-scale solutions of the flows are represented in the Eulerian coordinates, while Lagrangian coordinates are used in the description of the small-scale solution propagation.

First, the nested multiscale expansion of $\boldsymbol{\theta}^\epsilon$ is obtained. The flow map $\boldsymbol{x}^\epsilon(t, \boldsymbol{\alpha})$ is defined as

$$\begin{aligned} \frac{\mathrm{d}\boldsymbol{x}^\epsilon}{\mathrm{d}t} &= \boldsymbol{u}^\epsilon(t, \boldsymbol{x}^\epsilon), \\ \boldsymbol{x}^\epsilon|_{t=0} &= \boldsymbol{\alpha}. \end{aligned} \tag{A.1.1}$$

Equation (A.1.1) states that each flow particle propagates along the Lagrangian map. It is obvious that $\boldsymbol{\theta}^\epsilon$ is the inverse of the flow map $\boldsymbol{x}^\epsilon$; it is therefore called the inverse

flow map. In 3D incompressible flows, the vorticity can be expressed in terms of the flow map as follows (Chorin & Marsden, 1993):

$$\boldsymbol{\omega}(t, \boldsymbol{x}^\epsilon(t, \boldsymbol{\alpha})) = D_{\boldsymbol{\alpha}} \boldsymbol{x}^\epsilon(t, \boldsymbol{\alpha}) \boldsymbol{\omega}_{\text{int}} \left(\boldsymbol{\alpha}, \frac{\boldsymbol{\alpha}}{\epsilon} \right). \tag{A.1.2}$$

Equation (A.1.2) indicates that the small-scale vorticity is essentially propagated along its flow map. The effect of vortex stretching is accounted for by the deformation of the Jacobian matrix of the flow map $D_{\boldsymbol{\alpha}} \boldsymbol{x}^\epsilon(t, \boldsymbol{\alpha})$.

Let $\boldsymbol{x} = \boldsymbol{x}^\epsilon(t, \boldsymbol{\alpha})$ and $\mathcal{A}^\epsilon = D_{\boldsymbol{x}} \boldsymbol{\theta}^\epsilon = (D_{\boldsymbol{\alpha}} \boldsymbol{x}^\epsilon)^{-1}$. Because of the incompressibility, the flow map $\boldsymbol{x}^\epsilon(t, \boldsymbol{\alpha})$ is volume-preserving, i.e. , $\det(D_{\boldsymbol{\alpha}} \boldsymbol{x}^\epsilon) = 1$. In addition, since $D_{\boldsymbol{\alpha}} \boldsymbol{x}^\epsilon D_{\boldsymbol{x}} \boldsymbol{\theta}^\epsilon = \mathcal{I}$, it follows that $\det(\mathcal{A}^\epsilon) = 1$.

Under the Lagrangian coordinate system, the stream function $\boldsymbol{\psi}$ and flow map $\boldsymbol{x}^\epsilon$ satisfy the following coupled equations:

$$-\nabla_\alpha \cdot (\mathcal{A}^\epsilon \mathcal{A}^{\epsilon T} \nabla_\alpha \boldsymbol{\psi}^\epsilon) = D_\alpha \boldsymbol{x}^\epsilon \boldsymbol{\omega}_{\text{int}} \left(\boldsymbol{\alpha}, \frac{\boldsymbol{\alpha}}{\epsilon} \right), \tag{A.1.3}$$

$$\frac{\partial \boldsymbol{x}^\epsilon}{\partial t} = \left(\nabla_{\boldsymbol{\alpha}} \times ((D_{\boldsymbol{\alpha}} \boldsymbol{x}^\epsilon)^T \boldsymbol{\psi}^\epsilon) \cdot \nabla_{\boldsymbol{\alpha}} \right) \boldsymbol{x}^\epsilon, \quad t > 0, \tag{A.1.4}$$

$$\boldsymbol{x}^\epsilon(0, \boldsymbol{\alpha}) = \boldsymbol{\alpha}.$$

Using the stream function-vorticity formulation in the Lagrangian system, the nonlinear convection can be treated exactly. The equations (A.1.3) and (A.1.4) are a nonlinear coupled system of the elliptic and transport equations. Now, it is clear that the multiscale periodic structure is convected by the full velocity field.

Based on the formulations (A.1.3) and (A.1.4), we seek multiscale expansions of the stream function and the flow map in the following form:

$$\boldsymbol{\psi}^\epsilon(t, \boldsymbol{\alpha}) = \bar{\boldsymbol{\psi}}(t, \boldsymbol{\alpha}, \tau) + \epsilon \tilde{\boldsymbol{\psi}}(t, \boldsymbol{\alpha}, \tau, \mathbf{y}), \tag{A.1.5}$$

$$\boldsymbol{x}^\epsilon(t, \boldsymbol{\alpha}) = \bar{\boldsymbol{x}}(t, \boldsymbol{\alpha}, \tau) + \epsilon \tilde{\boldsymbol{x}}(t, \boldsymbol{\alpha}, \tau, \mathbf{y}), \tag{A.1.6}$$

where $\tau = t/\epsilon$ and $\mathbf{y} = \boldsymbol{\alpha}/\epsilon$ with $\boldsymbol{\alpha} = \boldsymbol{\theta}^\epsilon$. We assume that $\tilde{\boldsymbol{\psi}}$ and $\tilde{\boldsymbol{x}}$ are periodic functions in $\mathbf{y}$ with zero mean.

Note that the expansions (A.1.5) and (A.1.6) are along the exact Lagrangian flow map for both slow and fast variables. For engineering applications, it is more conve-

nient to represent the macroscopic behavior of the flow in the Eulerian coordinate for the slow variables. Hence, we consider a new expansion where Eulerian coordinates are used for the slow variables, while the propagation of the fast variables is still described in Lagrangian coordinates. Let $\boldsymbol{\alpha} = \bar{\boldsymbol{\theta}}(t, \boldsymbol{x}, \tau)$ be the inverse flow map of $\boldsymbol{x} = \bar{\boldsymbol{x}}(t, \boldsymbol{\alpha}, \tau)$, i.e. , $\boldsymbol{x} = \bar{\boldsymbol{x}}(t, \bar{\boldsymbol{\theta}}(t, \boldsymbol{x}, \tau), \tau)$. Then we have

$$\bar{\boldsymbol{\theta}}(t, \boldsymbol{x}, \tau) = \bar{\boldsymbol{\theta}} \left(t, \bar{x}(t, \boldsymbol{\theta}^\epsilon, \tau) + \epsilon \tilde{\boldsymbol{x}} \left(t, \boldsymbol{\theta}^\epsilon, \frac{t}{\epsilon}, \frac{\boldsymbol{\theta}^\epsilon}{\epsilon} \right), \tau \right). \tag{A.1.7}$$

By expanding the above equation around $\epsilon = 0$ and using the identity $\boldsymbol{\theta}^\epsilon = \bar{\boldsymbol{\theta}}(t, \bar{\boldsymbol{x}}(t, \boldsymbol{\theta}^\epsilon, \tau), \tau)$, we obtain the following expansions for the inverse flow map $\boldsymbol{\theta}^\epsilon$:

$$\boldsymbol{\theta}^\epsilon = \bar{\boldsymbol{\theta}}(t, \boldsymbol{x}, \tau) + \epsilon \tilde{\boldsymbol{\theta}} \left(t, \bar{\boldsymbol{\theta}}, \tau, \frac{\boldsymbol{\theta}^\epsilon}{\epsilon} \right). \tag{A.1.8}$$

The stream function $\boldsymbol{\psi}^\epsilon$ can be expanded similarly.

A.2 A change of variable in small-scale quantities

The fast variable $\mathbf{y} = \boldsymbol{\theta}^\epsilon/\epsilon$ can introduce some technical difficulty in the numerical implementation. To simplify the computation of the cell problem, a change of variable from $\mathbf{y}$ to $\boldsymbol{z}$ can be done as follows:

$$\boldsymbol{z} = \mathbf{y} - \tilde{\boldsymbol{\theta}}(t, \bar{\boldsymbol{\theta}}, \tau, \mathbf{y}) \equiv \mathcal{G}(\mathbf{y}), \quad \mathbf{y} = \mathcal{G}^{-1}(\boldsymbol{z}). \tag{A.2.1}$$

Let $\hat{g} = g(\mathbf{y}) = g \circ \mathcal{G}^{-1}(\boldsymbol{z})$. Note that

$$\boldsymbol{z} + \mathbf{1} = \mathbf{y} + \mathbf{1} - \tilde{\boldsymbol{\theta}}(t, \bar{\boldsymbol{\theta}}, \tau, \mathbf{y} + \mathbf{1}), \tag{A.2.2}$$

where $\mathbf{1}$ is a unit vector. Therefore, it is easy to show that $\hat{g}$ is also a periodic function in $\boldsymbol{z}$. This implies that $\tilde{\boldsymbol{\theta}}$ can be rewritten as

$$\tilde{\boldsymbol{\theta}} = \hat{\tilde{\boldsymbol{\theta}}} \left(t, \bar{\boldsymbol{\theta}}, \tau, \frac{\bar{\boldsymbol{\theta}}}{\epsilon} \right). \tag{A.2.3}$$

To simplify the notation, we still denote $\hat{\tilde{\boldsymbol{\theta}}}$ by $\tilde{\boldsymbol{\theta}}$.

Finally, we expand the inverse flow map $\boldsymbol{\theta}^\epsilon$ and the stream function $\boldsymbol{\psi}^\epsilon$ as follows:

$$\boldsymbol{\theta}^\epsilon = \bar{\boldsymbol{\theta}}(t, \boldsymbol{x}, \tau) + \epsilon\tilde{\boldsymbol{\theta}}\left(t, \bar{\boldsymbol{\theta}}, \tau, \boldsymbol{z}\right), \tag{A.2.4}$$

$$\boldsymbol{\psi}^\epsilon = \bar{\boldsymbol{\psi}}(t, \boldsymbol{x}, \tau) + \epsilon\tilde{\boldsymbol{\psi}}\left(t, \bar{\boldsymbol{\theta}}, \tau, \boldsymbol{z}\right). \tag{A.2.5}$$

Then the expansion of velocity $\boldsymbol{u}^\epsilon$ can be calculated from the stream function:

$$\begin{aligned}\boldsymbol{u}^\epsilon &= \nabla_{\boldsymbol{x}} \times \boldsymbol{\psi}^\epsilon = \nabla_{\boldsymbol{x}} \times \left(\bar{\boldsymbol{\psi}}(t, \boldsymbol{x}, \tau) + \epsilon\tilde{\boldsymbol{\psi}}(t, \bar{\boldsymbol{\theta}}, \tau, \boldsymbol{z})\right) \\ &= \nabla_{\boldsymbol{x}} \times \bar{\boldsymbol{\psi}} + \epsilon\nabla_{\boldsymbol{x}} \times \tilde{\boldsymbol{\psi}} + \epsilon \cdot \frac{1}{\epsilon}(D_{\boldsymbol{x}}\bar{\boldsymbol{\theta}}^T\nabla_{\boldsymbol{z}}) \times \tilde{\boldsymbol{\psi}} \\ &= \bar{\boldsymbol{u}}(t, \boldsymbol{x}, \tau) + \tilde{\boldsymbol{u}}(t, \bar{\boldsymbol{\theta}}, \tau, \boldsymbol{z}),\end{aligned} \tag{A.2.6}$$

where $\bar{\boldsymbol{u}} = \nabla_{\boldsymbol{x}} \times \bar{\boldsymbol{\psi}}$ and $\tilde{\boldsymbol{u}} = (D_{\boldsymbol{x}}\bar{\boldsymbol{\theta}}^T\nabla_{\boldsymbol{z}}) \times \tilde{\boldsymbol{\psi}} + \epsilon\nabla_{\boldsymbol{x}} \times \tilde{\boldsymbol{\psi}}$.

A.3 Multiscale analysis of the 3D incompressible Navier-Stokes equations

Based on the understanding in the previous sections, we now perform a multiscale analysis of the 3D incompressible Navier-Stokes equations. We seek multiscale expansions for the velocity-pressure pair $(\boldsymbol{u}^\epsilon, p^\epsilon)$ in the form:

$$\boldsymbol{u}^\epsilon = \bar{\boldsymbol{u}}(t, \boldsymbol{x}, \tau) + \tilde{\boldsymbol{u}}(t, \boldsymbol{x}, \tau, \boldsymbol{z}), \tag{A.3.1}$$

$$p^\epsilon = \bar{p}(t, \boldsymbol{x}, \tau) + \tilde{p}(t, \boldsymbol{x}, \tau, \boldsymbol{z}). \tag{A.3.2}$$

Denoting $\bar{\partial}_t = \partial_t + \epsilon^{-1}\partial_\tau$ and substituting the expansions (A.2.4), (A.3.1), and (A.3.2) into the Navier-Stokes equations (2.1.1) and the equations of the inverse flow

map function (2.1.2), we have the following equations for the velocity:

$$\begin{aligned}
&\bar{\partial}_t \bar{\boldsymbol{u}} + \bar{\partial}_t \tilde{\boldsymbol{u}} + \frac{1}{\epsilon} D_{\boldsymbol{z}} \tilde{u} \bar{\partial}_t \bar{\boldsymbol{\theta}} \\
&+ \left(\nabla_{\boldsymbol{x}} + \frac{1}{\epsilon} D_{\boldsymbol{x}} \bar{\boldsymbol{\theta}}^T \nabla_{\boldsymbol{z}} \right) \cdot ((\bar{\boldsymbol{u}} + \tilde{\boldsymbol{u}}) \otimes (\bar{\boldsymbol{u}} + \tilde{\boldsymbol{u}})) \\
&+ \nabla_{\boldsymbol{x}} \bar{p} + \left(\nabla_{\boldsymbol{x}} + \frac{1}{\epsilon} D_{\boldsymbol{x}} \bar{\boldsymbol{\theta}}^T \nabla_{\boldsymbol{z}} \right) \tilde{p} \\
&- \nu \left(\nabla_{\boldsymbol{x}} + \frac{1}{\epsilon} D_{\boldsymbol{x}} \bar{\boldsymbol{\theta}}^T \nabla_{\boldsymbol{z}} \right) \cdot \left(\nabla_{\boldsymbol{x}} + \frac{1}{\epsilon} D_{\boldsymbol{x}} \bar{\boldsymbol{\theta}}^T \nabla_{\boldsymbol{z}} \right) (\bar{\boldsymbol{u}} + \tilde{\boldsymbol{u}}) = 0, \qquad \text{(A.3.3)} \\
&\left(\nabla_{\boldsymbol{x}} + \frac{1}{\epsilon} D_{\boldsymbol{x}} \bar{\boldsymbol{\theta}}^T \nabla_{\boldsymbol{z}} \right) \cdot (\bar{\boldsymbol{u}} + \tilde{\boldsymbol{u}}) = 0; \qquad \text{(A.3.4)}
\end{aligned}$$

and the inverse flow map:

$$\begin{aligned}
&\bar{\partial}_t \bar{\boldsymbol{\theta}} + \epsilon \partial_t \tilde{\boldsymbol{\theta}} + D_{\boldsymbol{z}} \tilde{\boldsymbol{\theta}} \bar{\partial}_t \bar{\boldsymbol{\theta}} + \epsilon \partial_t \tilde{\boldsymbol{\theta}} \\
&+ \left(\nabla_{\boldsymbol{x}} + \frac{1}{\epsilon} D_{\boldsymbol{x}} \bar{\boldsymbol{\theta}}^T \nabla_{\boldsymbol{z}} \right) \cdot \left((\bar{\boldsymbol{\theta}} + \epsilon \tilde{\boldsymbol{\theta}}) \otimes (\bar{\boldsymbol{u}} + \tilde{\boldsymbol{u}}) \right) = 0. \qquad \text{(A.3.5)}
\end{aligned}$$

A.3.1 Averaged equations

In this subsection, we derive the averaged equations for $\bar{\boldsymbol{u}}$ and $\bar{\boldsymbol{\theta}}$.

Averaging (A.3.3) and (A.3.4) with respect to $\boldsymbol{z}$ gives the following averaged equations for the large-scale velocity:

$$\begin{aligned}
\bar{\partial}_t \bar{\boldsymbol{u}} + \nabla_{\boldsymbol{x}} \cdot (\bar{\boldsymbol{u}} \otimes \bar{\boldsymbol{u}}) + \nabla_{\boldsymbol{x}} \cdot \langle \tilde{\boldsymbol{u}} \otimes \tilde{\boldsymbol{u}} \rangle_{\boldsymbol{z}} + \nabla_{\boldsymbol{x}} \bar{p} &= \nu \Delta_{\boldsymbol{x}} \bar{\boldsymbol{u}}, \qquad \text{(A.3.6)} \\
\nabla_{\boldsymbol{x}} \cdot \bar{\boldsymbol{u}} &= 0. \qquad \text{(A.3.7)}
\end{aligned}$$

Similarly, we have the following averaged equations for the inverse flow map after averaging over $\boldsymbol{z}$:

$$\bar{\partial}_t \bar{\boldsymbol{\theta}} + \nabla_{\boldsymbol{x}} \cdot \left(\bar{\boldsymbol{\theta}} \otimes \bar{\boldsymbol{u}} \right) + \epsilon \nabla_{\boldsymbol{x}} \cdot \langle \tilde{\boldsymbol{\theta}} \otimes \tilde{\boldsymbol{u}} \rangle_{\boldsymbol{z}} = 0. \qquad \text{(A.3.8)}$$

A.3.2 The cell problems

After deducting the averaged equations (A.3.6)-(A.3.8) from the full Navier-Stokes equation (2.1.1) and the equations of the inverse flow map (2.1.2), respectively, the

remaining parts are the equations for the small-scale velocity $\tilde{\boldsymbol{u}}$:

$$\begin{aligned}
&\partial_t \tilde{\boldsymbol{u}} + \nabla_{\boldsymbol{x}} \cdot (\bar{\boldsymbol{u}} \otimes \tilde{\boldsymbol{u}} + \tilde{\boldsymbol{u}} \otimes (\bar{\boldsymbol{u}} + \tilde{\boldsymbol{u}})) - \nabla_{\boldsymbol{x}} \cdot \langle \tilde{\boldsymbol{u}} \otimes \tilde{\boldsymbol{u}} \rangle + \nabla_{\boldsymbol{x}} \tilde{p} \\
&+ \frac{1}{\epsilon} \left(\partial_\tau \tilde{\boldsymbol{u}} + D_{\boldsymbol{z}} \tilde{\boldsymbol{u}} \bar{\partial}_t \bar{\boldsymbol{\theta}} + (D_{\boldsymbol{x}} \bar{\boldsymbol{\theta}}^T \nabla_{\boldsymbol{z}}) \cdot (\bar{\boldsymbol{u}} \otimes \tilde{\boldsymbol{u}} + \tilde{\boldsymbol{u}} \otimes \bar{\boldsymbol{u}} + \tilde{\boldsymbol{u}} \otimes \tilde{\boldsymbol{u}}) + D_{\boldsymbol{x}} \bar{\boldsymbol{\theta}}^T \nabla_{\boldsymbol{z}} \tilde{p} \right) \\
&- \frac{\nu}{\epsilon} \left(\nabla_{\boldsymbol{x}} \cdot (D_{\boldsymbol{x}} \bar{\boldsymbol{\theta}}^T \nabla_{\boldsymbol{z}} \tilde{\boldsymbol{u}}) + \nabla_{\boldsymbol{z}} \cdot (D_{\boldsymbol{x}} \bar{\boldsymbol{\theta}} \nabla_{\boldsymbol{x}} \tilde{\boldsymbol{u}}) \right) \\
&- \frac{\nu}{\epsilon^2} \nabla_{\boldsymbol{z}} \cdot (D_{\boldsymbol{x}} \bar{\boldsymbol{\theta}} D_{\boldsymbol{x}} \bar{\boldsymbol{\theta}}^T \nabla_{\boldsymbol{z}} \tilde{\boldsymbol{u}}) = 0, \qquad \text{(A.3.9)} \\
&(\epsilon \nabla_{\boldsymbol{x}} + D_{\boldsymbol{x}} \bar{\boldsymbol{\theta}}^T \nabla_{\boldsymbol{z}}) \cdot \tilde{\boldsymbol{u}} = 0, \qquad \text{(A.3.10)}
\end{aligned}$$

and the small scale inverse flow map $\tilde{\boldsymbol{\theta}}$:

$$\begin{aligned}
&\partial_\tau \tilde{\boldsymbol{\theta}} + D_{\boldsymbol{z}} \tilde{\boldsymbol{\theta}} \bar{\partial}_t \bar{\boldsymbol{\theta}} + \epsilon \partial_t \tilde{\boldsymbol{\theta}} \\
&+ \left(\nabla_{\boldsymbol{x}} + \frac{1}{\epsilon} D_{\boldsymbol{x}} \bar{\boldsymbol{\theta}}^T \nabla_{\boldsymbol{z}} \right) \cdot \left(\bar{\boldsymbol{\theta}} \otimes \tilde{\boldsymbol{u}} + \epsilon \tilde{\boldsymbol{\theta}} \otimes \bar{\boldsymbol{u}} + \epsilon \tilde{\boldsymbol{\theta}} \otimes \tilde{\boldsymbol{u}} \right) \\
&- \epsilon \nabla_{\boldsymbol{x}} \cdot \langle \tilde{\boldsymbol{\theta}} \otimes \tilde{\boldsymbol{u}} \rangle = 0. \qquad \text{(A.3.11)}
\end{aligned}$$

In the following, we will try to simplify equations (A.3.9)-(A.3.11) as much as possible.

It is easy to see that the incompressibility condition (A.3.10) becomes

$$(\epsilon \nabla_{\boldsymbol{x}} + D_{\boldsymbol{x}} \boldsymbol{\theta}^T \nabla_{\boldsymbol{z}}) \cdot \tilde{\boldsymbol{u}} = 0. \qquad \text{(A.3.12)}$$

Multiplying by ϵ, the equation for $\tilde{\boldsymbol{u}}$ (A.3.9) can be rewritten as

$$\begin{aligned}
&\partial_\tau \tilde{\boldsymbol{u}} + D_{\boldsymbol{z}} \tilde{\boldsymbol{u}} \bar{\partial}_t \bar{\boldsymbol{\theta}} + (D_{\boldsymbol{x}} \bar{\boldsymbol{\theta}}^T \nabla_{\boldsymbol{z}}) \cdot (\bar{\boldsymbol{u}} \otimes \tilde{\boldsymbol{u}} + \tilde{\boldsymbol{u}} \otimes \bar{\boldsymbol{u}} + \tilde{\boldsymbol{u}} \otimes \tilde{\boldsymbol{u}}) + D_{\boldsymbol{x}} \bar{\boldsymbol{\theta}}^T \nabla_{\boldsymbol{z}} \tilde{p} \\
&= \frac{\nu}{\epsilon} \nabla_{\boldsymbol{z}} \cdot \left(D_{\boldsymbol{x}} \bar{\boldsymbol{\theta}} D_{\boldsymbol{x}} \bar{\boldsymbol{\theta}}^T \nabla_{\boldsymbol{z}} \tilde{\boldsymbol{u}} \right) \\
&+ \nu \left[\nabla_{\boldsymbol{x}} \cdot (D_{\boldsymbol{x}} \bar{\boldsymbol{\theta}}^T \nabla_{\boldsymbol{z}} \tilde{\boldsymbol{u}}) + \nabla_{\boldsymbol{z}} \cdot (D_{\boldsymbol{x}} \bar{\boldsymbol{\theta}} \nabla_{\boldsymbol{x}} \tilde{\boldsymbol{u}}) \right] \\
&- \epsilon \left[\partial_t \tilde{\boldsymbol{u}} + \nabla_{\boldsymbol{x}} \cdot (\bar{\boldsymbol{u}} \otimes \tilde{\boldsymbol{u}} + \tilde{\boldsymbol{u}} \otimes (\bar{\boldsymbol{u}} + \tilde{\boldsymbol{u}})) - \nabla_{\boldsymbol{x}} \cdot \langle \tilde{\boldsymbol{u}} \otimes \tilde{\boldsymbol{u}} \rangle + \nabla_{\boldsymbol{x}} \tilde{p} \right]. \qquad \text{(A.3.13)}
\end{aligned}$$

Neglecting the $\mathcal{O}(\epsilon)$ terms, (A.3.13) becomes

$$\begin{aligned}
&\partial_\tau \tilde{\boldsymbol{u}} + D_{\boldsymbol{z}}\tilde{\boldsymbol{u}}\bar{\partial}_t\bar{\boldsymbol{\theta}} + (D_{\boldsymbol{x}}\bar{\boldsymbol{\theta}}^T\nabla_{\boldsymbol{z}})\cdot(\bar{\boldsymbol{u}}\otimes\tilde{\boldsymbol{u}} + \tilde{\boldsymbol{u}}\otimes\bar{\boldsymbol{u}} + \tilde{\boldsymbol{u}}\otimes\tilde{\boldsymbol{u}}) + D_{\boldsymbol{x}}\bar{\boldsymbol{\theta}}^T\nabla_{\boldsymbol{z}}\tilde{p} \\
=&\frac{\nu}{\epsilon}\nabla_{\boldsymbol{z}}\cdot\left(D_{\boldsymbol{x}}\bar{\boldsymbol{\theta}}D_{\boldsymbol{x}}\bar{\boldsymbol{\theta}}^T\nabla_{\boldsymbol{z}}\cdot\tilde{\boldsymbol{u}}\right) \\
&+\nu\left[\nabla_{\boldsymbol{x}}\cdot(D_{\boldsymbol{x}}\bar{\boldsymbol{\theta}}^T\nabla_{\boldsymbol{z}}\tilde{\boldsymbol{u}}) + \nabla_{\boldsymbol{z}}\cdot(D_{\boldsymbol{x}}\bar{\boldsymbol{\theta}}\nabla_{\boldsymbol{x}}\tilde{\boldsymbol{u}})\right].
\end{aligned} \tag{A.3.14}$$

Note that by using (A.3.8),

$$\begin{aligned}
&D_{\boldsymbol{z}}\tilde{\boldsymbol{u}}\bar{\partial}_t\bar{\boldsymbol{\theta}} + D_{\boldsymbol{z}}\tilde{\boldsymbol{u}}D_{\boldsymbol{x}}\bar{\boldsymbol{\theta}}(\bar{\boldsymbol{u}}+\tilde{\boldsymbol{u}}) \\
&= D_{\boldsymbol{z}}\tilde{\boldsymbol{u}}(\bar{\partial}_t\bar{\boldsymbol{\theta}} + D_{\boldsymbol{x}}\bar{\boldsymbol{\theta}}\bar{\boldsymbol{u}}) + D_{\boldsymbol{z}}\tilde{\boldsymbol{u}}D_{\boldsymbol{x}}\bar{\boldsymbol{\theta}}\tilde{\boldsymbol{u}} \\
&= D_{\boldsymbol{z}}\tilde{\boldsymbol{u}}D_{\boldsymbol{x}}\bar{\boldsymbol{\theta}}\tilde{\boldsymbol{u}} - \epsilon D_{\boldsymbol{z}}\tilde{\boldsymbol{u}}(\nabla_{\boldsymbol{x}}\cdot\langle\tilde{\boldsymbol{\theta}}\otimes\tilde{\boldsymbol{u}}\rangle) \quad \text{by equation (A.3.8)} \\
&= \mathcal{O}(\epsilon) \quad \text{by (A.3.12).}
\end{aligned}$$

Thus, to the leading order approximation in terms of ϵ, we have

$$\begin{aligned}
&\partial_\tau\tilde{\boldsymbol{u}} + D_{\boldsymbol{z}}\tilde{\boldsymbol{u}}D_{\boldsymbol{x}}\bar{\boldsymbol{\theta}}\tilde{\boldsymbol{u}} + D_{\boldsymbol{x}}\bar{\boldsymbol{\theta}}^T\nabla_{\boldsymbol{z}}\tilde{p} \\
=&\frac{\nu}{\epsilon}\left(\nabla_{\boldsymbol{z}}\cdot\left(D_{\boldsymbol{x}}\bar{\boldsymbol{\theta}}D_{\boldsymbol{x}}\bar{\boldsymbol{\theta}}^T\nabla_{\boldsymbol{z}}\cdot\tilde{\boldsymbol{u}}\right)\right. \\
&\left.+\,\epsilon(\nabla_{\boldsymbol{x}}\cdot(D_{\boldsymbol{x}}\bar{\boldsymbol{\theta}}^T\nabla_{\boldsymbol{z}}\tilde{\boldsymbol{u}}) + \nabla_{\boldsymbol{z}}\cdot(D_{\boldsymbol{x}}\bar{\boldsymbol{\theta}}\nabla_{\boldsymbol{x}}\tilde{\boldsymbol{u}}))\right) + \mathcal{O}(\epsilon).
\end{aligned} \tag{A.3.15}$$

Further, subtracting the averaged equations of $\bar{\boldsymbol{\theta}}$ (A.3.8) from the full equation of $\bar{\boldsymbol{\theta}}^\epsilon$ (2.1.2) leads to the following equation for $\tilde{\boldsymbol{\theta}}$:

$$\begin{aligned}
&\partial_\tau\tilde{\boldsymbol{\theta}} + D_{\boldsymbol{z}}\tilde{\boldsymbol{\theta}}\bar{\partial}_t\bar{\boldsymbol{\theta}} + \epsilon\partial_t\tilde{\boldsymbol{\theta}} \\
&+\left(\nabla_{\boldsymbol{x}} + \frac{1}{\epsilon}D_{\boldsymbol{x}}\bar{\boldsymbol{\theta}}^T\nabla_{\boldsymbol{z}}\right)\left(\bar{\boldsymbol{\theta}}\otimes\tilde{\boldsymbol{u}} + \epsilon\tilde{\boldsymbol{\theta}}\otimes\bar{\boldsymbol{u}} + \epsilon\tilde{\boldsymbol{\theta}}\otimes\tilde{\boldsymbol{u}}\right) \\
&-\epsilon\nabla_{\boldsymbol{x}}\cdot\langle\tilde{\boldsymbol{\theta}}\otimes\tilde{\boldsymbol{u}}\rangle = 0,
\end{aligned}$$

or to the first order in ϵ,

$$\begin{aligned}
&\partial_\tau\tilde{\boldsymbol{\theta}} + D_{\boldsymbol{z}}\tilde{\boldsymbol{\theta}}\bar{\partial}_t\bar{\boldsymbol{\theta}} + \nabla_{\boldsymbol{x}}\cdot(\bar{\boldsymbol{\theta}}\otimes\tilde{\boldsymbol{u}}) \\
&+\frac{1}{\epsilon}(D_{\boldsymbol{x}}\bar{\boldsymbol{\theta}}^T\nabla_{\boldsymbol{z}})\cdot(\bar{\boldsymbol{\theta}}\otimes\tilde{\boldsymbol{u}}) + (D_{\boldsymbol{x}}\bar{\boldsymbol{\theta}}^T\nabla_{\boldsymbol{z}})\cdot(\tilde{\boldsymbol{\theta}}\otimes(\bar{\boldsymbol{u}}+\tilde{\boldsymbol{u}})) + \mathcal{O}(\epsilon) = 0.
\end{aligned} \tag{A.3.16}$$

We then calculate each term in the above equation (A.3.16):

$$\begin{aligned} I &:= D_{\boldsymbol{z}}\tilde{\boldsymbol{\theta}}\bar{\partial}_t\bar{\boldsymbol{\theta}} \\ &= D_{\boldsymbol{z}}\tilde{\boldsymbol{\theta}}(-\nabla_{\boldsymbol{x}}\cdot(\bar{\boldsymbol{\theta}}\otimes\bar{\boldsymbol{u}})), \quad \text{from (A.3.8)} \\ &= -(D_{\boldsymbol{z}}\tilde{\boldsymbol{\theta}})\cdot\left((\bar{\boldsymbol{u}}\cdot\nabla_{\boldsymbol{x}})\bar{\boldsymbol{\theta}}\right) \quad \text{or} \quad -\left(D_{\boldsymbol{z}}\tilde{\boldsymbol{\theta}}D_{\boldsymbol{x}}\bar{\boldsymbol{\theta}}\bar{\boldsymbol{u}}\right); \end{aligned} \tag{A.3.17}$$

$$\begin{aligned} II &:= \nabla_{\boldsymbol{x}}\cdot(\bar{\boldsymbol{\theta}}\otimes\tilde{\boldsymbol{u}}) \\ &= (\tilde{\boldsymbol{u}}\cdot\nabla_{\boldsymbol{x}})\bar{\boldsymbol{\theta}} + \bar{\boldsymbol{\theta}}(\nabla_{\boldsymbol{x}}\cdot\tilde{\boldsymbol{u}}) \quad \text{or} \quad (D_{\boldsymbol{x}}\bar{\boldsymbol{\theta}})\cdot\tilde{\boldsymbol{u}} + \bar{\boldsymbol{\theta}}(\nabla_{\boldsymbol{x}}\cdot\tilde{\boldsymbol{u}}); \end{aligned} \tag{A.3.18}$$

$$\begin{aligned} III &:= \frac{1}{\epsilon}(D_{\boldsymbol{x}}\bar{\boldsymbol{\theta}}^T\nabla_{\boldsymbol{z}})\cdot(\bar{\boldsymbol{\theta}}\otimes\tilde{\boldsymbol{u}}) \\ &= \frac{1}{\epsilon}\bar{\boldsymbol{\theta}}((D_{\boldsymbol{x}}\bar{\boldsymbol{\theta}}^T\nabla_{\boldsymbol{z}})\cdot\tilde{\boldsymbol{u}}) \\ &= \frac{1}{\epsilon}(-\epsilon\nabla_{\boldsymbol{x}}\cdot\tilde{\boldsymbol{u}} \quad \text{by (A.3.12)} \\ &= -\bar{\boldsymbol{\theta}}(\nabla_{\boldsymbol{x}}\cdot\tilde{\boldsymbol{u}}); \quad \text{and} \end{aligned} \tag{A.3.19}$$

$$\begin{aligned} IV &:= (D_{\boldsymbol{x}}\bar{\boldsymbol{\theta}}^T\nabla_{\boldsymbol{z}})\cdot(\tilde{\boldsymbol{\theta}}\otimes(\bar{\boldsymbol{u}}+\tilde{\boldsymbol{u}})) \\ &= D_{\boldsymbol{z}}\tilde{\boldsymbol{\theta}}\cdot D_{\boldsymbol{x}}\bar{\boldsymbol{\theta}}\cdot(\bar{\boldsymbol{u}}+\tilde{\boldsymbol{u}}) + (((D_{\boldsymbol{x}}\bar{\boldsymbol{\theta}})^T\nabla_{\boldsymbol{z}})\cdot\tilde{\boldsymbol{u}})\tilde{\boldsymbol{\theta}} \\ &= D_{\boldsymbol{z}}\tilde{\boldsymbol{\theta}}\cdot D_{\boldsymbol{x}}\bar{\boldsymbol{\theta}}\cdot\bar{\boldsymbol{u}} + D_{\boldsymbol{z}}\tilde{\boldsymbol{\theta}}\cdot D_{\boldsymbol{x}}\bar{\boldsymbol{\theta}}\tilde{\boldsymbol{u}} - \epsilon(\nabla_{\boldsymbol{x}}\cdot\tilde{\boldsymbol{u}})\tilde{\boldsymbol{\theta}}. \end{aligned} \tag{A.3.20}$$

The sum of the above equalities is

$$I + II + III + IV = D_{\boldsymbol{x}}\bar{\boldsymbol{\theta}}\tilde{\boldsymbol{u}} + D_{\boldsymbol{z}}\tilde{\boldsymbol{\theta}}D_{\boldsymbol{x}}\bar{\boldsymbol{\theta}}\tilde{\boldsymbol{u}} - \epsilon(\nabla_{\boldsymbol{x}}\cdot\tilde{\boldsymbol{u}})\tilde{\boldsymbol{\theta}}. \tag{A.3.21}$$

Therefore, up to the first order in ϵ, (A.3.16) states that

$$\partial_\tau\tilde{\boldsymbol{\theta}} + D_{\boldsymbol{z}}\tilde{\boldsymbol{\theta}}D_{\boldsymbol{x}}\bar{\boldsymbol{\theta}}\tilde{\boldsymbol{u}} + D_{\boldsymbol{z}}\bar{\boldsymbol{\theta}}\tilde{\boldsymbol{u}} = 0. \tag{A.3.22}$$

A.3.3 A simplified multiscale system

In the numerical implementation, the large-scale solutions $\bar{\boldsymbol{u}}$, $\bar{p}$, and $\bar{\boldsymbol{\theta}}$ still depend on the fast time τ. In order to obtain a multiscale system for the large-scale solutions that is independent of τ, a local time-average is performed to eliminate the dependence of the mean velocity field and inverse flow map on the fast time τ. Then the large-scale solutions have the form

$$\bar{\boldsymbol{u}}(t,\boldsymbol{x},\tau) = \boldsymbol{u}(t,\boldsymbol{x}) + \epsilon \boldsymbol{u}_1(t,\boldsymbol{x},\tau), \tag{A.3.23}$$

$$\bar{p}(t,\boldsymbol{x},\tau) = p(t,\boldsymbol{x}) + \epsilon p_1(t,\boldsymbol{x},\tau), \tag{A.3.24}$$

$$\bar{\boldsymbol{\theta}}(t,\boldsymbol{x},\tau) = \boldsymbol{\theta}(t,\boldsymbol{x}) + \epsilon \boldsymbol{\theta}_1(t,\boldsymbol{x},\tau). \tag{A.3.25}$$

In addition, the multiscale system can be simplified further by studying only the leading-order terms of $(\tilde{\boldsymbol{u}}, \tilde{p})$ and $\tilde{\boldsymbol{\theta}}$:

$$\tilde{\boldsymbol{u}} = \boldsymbol{w}(t,\bar{\boldsymbol{\theta}},\tau,\boldsymbol{z}) + \mathcal{O}(\epsilon), \tag{A.3.26}$$

$$\tilde{p} = q(t,\bar{\boldsymbol{\theta}},\tau,\boldsymbol{z}) + \mathcal{O}(\epsilon), \tag{A.3.27}$$

$$\tilde{\boldsymbol{\theta}} = \boldsymbol{\Theta}(t,\bar{\boldsymbol{\theta}},\tau,\boldsymbol{z}) + \mathcal{O}(\epsilon). \tag{A.3.28}$$

Then we obtain the equations for the large-scale solutions (2.1.11) that are accurate up to the first order of ϵ:

$$\partial_t \boldsymbol{u} + (\boldsymbol{u}\cdot\nabla_{\boldsymbol{x}})\boldsymbol{u} + \nabla_x p + \nabla\cdot\langle[\boldsymbol{w}\otimes\boldsymbol{w}]^*_\Delta\rangle = \nu\Delta\boldsymbol{u}, \tag{A.3.29}$$

$$\nabla_{\boldsymbol{x}}\cdot\boldsymbol{u} = 0 \tag{A.3.30}$$

for the large-scale velocity and

$$\partial_t\boldsymbol{\theta} + (u\cdot\nabla_{\boldsymbol{x}})\boldsymbol{\theta} + \epsilon\nabla\cdot\langle[\boldsymbol{\Theta}\otimes\boldsymbol{w}]^*_\Delta\rangle = \mathbf{0} \tag{A.3.31}$$

for the large-scale inverse flow map.

Also, the leading order equations of the small-scale solutions (2.1.12) are derived:

$$\partial_\tau \boldsymbol{w} + D_{\boldsymbol{z}}\boldsymbol{w} D_{\boldsymbol{x}}\bar{\boldsymbol{\theta}}\boldsymbol{w} + D_{\boldsymbol{x}}\bar{\boldsymbol{\theta}}^T \nabla_{\boldsymbol{z}} q - \frac{\nu}{\epsilon}\nabla \cdot (D_{\boldsymbol{x}}\bar{\boldsymbol{\theta}} D_{\boldsymbol{x}}\bar{\boldsymbol{\theta}}^T \nabla_{\boldsymbol{z}}\boldsymbol{w}) = \mathbf{0},$$
$$(D_x \bar{\boldsymbol{\theta}}^T \nabla_{\boldsymbol{z}}) \cdot \boldsymbol{w} = \mathbf{0},$$

for the small-scale velocity and

$$\partial_\tau \boldsymbol{\Theta} + (\mathcal{I} + D_{\boldsymbol{z}}\boldsymbol{\Theta}) D_{\boldsymbol{x}}\bar{\boldsymbol{\theta}}\boldsymbol{w} = \mathbf{0} \tag{A.3.32}$$

for the small-scale inverse flow map.

Appendix B

Reparameterization of the initial velocity in a two-scale structure

In this appendix, we show how to reformulate any velocity $\boldsymbol{v}(x, y, z)$, which may contain infinitely many scales, into a two-scale structure. Assume $\boldsymbol{v}$ is periodic in x and z. The no-slip boundary condition is applied in the y direction. Since this procedure can be done direction by direction, we can reparameterize in the periodic direction x and z; this has been shown in Hou *et al.* (2005, 2008). Thus, we only need to deal with the non-periodic direction y. The key idea is to use the sine transform, which not only has the same computational complexity of Fourier transform, but also incorporates the boundary condition.

Let $\boldsymbol{v}(x, y, z)$ be any function which is periodic in (x, z) and is zero on the boundaries in y, i.e. , $\boldsymbol{v}(x, 0, z) = \boldsymbol{v}(x, 1, z) = 0$. Denoting $\boldsymbol{x} = (x, y, z)$ and $\boldsymbol{k} = (k_x, k_y, k_z)$, the Fourier transform in the x and z directions and the sine transform in the y direction read as

$$\boldsymbol{v}(x, y, z) = \sum_{\boldsymbol{k}=(k_x,k_y,k_z)} \hat{\boldsymbol{v}}_k \sin(\pi k_y y) \exp(2\pi i(k_x x + k_z z)).$$

Choose $0 < \epsilon = 1/E < 1$, where E is an integer, and let

$$\Lambda_E = \left\{ \boldsymbol{k}; |k_j| \leq \frac{E}{2}, j = (x, y, z) \right\}, \quad \Lambda'_E = Z^3 \backslash \Lambda_E. \tag{B.0.1}$$

Then by splitting into two parts in spectral space, the velocity can be rewritten as

$$\boldsymbol{v} = \boldsymbol{v}^{(l)}(\boldsymbol{x}) + \boldsymbol{v}^{(s)}(\boldsymbol{x}, \boldsymbol{x}/\epsilon), \tag{B.0.2}$$

where

$$\boldsymbol{z} = \boldsymbol{x}/\epsilon = (x/\epsilon, y/\epsilon, z/\epsilon).$$

The two terms in (B.0.2) are the large-scale velocity and the small-scale velocity, respectively:

$$\boldsymbol{v}^{(l)}(\boldsymbol{x}) = \sum_{\boldsymbol{k}\in\Lambda_E} \hat{\boldsymbol{v}}(\boldsymbol{k}) \sin(\pi k_y y) \exp(2\pi i(k_x x + k_z z)),$$
$$\boldsymbol{v}^{(s)}(\boldsymbol{x}, \boldsymbol{y}) = \sum_{\boldsymbol{k}\in\Lambda'_E} \hat{\boldsymbol{v}}(\boldsymbol{k}) \sin(\pi k_y y) \exp(2\pi i(k_x x + k_z z)).$$

Rewrite each $\boldsymbol{k}$ in the following form

$$\boldsymbol{k} = E\boldsymbol{k}^{(s)} + \boldsymbol{k}^{(l)},$$

where

$$\boldsymbol{k}^{(s)} = (k_x^{(s)}, k_y^{(s)}, k_z^{(s)}), \quad \boldsymbol{k}^{(l)} = (k_x^{(l)}, k_y^{(l)}, k_z^{(l)}),$$

then we have

$$
\begin{aligned}
v^{(s)} &= \sum_{\boldsymbol{k}\in\Lambda'_E} \hat{\boldsymbol{v}}(\boldsymbol{k}) \sin\left(\pi k_y y\right) \exp\left(2\pi i(k_x x + k_z z)\right) \\
&= \sum_{E\boldsymbol{k}^{(s)}+\boldsymbol{k}^{(l)}\in\Lambda'_E} \hat{\boldsymbol{v}}(E\boldsymbol{k}^{(s)} + \boldsymbol{k}^{(l)}) \sin\left(\pi(Ek_y^{(s)} + k_y^{(l)})y\right) \\
&\times \exp\left(2\pi i((Ek_x^{(s)} + k_x^{(l)})x + (Ek_z^{(s)} + k_z^{(l)})z)\right) \\
&= \sum_{\boldsymbol{k}^{(s)}\neq 0} \left(\sum_{\boldsymbol{k}^{(l)}\in\Lambda_E} \hat{\boldsymbol{v}}(E\boldsymbol{k}^{(s)} + \boldsymbol{k}^{(l)}) \sin\left(\pi k_y^{(l)} y\right) \exp\left(2\pi i(k_x^{(l)} x + k_z^{(l)} z)\right) \right) \\
&\qquad \times \cos\left(\pi k_y^{(s)}(Ey)\right) \exp\left(2\pi i(k_x^{(s)} Ex + k_z^{(s)} Ez)\right) \\
&+ \sum_{\boldsymbol{k}^{(s)}\neq 0} \left(\sum_{\boldsymbol{k}^{(l)}\in\Lambda_E} \hat{\boldsymbol{v}}(E\boldsymbol{k}^{(s)} + \boldsymbol{k}^{(l)}) \cos\left(\pi k_y^{(l)} y\right) \exp\left(2\pi i(k_x^{(l)} x + k_z^{(l)} z)\right) \right) \\
&\qquad \times \sin\left(\pi k_y^{(s)}(Ey)\right) \exp\left(2\pi i(k_x^{(s)} Ex + k_z^{(s)} Ez)\right) \\
&= \sum_{\boldsymbol{k}^{(s)}\neq 0} \left(\hat{\boldsymbol{v}}_1(\boldsymbol{k}^{(s)}, \boldsymbol{x}) \cos\left(\pi k_y^{(s)}(y/\epsilon)\right) + \hat{\boldsymbol{v}}_2(\boldsymbol{k}^{(s)}, \boldsymbol{x}) \sin\left(\pi k_y^{(s)}(y/\epsilon)\right) \right) \\
&\times \exp\left(2\pi i(k_x^{(s)} x/\epsilon + k_z^{(s)} z/\epsilon)\right) \\
&= \boldsymbol{v}^{(s)}\left(\boldsymbol{x}, \frac{\boldsymbol{x}}{\epsilon}\right),
\end{aligned}
$$

where $\hat{\boldsymbol{v}}_1(\boldsymbol{k}^{(s)}, \boldsymbol{x})$ and $\hat{\boldsymbol{v}}_2(\boldsymbol{k}^{(s)}, \boldsymbol{x})$, which are in physical space, are the results of inverse transform of the large-scale component,

$$
\begin{aligned}
\hat{\boldsymbol{v}}_1(\boldsymbol{k}^{(s)}, \boldsymbol{x}) &= \sum_{\boldsymbol{k}^{(l)}\in\Lambda_E} \hat{\boldsymbol{v}}(E\boldsymbol{k}^{(s)} + \boldsymbol{k}^{(l)}) \sin\left(\pi k_y^{(l)} y\right), \\
\hat{\boldsymbol{v}}_2(\boldsymbol{k}^{(s)}, \boldsymbol{x}) &= \sum_{\boldsymbol{k}^{(l)}\in\Lambda_E} \hat{\boldsymbol{v}}(E\boldsymbol{k}^{(s)} + \boldsymbol{k}^{(l)}) \cos\left(\pi k_y^{(l)} y\right).
\end{aligned}
$$

Remark B.0.1. *Note that $v^{(s)}(\boldsymbol{x}, \boldsymbol{z})$ is a periodic function in $\boldsymbol{z}$ with mean zero.*

Bibliography

Abe, H., Kawamura, H. & Matsuo, Y. 2001 Direct numerical simulation of a fully developed turbulent channel flow with respect to the Reynolds number dependence. *Journal of Fluids Engineering* **123**, 382–393.

Aldama, A. A. 1990 *Filtering techniques for turbulent flow simulation*, , vol. 56. Springer, Berlin.

Antonia, R. A., Teitel, M., Kim, J. & Browne, L. W. 1992 Low Reynolds number effects in a fully developed turbulent channel flow. *J. Fluid Mech.* **236**, 579–605.

Bagget, J. S., Jimenez, J. & Kravchenko, A. G. 1997 Resolution requirements in large-eddy simulations of shear flows. *Annual Research Briefs*. Center for Turbulence Research, NASA Ames/Stanford University, pp 51-66.

Baggett, J. S. 1998 On the feasibility of merging LES with RANS for the near-wall region of attached turbulent flows. *Annual Research Briefs*. Center for Turbulence Research, NASA Ames/Stanford University, pp. 267-277.

Balint, J.-L., Wallace, J. M. & Vukoslavcevic, P. 1991 The velocity and vorticity vector fields of a turbulent boundary layer. Part 2. Statistical Properties. *J. Fluid Mech.* **228**, 53.

Berselli, L. C., Iliescu, T. & Layton, W. J. 2006 *Mathematics of Large Eddy Simulation of Turbulent Flows*. Springer.

Betchov, R. 1956 An inequality concerning the production of vorticity in isotropic turbulence. *J. Fluid Mech.* **1**, 497–504.

Cabot, W. & Moin, P. 1999 Approximate wall boundary conditions in the large-eddy simulation of high Reynolds number flows. *Flow Turbul. Combust.* **63**, 269–291.

Champagne, F. H., Friehe, C. A., LaRue, J. C. & Wyngaard, J. C. 1977 Flux measurements, flux estimation techniques and fine-scale turbulence measurements in the unstable surface layer over land. *J. Atmos. Sci* **34**, 515–530.

Chapman, D. R. 1979 Computational aerodynamics development and outlook. *AIAA Journal* **17**, 1293–1313.

Cheng, M., Hou, T. Y. & Yan, P. 2011 A data-driven stochastic multiscale method. *(In preparation)* .

Chorin, A. J. & Marsden, J. E. 1993 *A mathematical introduction to fluid mechanics*, 3rd edn. Springer, New York.

Chung, D. & Pullin, D. I. 2009 Large-eddy simulation and wall modelling of turbulent channel flow. *J. Fluid Mech.* **631**, 281–309.

Ciarlet, P. G. 1988 *Mathematical elasticity, Volume I: Three-dimensional elasticity*. North-Holland, Elsevier Science Publisher.

Clark, R. A., Ferziger, J. H. & Reynolds, W. C. 1979 Evaluation of subgrid-scale models using an accurately simulated turbulent flow. *J. Fluid Mech.* **91**, 1–16.

van Driest, E. R. 1956 On turbulent flow near a wall. *J. Aerospace Sci* **23**, 1007–1011.

Eckelmann, H. 1974 The structure of the viscous sublayer and the adjacent wall region in a turbulent channel flow. *J. Fluid Mech.* **65**, 429–459.

Ferziger, J. H. 1977 Large eddy simulations of turbulent flows. *AIAA Journal* **15(9)**, 1261–1267.

Fishman, G. S. 1996 *Monte Carlo: Concepts, Algorithms, and Applications.*. Springer-Verlag, New York.

Hamba, F. 2003 A hybrid rans/les simulation of turbulent channel flows. *Theoret. Comput. Fluid Dyn.* **16**, 387–403.

Hamba, F. 2006 A hybrid rans/les simulation of high-Reynolds-number channel flow using additional filtering at the interface. *Theoret. Comput. Fluid Dyn.* **20** (2), 89–101.

Horiuti, K. 2001 Alignment of eigenvectors for strain rate and subgrid-scale stress tensors. *Direct and large-eddy simulation IV, Geurts, Friedrich and Metais eds., Kluwer,* pp. 67–72.

Hou, T.Y. & Wu, X. 1997 A multiscale finite element method for elliptic problems in composite materials and porous media. *J. Comp. Phys.* **134** (1), 169–189.

Hou, Thomas Y. & Li, Ruo 2007 Computing nearly singular solutions using pseudo-spectral methods. *J. Comp. Phys.* **226**, 379–397.

Hou, T. Y., Yang, D. P. & Ran, H. 2005 Multiscale analysis in Lagrangian formulation for the 2-D incompressible Euler equation. *Discrete and Continuous Dynamical System, Series A* **13**, 1153–1186.

Hou, T. Y., Yang, D. P. & Ran, H. 2008 Multiscale analysis and computation for the three-dimensional incompressible Navier-Stokes equations. *Multiscale Model. Simul.* **6**, 1317–1346.

Hu, X., Lin, G., Hou, T. Y. & Yan, P. 2012 An adaptive anova-based data-driven stochastic method for elliptic pde with random coefficients. *(In preparation)* .

Hussain, A. K. M. F. & Reynolds, W. C. 1970 The mechanics of an organized wave in turbulent shear flow. *J. Fluid Mech.* **41**, 241–258.

Jeong, J. & Hussain, F. 1995 On the identification of a vortex. *J. Fluid Mech.* **285**, 69–94.

Jeong, J., Hussain, F., Schoppa, W. & Kim, J. 1997 Coherent structures near the wall in a turbulent channel flow. *J. Fluid Mech.* **332**, 185–214.

von Kármán, T. 1930 Mechanische Ahnlichkeit und turbulenz. In *Proc. Third Int. Congr. Applied Mechanics*, pp. 85–105. Stockholm.

Kastrinakis, E. G. & Eckelmann, H. 1983 Measurement of streamwise vorticity fluctuations in a turbulent channel flows. *J. Fluid Mech.* **137**, 165–186.

Kim, J., Moin, P. & Moser, R. 1987 Turbulence Statisitics in Fully Developed Channel Flow at Low Reynolds Number. *J. Fluid Mech.* **177**, 1317–1346.

Kravchenko, A. G., Moin, P. & Moser, R. 1996 Zonal embedded grids for numerical simulations of wall-bounded turbulent flows. *J. Comp. Phys.* **127**, 412–423.

Kreplin, H. & Eckelmann, H. 1979 Behavior of the three fluctuating velocity components in the wall region of a turbulent channel flow. *Phys. Fluids* **22** (7), 1233–1239.

Lamb, H. 1945 *Hydrodynamics*. Dover.

Launder, B. E. & Spalding, D. B. 1972 *Mathematical models of turbulence*. Academic Press, London.

Lesieur, M. & Métais, O. 1996 New trends in large-eddy simulations of turbulence. *Ann. Rev. Fluid Mech.* **28**, 45–82.

Lilly, D. K. 1987 *Lecture notes on Turbulence*, pp. 171–218. World Scientific.

Liu, S., Meneveau, C. & Katz, J. 1994 On the properties of similarity subgrid-scale models as deduced from measurements in a turbulent jet. *J. Fluid Mech.* **275**, 83–119.

Loève, M. 1977 *Probability Theory*, 4th edn. Springer-Verlag, New York.

Lund, T.S. & Novikov, E. A. 1992 Parameterization of subgrid-scale stress by the velocity gradient tensor. *Center for Turbulence Research (Stanford University and NASA* pp. 27–43.

Marusic, I., Kunkel, G. & Portè-Agel, F. 2001 Experimental study of wall boundary conditions for large-eddy simulations. *J. Fluid Mech.* **446**, 309–320.

McLaughlin, D. W., Papanicolaou, G. C. & Pironneau, O. R. 1985 Convection of microstructure and related problems. *SIAM J. Appl. Math.* **45**, 780–797.

Meneveau, C., Lund, T. S. & Moin, P. 1992 Search for subgrid scale parametrization by projection pursuit regression. *Proceedings of the Summer Program Center for Turbulence Research* pp. 61–81.

Misra, A. & Pullin, D. I. 1997 A vortex-based subgrid stress model for large-eddy simulation. *Phys. Fluids* **9** (8), 2443–2454.

Mohammadi, B. & Pironneau, Olivier 1994 *Analysis of the k-epsilon turbulence model*. John Wiley & Sons.

Moin, P. & Jimenez, J. 1993 Large eddy simulation of complex flows. In *24th AIAA Fluid Dynamics Conference, Orlando, USA*.

Moser, R. D., Kim, J. & Mansour, N. N. 1999 Direct numerical simulation of turbulent channel flow up to $re_\tau = 590$. *Phys. Fluids* **11** (4), 943–945.

Niederreiter, H., Hellekalek, P., Larcher, G. & Zinterhof, P. 1998 *Monte Carlo and Quasi-Monte Carlo Methods 1996*. Springer-Verlag, Berlin.

Pope, S. B. 1985 Pdf methods for turbulent reactive flows. *Progress in Energy and Combustion Science* **11**, 119–192.

Pope, S. B. 1994 Lagrangian pdf methods for turbulence flows. *Annu. Rev. Fluid Mech.* **26**, 23–63.

Pope, S. B. 2000 *Turbulent Flows*. Cambridge University Press.

Prandtl, L. 1925 Über die ausgebildete turbulenz. *Z. angew. Math. u. Mech* **5**, 136–139.

Rogallo, R. S. & Moin, P. 1984 Numerical simulation of turbulent flows. *Ann. Rev. Fluid Mech.* **16**, 99–137.

Sagaut, P. 2001 *Large eddy simulation for incompressible flows, an introduction*. Springer-Verlag.

Schoppa, W. & Hussain, F. 2002 Coherent structure generation in near-wall turbulence. *J. Fluid Mech.* **453**, 57–108.

Schumann, U. 1975 Subgrid scale model for finite difference simulations of turbulent flows in plane channels and annuli. *J. Comp. Phys.* **18**, 376–404.

Schwab, C. & Todor, R. A. 2006 Karhunen-Loève approximation of random fields by generalized fast multipole methods. *J. Comp. Phys.* **217**, 100–122.

Sirovich, L. 1987 Turbulence and the dynamics of coherent structures, Parts I, II and III. *Q. Appl. Maths XLV* pp. 561–590.

Smagorinsky, J. 1963 General circulation experiments with the primitive equations. i. the basic experiment. *Monthly Weather Review* **91**, 99–164.

Spalart, P., Moser, R & Rogers, M. 1994 Spectral methods for the Navier-Stokes equations with one infinite and two periodic directions. *J. Comp. Phys.* **96**, 297–324.

Spalart, P. R. 1988 Direct simulation of a turbulent boudnary layer up to $re_\theta = 1410$. *J. Fluid Mech.* **187**, 61–98.

Spalart, P. R., Jou, W. H., Strelets, M. & Allmaras, S. R. 1997 Comments on the feasibility of LES for wings, and on a hybrid RANS/LES approach. In *First AFOSR International Conference on DNS/LES*, pp. 137–147.

Squires, K. D., Forsythe, J. R. & Spalart, P. R. 2005 Detached-eddy simulation of the separated flow over a rounded-corner square. *J. Fluids Eng.* **127**, 959–966.

Tennekes, H. & Lumley, J. L. 1972 *A first course in Turbulence*. MIT Press.

Travin, A., Shur, M., Strelets, M. & Spalart, P. 2001 Detached-eddy simulations past a circular cylinder. *Flow, Turbul. Combust.* **63**, 293–313.

Venturi, D., Wan, X. & Karniadakis, G. E. 2008 Stochastic low dimensional modeling of random laminar wake past a circular cylinder. *J. Fluid Mech.* **606**, 339–367.

Vreman, B., Geurts, B. & Kuerten, H. 1996 Large eddy simulation of the temporal mixing layer using the Clark model. *Theoret. Comput. Fluid Dyn.* **8**, 309–324.

Vreman, B., Geurts, B. & Kuerten, H. 1997 Large-eddy simulation of the turbulent mixing layer. *J. Fluid Mech.* **339**, 357–390.

Wang, M. & Moin, P. 2002 Dynamics wall modelling for large-eddy simulation of complex turbulent flows. *Phys. Fluids* **14**, 2043–2051.

Xiu, D. 2010 *Numerical Methods for Stochastic Computations-A Spectral Method Approach*. Princeton University Press.

Xiu, D. & Karniadakis, G. E. 2002 The Wiener-Askey polynomial chaos for stochastic differential equations. *SIAM J. Sci. Comput.* **24** (2), 619–644.

Zaman, K. B. M. Q. & Hussain, A. K. M. F. 1981 Taylor hypothesis and large-scale coherent structures. *J. Fluid Mech.* **112**, 379–396.

Zang, T. A. 1991 Numerical simulation of the dynamics of turbulent boundary layers: Perspectives of a transition simulator. *Philos. Trans. R. Soc. Lond. Ser. A* **336**, 95–102.